Politecnico di Torino

Politecnico
di Torino

Department of Mechanical and Aerospace Engineering

Master's Degree Course in Aerospace Engineering

Master's Degree Thesis

Development of a conceptual design tool to predict performance and pollutant and GHG emissions of high-speed vehicles using liquid hydrogen

Supervisors:

Prof.ssa Nicole Viola

Prof.ssa Roberta Fusaro

Dr. Guido Saccone

Candidate:

Giovanni Grimaldi

December 2021

Abstract

At present day, it is easily noticeable how the interest for environmental impact of human activities is becoming more and more important. Space utilization is not exempt from this, thus new ways of estimating pollutant and greenhouse gases emissions of launchers are needed, especially in a conceptual design phase, during which the consequences of different design choices must be compared. Meanwhile, many new propulsion concepts are currently under design and, in particular, one promising category is that of precooled air-breathing rocket engines, represented by SABRE, from Reaction Engines Limited. This work aims at anticipating propulsive performance and emission estimations of such systems at conceptual design level. In particular, after a brief description of SABRE and Skylon, the vehicle which it is installed on, different models of increasing complexity are presented and their results compared with performance predictions of Reaction Engines Limited in order to validate them. After this, a method for using such results to predict emissions is presented. Finally, the tool is integrated in a Matlab Graphical User Interface previously created at Politecnico di Torino, to be then added to ASTRID-H, a conceptual design tool currently under development to evaluate performance of different high-speed air breathing propulsive systems architectures.

Sommario

In tempi recenti, si può facilmente notare come l'interesse verso l'impatto ambientale delle attività umane stia diventando sempre più rilevante. Lo sfruttamento dello spazio non è esente da tutto ciò; pertanto, è necessario sviluppare nuovi metodi che permettano di valutare le emissioni di gas serra e inquinanti dei lanciatori, specialmente in una fase iniziale di conceptual design, durante la quale le conseguenze di diverse scelte di progetto devono poter essere facilmente valutate e confrontate. Allo stesso tempo, bisogna tenere conto dei diversi innovativi sistemi propulsivi che sono attualmente in fase di sviluppo e che diventeranno operativi in futuro, tra i quali una categoria particolarmente promettente è quella dei precooled air – breathing rocket engines, dei quali il SABRE di Reaction Engines Limited è un perfetto rappresentante. Questo lavoro ha l'obiettivo di anticipare le performance propulsive di tali sistemi a livello di conceptual design. In particolare, dopo una breve descrizione del SABRE e dello Skylon, ovvero il veicolo sul quale il motore è installato, diversi modelli di crescente complessità sono descritti e i loro risultati confrontati con le stime delle performance pubblicate da Reaction Engines, in modo da poterli validare. Dopodiché, viene presentato un metodo che permetta di sfruttare tali risultati per predire le emissioni prodotte. Infine, viene descritto come il codice sviluppato sia stato integrato in una Graphical User Interface di Matlab, precedentemente creata al Politecnico di Torino, in modo da poterlo poi aggiungere ad ASTRID-H, un tool di conceptual design, attualmente in fase di sviluppo, per la valutazione delle performance di diverse architetture di sistemi propulsivi air – breathing per velivoli ad alta velocità.

Acknowledgements

Thank you to all the people that supported me, in one way or another, during my years of university and that allowed me to finally reach this goal.

First of all, I would like to thank my supervisors from Politecnico di Torino, professors Nicole Viola and Roberta Fusaro for their precious help and suggestions, and for helping me in finding such an interesting topic in the wide field of environmental impact. I find their efforts to focus on the environmental analysis of future aviation to be really useful to draw also the attention of students and I am glad for having been allowed to be a small part of it. Heartfelt thanks also to dr. Guido Saccone from Centro Italiano Ricerche Aerospaziali, for his priceless support in the estimation of emissions of SABRE and especially for his continuous and immediate availability in solving any incoming problem. I really hope to leave to all of them a small part of how much they taught me. Thanks also to dr. Valeria Vercella for the suggestions regarding the development of the graphical interface.

Thanks also to my family, for being so supportive in all my choices, economically and emotionally, and for letting me live this path in a way as serene as possible.

Finally, I would like to thank from the deepest of my heart Federica and my friends Filippo, Paolo and Matteo. I am sure that they all know how much their help was needed during the past years.

Thanks very much to all of you and to all those who, consciously or not, helped me to arrive to this point.

Table of contents

List of figures

List of tables

Nomenclature

SABRE	=	Synergetic Air – Breathing Rocket Engine
HOTOL	=	Horizontal Take Off and Landing
LACE	=	Liquid Air Cycle Engine
HX	=	Heat Exchanger
He	=	Helium
H2	=	Hydrogen
LOx	=	Liquid Oxygen
REL	=	Reaction Engines Limited
T	=	Temperature
p	=	pressure
ρ	=	density
TPR	=	Total Pressure Recovery
ϵ	=	Pneumatic efficiency
η	=	efficiency
M_0	=	Flight Mach number
PC	=	precooler
$\dot{m}$	=	Mass flow rate
Q	=	Exchanged heat power
AC	=	Air Compressor
f	=	Fuel to air ratio
H_i	=	Net calorific value
c_p	=	Specific heat at constant pressure
c_v	=	Specific heat at constant volume
γ	=	Specific heats ratio
z	=	altitude
F_g	=	Gross thrust
F_u	=	Uninstalled thrust
T_{sp}	=	Specific thrust
I_{sp}	=	Specific impulse
PB	=	Pre-burner
CC	=	Combustion chamber
β	=	Compressor or turbine pressure ratio
LHP	=	Liquid Hydrogen Pump
W	=	Power
ϕ	=	Fuel to air equivalence ratio
HT	=	Hydrogen Turbine
HeT	=	Helium turbine
MM	=	Molar mass
NO_x	=	Nitrogen oxides
FAR	=	Fuel to air ratio
FL	=	Flight Level
SL	=	Sea Level
EI	=	Emission Index

1 Research background and main objectives

At present day, it is easily noticeable how the interest for environmental impact of human activities is getting more and more important. Common people are fortunately becoming increasingly aware of climate problems and the industry is continually struggling to be compliant with stricter regulations concerning environmental protection. Space utilization is not exempt from this, thus new ways of estimating pollutant and greenhouse gases emissions of launchers are needed.

Moreover, there are many new propulsion concepts under development and, in particular, one promising category is that of hybrid rocket engines, that work as an airbreathing engine for the first part of the ascent and as a pure rocket when the atmosphere is not dense enough. The scope of this work is to build a model to analyze the performance and environmental impact of one specific category of this engines, the precooled air breathing rocket engines, which a perfect example of is the SABRE (Synergetic Air – Breathing Rocket Engine) by Reaction Engines Ltd.

SABRE will probably drastically affect and shape the future of space exploration and utilization. It is an example of hydrogen fueled hybrid rocket engine, a machine that has the objective to merge the benefits of air breathing and rocket engines, which are respectively characterized by a high specific impulse and a high thrust. SABRE works as a precooled jet engine for the first part of its mission, starting from ground level to around 25 km of altitude and a velocity around Mach 5, at which point, due to the decreased level of atmospheric oxygen, it switches to rocket mode to reach a parking low Earth orbit. By doing this, it largely decreases the amount of oxidant to store onboard, guaranteeing a high specific impulse for the lower part of the flight and a great thrust necessary to reach space.

In particular, SABRE will be mounted on Skylon, even if the key technologies for its functioning are opening new perspectives in different areas, from electric and hypersonic air travel to the automotive field (Reaction Engines Limited, s.d.). Skylon is a fully reusable Single Stage To Orbit spaceplane: it takes off as a common plane but reaches space where it can complete maneuvers thanks to an orbital maneuvering engine and then return to ground level and land as a common plane. The expected turnaround time of Skylon is around one or two days (Reaction Engines Limited, 2014) thus giving the possibility to accomplish a much higher launch frequency. Moreover, according to (Stanley, s.d.) and (Nailard, 2020), the value of the space economy will increase in the next years from the $350 billion of 2016 to $1 trillion in 2040 and this growth will be also imputable to space tourism, in which Skylon has the potential to play a key role with the development of a passenger module (Hempsell, 2010), and suborbital flights that can connect antipodal points faster, since this is what truly engage popular enthusiasm (Pelton, 2019). Also the UK parliament has stated (Parliament, 2011) that in this decade the space industry will levitate and Skylon gives the possibility to decrease the cost for

putting satellites into orbit from £15000 to £650 per kg. These two aspects together let easily imagine how much the launch frequency will increase, for example for applications, such as a Space Based Solar Power system, that are impracticable with current launchers. For such an application the expected launch rate would be, as stated in (Erik J.L. Larson, 2016), around 10^4 per year for 10 years and this is why it is dutiful and it will become necessary to evaluate the environmental impact of space missions in future. It is also interesting to notice that this would give rise to the necessity of having around 70 working spaceplanes, which is in line with what found in (Mark Hempsell, 2016), where it is stated that such a production would guarantee for the producer an Internal Rate of Return (a measure of profitability of investments) of 10%, which is sufficiently high for a Public Private Partnership.

With all these aspects in mind, this study aims at assessing the environmental impact of such a technology: in fact in literature no estimations were found regarding this engine in particular, while there are a few regarding the Scimitar engine, which is derived from the SABRE but shows some key different aspects, such as a slightly different cycle and a much leaner combustion (Tayfun Tanbay M. B., 2020).

Regarding this work in particular, in the next chapter some details and key features of Skylon and SABRE are reported, in order to familiarize with the peculiar aspects of this propulsion architecture. Then, in the following chapter, the models developed to describe this type of engine in the air – breathing phase are described in detail and validated against the data reported by Reaction Engines Ltd. A path of increasing complexity was followed, in order to give different alternatives that can be used in an initial phase of the design, based also on the availability of data: the first models give rougher predictions but require less input while the last model is the most accurate but also the highest demanding in terms of input data necessary. Later, the model used to evaluate the emissions of the SABRE via the p3T3 method is presented, with also a comparison with another similar launch system. Last, the Graphic User Interface, that was created to evaluate performance of SABRE-like propulsion systems, is described in details with some examples of utilization.

2 Background on Skylon and SABRE

The engine on which the models that will be illustrated in chapter 3 were validated is the SABRE, an air breathing rocket engine capable of switching to pure rocket mode after the first part of the ascent. SABRE is under development by the UK company Reaction Engines Ltd and it will power the proprietary spaceplane Skylon. More details about these can be found in the following paragraphs.

2.1 Skylon

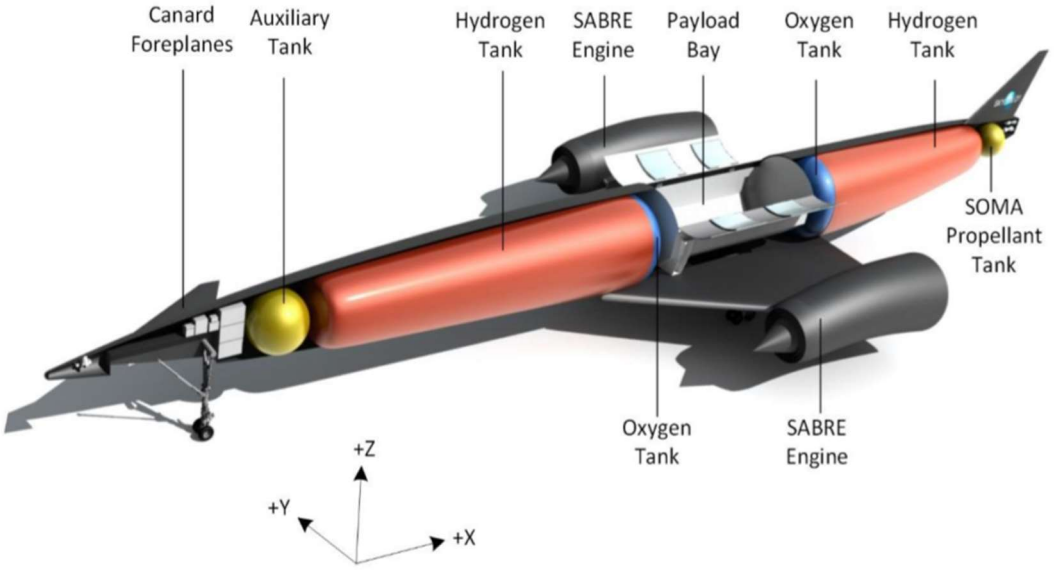

Figure 2.1: Skylon layout (from (Reaction Engines Limited, 2014))

Skylon is the fully reusable, Single Stage To Orbit spaceplane currently being designed by Reaction Engines Ltd. The main characteristic of the vehicle is its capability of taking off and landing on an extended runway much like a common airplane. This facilitates its management as for example it can be prepared in hangars and moved around without the need of the complex and expensive machines commonly necessary for other launchers. The payload bay is located in correspondence of the wing attachment and the payload is loaded from above, similarly to what was done with the Space Shuttle. Differently from designs of other spaceplanes, Skylon shows a clear division between the slender fuselage and the wing, that was proven to be optimum in terms of weight, lift and volume, though creating problems related to the fact that the wing does not fit entirely inside the bow shoch at the reentry, determining high localized heat fluxes and the necessity of an active cooling system.

The main structure is a frame composed by struts made from titanium with silicon carbide reinforcement, while the aluminum tanks are suspended by Kevlar ties. The frame is then covered with sheets of a reinforced glass ceramic material which acts both as the aeroshell and the main thermal protection system, together with a multilayer metallic heat shield. The dimensions are 83.1 meters of fuselage length and a wingspan of 21.8 meters.

The greatest part of the fuselage is occupied by the hydrogen cryogenic tanks, while a minimum part is reserved for the liquid oxygen tanks, thanks to the fact that in the first part of the ascent the oxidizer is the outside air. The position of the tanks is related to the equilibrium problems, that were noted to affect the vehicle, and that were solved with a careful aerodynamic design and with the differential burning of the propellant in the two tanks. The control of the spaceplane is made through control surfaces in atmosphere, namely by the canard foreplanes in pitch, ailerons in roll and an aft fin in yaw, while during the pure rocket ascent the yaw and pitch control are taken over by the differential engine throttling and nozzles gimbaling and when the main engines are shut off the reaction control thrusters are used. In addition to this, there is also the SOMA, Skylon Orbital Maneuvering Assembly, for in orbit maneuvers.

The gross take off mass is around 325 tons with a dry mass of 53.4 tons. An example of payload altitude diagram is reported in

Figure *2.2*, showing that the payload capacity of Skylon is similar to that of Ariane V for example. Below it is also possible to see data regarding the ascent and descent trajectory.

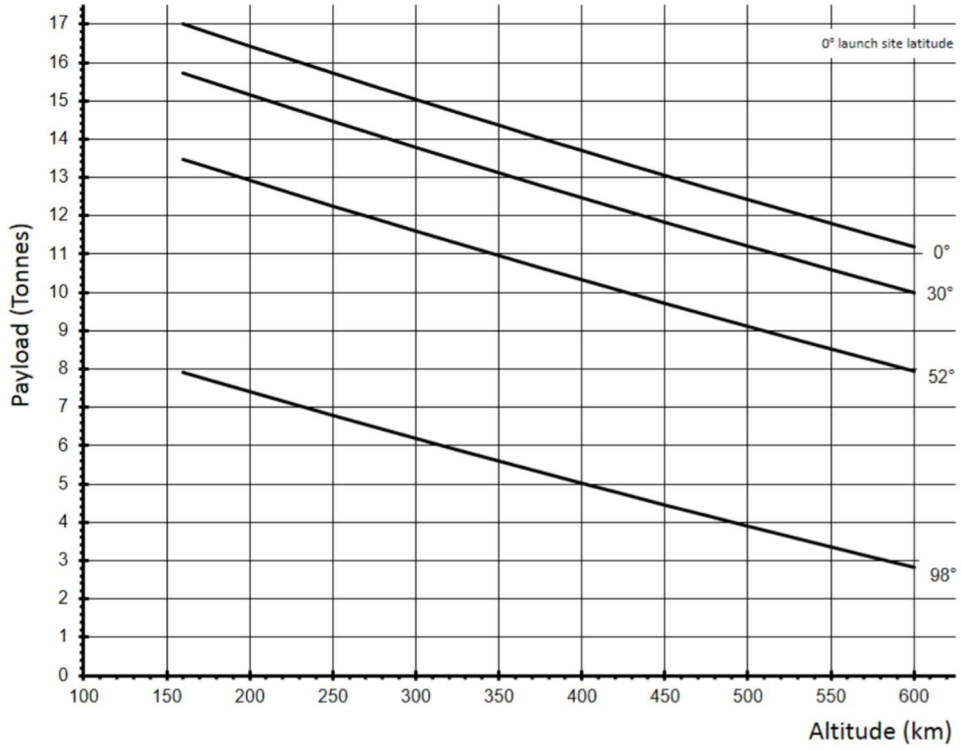

Figure 2.2: Payload - altitude diagram (from (Reaction Engines Limited, 2014)*)*

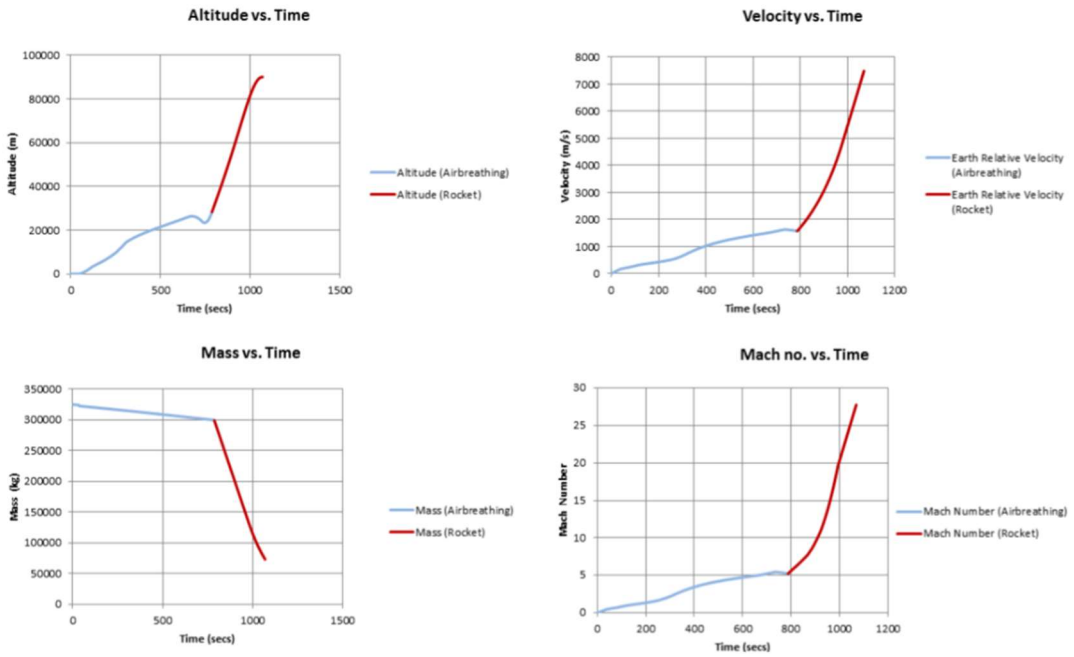

Figure 2.3: ascent trajectory (from (Reaction Engines Limited, 2014))

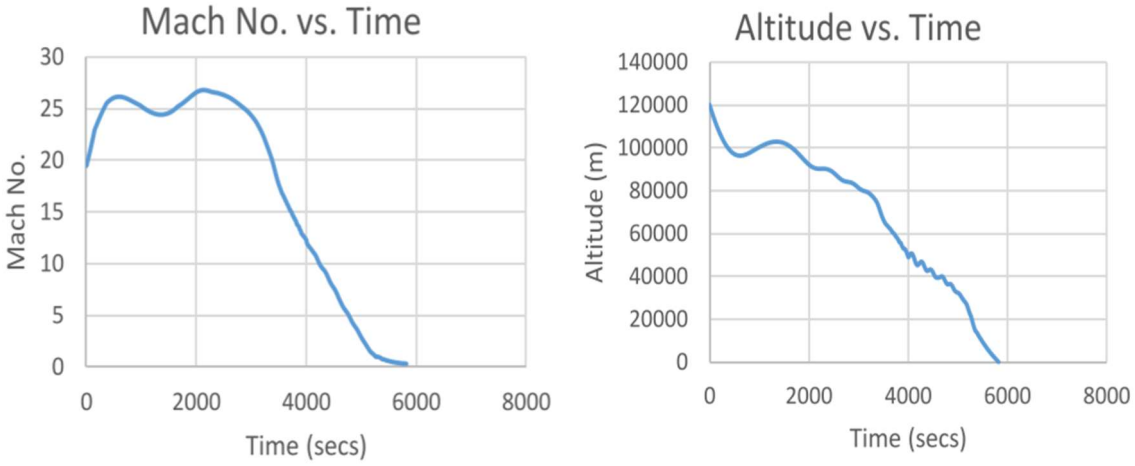

Figure 2.4: descent trajectory (from (Reaction Engines Limited, 2014))

2.2 SABRE

SABRE stands for Synergetic Air – Breathing Rocket Engine and it is the main propulsion system of Skylon. Much as Skylon is an evolution of British Aerospace HOTOL, it is derived by the corresponding liquid air cycle engine (LACE), however avoiding air liquefaction.

As said before, SABRE is capable of operating as an air breathing engine in the first part of the ascent, until an altitude around 25 km and a velocity corresponding to Mach 5. Eventually, the air becoming too rarefied, the functioning is switched to a pure rocket mode in which both fuel and oxidizer are on board consumables.

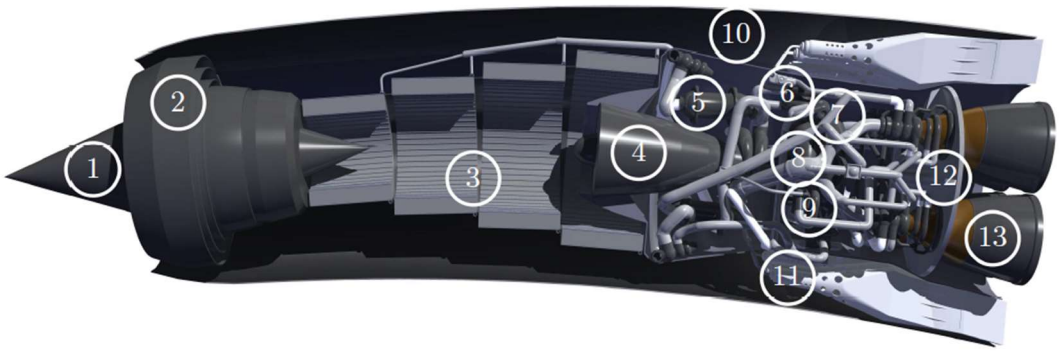

Figure 2.5: From ((Fernandez-Villace, 2013)) SABRE section: 1) movable spike 2) intake 3) precooler 4) air compressor 5) pre-burner and reheater (HX3) 6) helium circulator 7) H2 pump 8) He turbine and regenerator (HX4) 9) LOx pump 10) spill duct 11) ramjet burners 12) heat shield 13) thrust chamber

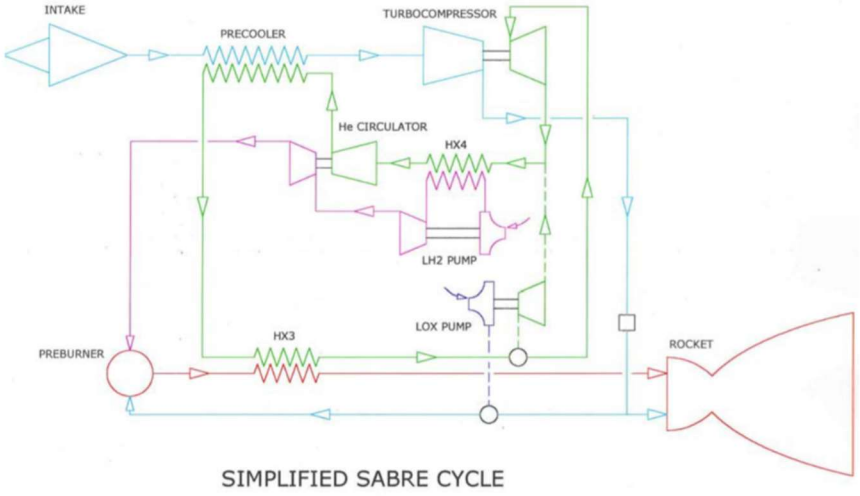

Figure 2.6: SABRE cycle in both air breathing and rocket modes (from (TEC-MPC, 2011))

In many ways, the engine allows to keep together the advantages of air breathing and rocket engines, respectively the low propellant consumption, since only the fuel mass is significant for the performance in the first phase, and the high delivered thrust, allowing for a great reduction of total weight. The engine cycle is reported in Figure 2.6 and, as it can be seen, it is a turbomachinery-based cycle, allowing the generation of static thrust, differently from a ramjet.

Generally speaking, in the first mode, the air captured by the intake is deeply cooled down before entering a high pressure ratio compressor; after that the flow is split and a part goes to a pre-burner which, through the consequent heat exchanger allows, together with the precooler, to power the helium cycle. The remaining air is directly fed into the chamber which, thanks to the high compressor outlet pressures, can be a rocket type combustion chamber allowing to have an exit area lower than the intake area. This air cycle is supported by two other cycles: the hydrogen and the helium ones. The hydrogen is used as the fuel but also as the heat sink for the heat extracted by the precooler, through the

HX4. The possibility of using the hydrogen directly facing the air cycle inside the PC was discarded due to hydrogen embrittlement problems thus introducing the necessity of the helium closed loop that serves to transfer the heat from the air to the hydrogen while also powering the air compressor. The helium is in fact strongly heated inside the precooler and slightly in the HX3, flowing then in the turbine mechanically linked to the compressor and then in the HX4 that transfer power to the hydrogen cycle which then powers the first turbine linked to the liquid fuel turbopump and then to the second turbine linked to the helium circulator.

The intake operates, when in supercritical mode, with a three shocks compression, the first at the tip of the movable spike, the second at the cowl before the throat and the third after the intake throat. The position of this last shock is controlled with the spillage of the flow to the bypass burners. These are introduced because the nacelle is designed to swallow the amount of air necessary for the core engine to operate at an altitude of 25 km: therefore, at lower altitudes and higher atmospheric densities, the ingested air is higher than necessary and must be bypassed. In order not to incur in a high drag penalty, some fuel is also bypassed and burnt in a ring of ramjet burners. This is possible because the engine runs with a very hydrogen rich mixture due to the cooling requirements. The problem of the unburnt hydrogen discharge has been object of optimization in works such as (Jianqiang Zhang, 2017). The nacelle then closes in the rocket phase to reduce drag.

However, the enabling technology of SABRE cycle is the precooler, which has been subject of the highest research interest by REL (Varvill, Heat exchanger development at Reaction Engines Ltd., 2010). It is composed by an array of brazed microchannels made by Inconel cast alloy 718 in which the helium flows and cools down the outside air flow of roughly 400 kg/s from a temperature of 1250K to 100K. The low temperatures at the compressor inlet allow then for the high compression ratio of 140. Many problems are related to the precooler, one above all the possible formation of ice that could disturb the flow and cause unpredictable performances. However, the precooler has been successfully tested in late 2019 by REL, followed then by the successful testing of the pre burner and HX3 (Reaction Engines Limited, s.d.).

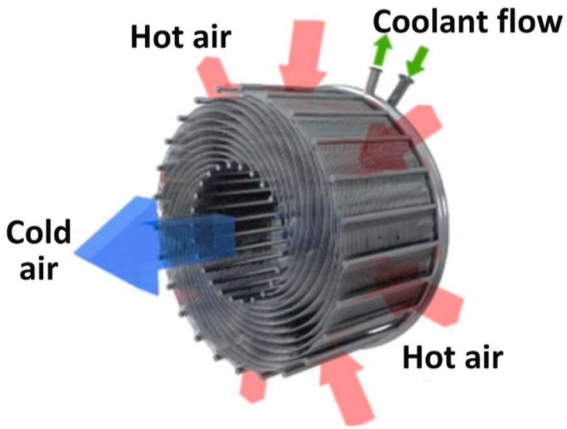

Figure 2.7: scheme of the SABRE precooler (from (Dai Jian, 2020))

After the precooler the air goes in the compressor which is a relatively conventional three spools axial compressor powered by the counter rotating helium turbine, that can in turn power also the LOx turbopump during the rocket ascent. There is then the pre burner that,

differently from classical staged combustion, is used as a heat source to top off the heat input in the helium cycle through the counterflow HX3 heat exchanger. The pre burner always operates in rich mixture conditions and for each nacelle there are two of them that constitutes a redundancy in the rocket phase but that are both necessary to power the air compressor. The combustion chamber is also a relatively conventional component and in particular it uses a film cooling technique involving both the hydrogen and compressed air in the airbreathing phase and liquid oxygen in the rocket phase, since most part of the fuel is always already used to cool the helium loop. Other important components are the hydrogen and oxygen turbopumps which operates with inlet and outlet pressures respectively of 1 and 260 bar for the hydrogen turbopump in the airbreathing phase and 4 and 400 bar for the oxygen in the rocket phase. One key problem of this components is to avoid cavitation since it could damage the blades, conflicting with the Skylon requirement of being reusable and having a strict turnaround time. Regarding the helium loop, there is the circulator which is a centrifugal compressor that operates at almost constant speed and that is powered by the first hydrogen turbine.

One particular aspect of the SABRE nacelle is its curved shape: it is due to the fact that, especially at low speed, when the mass of Skylon is higher due to the full tanks, the incidence of the wing must be high. However it is desirable to have the intake parallel to the incoming flow in order to have symmetry of the shocks but this cannot be done by attaching the engines with an angle respect to the vehicle because it would lead to a misaligned thrust in the rocket phase: thus the curved nacelle.

To sum up, the SABRE is built for two relatively different purposes: to serve as an air breathing deeply precooled engine and as a high specific impulse rocket. In order to do so, it follows the cycle reported before and it comprises four thrust chambers, two preburner-HX3 units, two hydrogen turbopumps and two helium loops. This allows it to operate as one air breathing engine and as two separate rocket engines. Thus a key aspect of the models presented in the following chapter is that they are scaled down in order to incorporate one unit of each component and they neglect the presence of the ramjet burners, considering the intake to match the requests of the compressor with nominal pressure recovery. Therefore, the resulting performances are to be compared to one fourth of those of the full scale engine, which still have to be doubled to match the Skylon propulsive plant characteristics, since it is made up of two SABRE.

In Figure 2.8, the performances of the SABRE are compared to other engine types, clearly showing its superiority in terms of thrust to weight ratio to the other common airbreathing engines and its higher specific impulse with respect to a pure rocket.

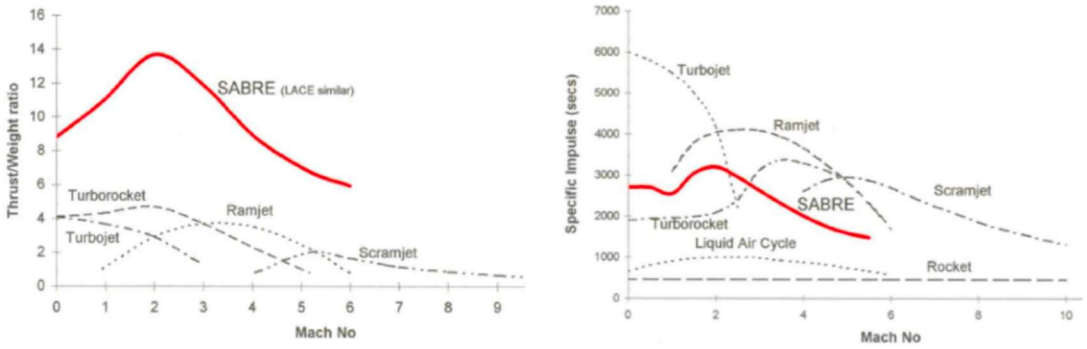

Figure 2.8: SABRE thrust to weight ratio and specific impulse in comparison with other engines (from (Dai Jian, 2020))

3 Air – breathing models development

The aim of the next section of this work is to present the path used to develop the different models that can be used to predict performance of the type of engines addressed in the thesis, with a particular reference to SABRE, the air breathing rocket engine currently under development by Reaction Engines Limited. An increasing complexity approach was used, in order to reduce the errors introduced with the initial simplifying hypothesis. The models were then coded in Matlab to obtain the results and compare them with the performance data published by R.E.L.

3.1 Atmosphere model

The first step in the creation of the models was to calculate the atmosphere characteristics along the Skylon trajectory. In order to do so, the model developed in (Moino, 2021) was used, in turn taken from (Trainelli, 2011) that is based on the International Standard Atmosphere (ISA).

The initial conditions are the standard conditions:

- $T_{st} = 288.15\ K$
- $p_{st} = 101325\ Pa$
- $\rho_{st} = 1.225\ kg/m^3$

The conditions at the beginning of the stratosphere ($z_s = 11000m$) are:

- $T_s = 216.65\ K$

(3-1)

- $p_s = p_{st}\left(1 - 0.0065\frac{z_s}{T_{st}}\right)^{5.2561}$

(3-2)

- $\rho_s = \rho_{st}\left(1 - 0.0065\frac{z_s}{T_{st}}\right)^{4.2561}$

(3-3)

The conditions at $z_{20} = 20000\ m$ are:

- $T_{20} = 216.65\ K$

(3-4)

- $p_{20} = p_s e^{-g\frac{z_{20}-z_s}{RT_s}}$

(3-5)

- $\rho_{20} = \rho_s e^{-g\frac{z_{20}-z_s}{RT_s}}$

(3-6)

The equations to calculate the values of temperature T, pressure p and density ρ at each altitude z are the following:

- When $0 < z \leq 11000\ m$
  - $T_0 = T_{st} - 0.0065z$

(3-7)

  - $p_0 = p_{st}(1 - 0.0065\ z/T_{st})^{5.2561}$

(3-8)

  - $\rho_0 = \rho_{st}(1 - 0.0065\ z/T_{st})^{4.2561}$

(3-9)

- When $11000 < z \leq 20000\ m$
  - $T_0 = T_s$

(3-10)

  - $\mathrm{p_0 = p_s\ e^{\frac{-g(z-z_s)}{RT_s}}}$

(3-11)

  - $\mathrm{\rho_0 = \rho_s\ e^{\frac{-g(z-z_s)}{RT_s}}}$

(3-12)

- When $z > 20000\ m$
  - $T_0 = T_{20} + 0.001(z - z_{20})$

(3-13)

  - $p_0 = p_{20}(1 + 0.001(z - z_{20})/T_{20})^{\frac{-g}{R_{air}0.001}}$

(3-14)

  - $\rho_0 = \rho_{20}(1 + 0.001(z - z_{20})/T_{20})^{\frac{-g}{R_{air}0.001}-1}$

(3-15)

The results are here plotted between 0 and 25 *km,* the altitude at which SABRE switches to the rocket mode and thus is not influenced by the atmosphere anymore.

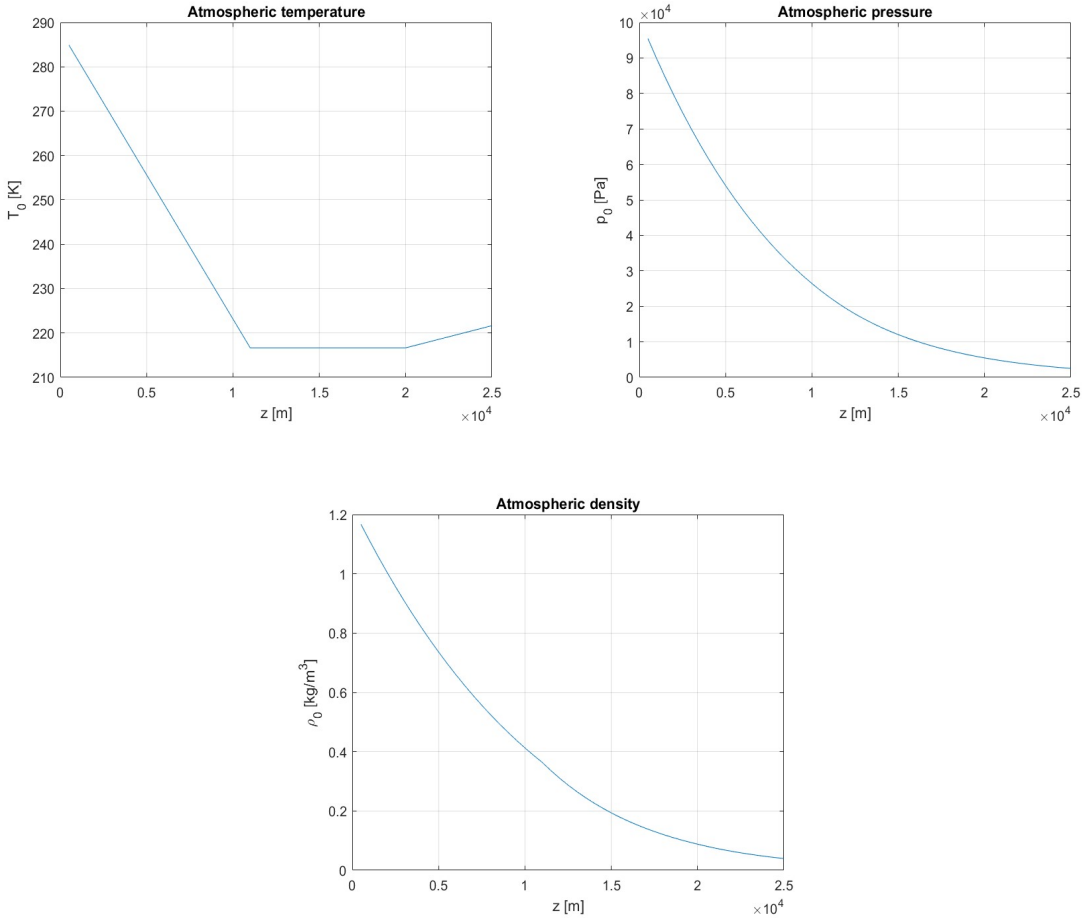

Figure 3.1: Ambient characteristics at different altitude

3.2 Ramjet with precooler and compressor model

3.2.1 Thermodynamic cycle

The simplest model that can be built, that is representative of what happens in the real thermodynamic cycle of the SABRE, considers only the air part of the cycle reported before. The simplified scheme is reported in Figure 3.2.

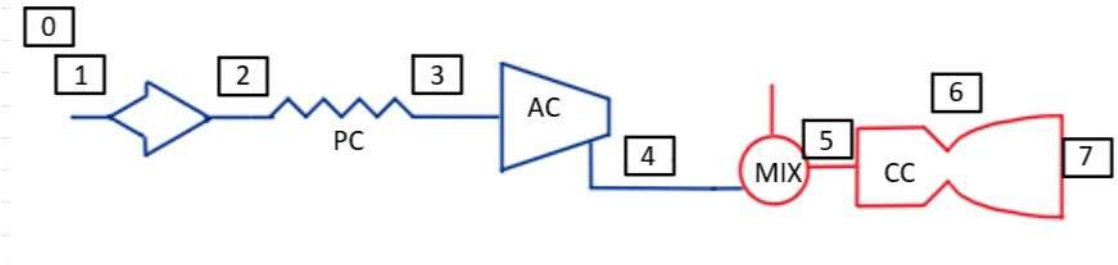

Figure 3.2: ramjet with precooler and compressor scheme

The different steps followed by the air are the following:

- 0: it is the ambient condition at the altitude considered where the properties of air are those calculated with the atmosphere model described in 3.1 and the velocity is the flight velocity;
- 1 – 2: the air passes through the intake and its velocity is decreased through an adiabatic process until it reaches subsonic velocities compatible with the compressor demand;
- 2 – 3: the air goes through the precooler where it is cooled down to the inlet temperature of the compressor;
- 3 – 4: the air is compressed through an adiabatic process in a single spool compressor;
- 4 – 5: the air is mixed with the hydrogen coming from the hydrogen tank;
- 5 – 6: the mixture is burnt in the combustion chamber with a quasi-isobaric process;
- 6 – 7: the combustion products at high temperature and pressure are expanded in the nozzle.

More hypothesis had to be stated in order to have a model as simple as possible and these are explained below where all the constitutive equations of the components are presented one by one.

Intake

Assuming that in a first phase of the design neither the exact behavior of the intake is known nor the air mass flow captured and requested by the compressor, a constant mass flow equal to that at the design point is assumed. Moreover the total pressure recovery (i.e. $\epsilon_d = p^\circ{}_2/p^\circ{}_1$) is calculated with a general formula reported in (Fernandez-Villace, 2013) that relates such a parameter to the kinetic efficiency of the intake, which is the ratio of the kinetic energy of the outlet flow, if expanded isentropically to ambient pressure, to the free stream kinetic energy.

$$\epsilon_\mathrm{d} = (1 + 0.5(\gamma - 1)(1 - \eta_k)M_0^2)^{(-\gamma/(\gamma-1))} \qquad (3\text{-}16)$$

where $\eta_k = v_{out}^2/v_\infty^2$.

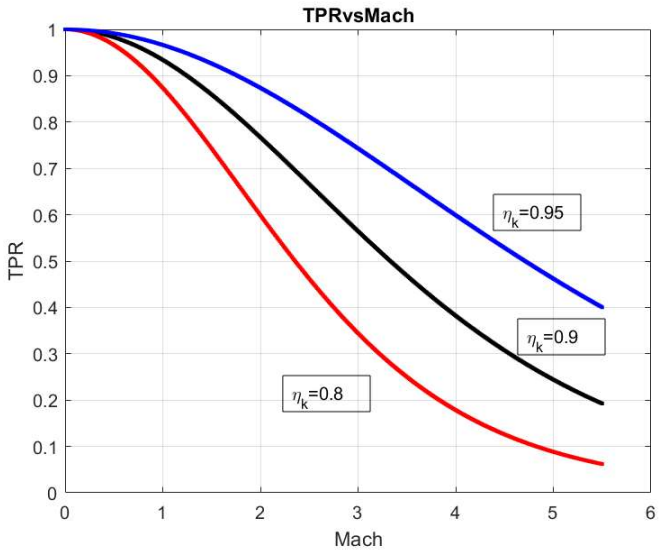

Figure 3.3: total pressure recovery along the trajectory

The values of the total pressure recovery along the trajectory are reported in Figure 3.3 for three different efficiencies. However, in the calculation a kinetic efficiency of 0.9 was assumed, as suggested in (Fernandez-Villace, 2013).

Thus, since the process is adiabatic, the relations are:

$$p°_2 = p°_1 \epsilon_d \tag{3-17}$$

$$T°_2 = T°_1 \tag{3-18}$$

Where the symbol ° indicates the stagnation conditions that are calculated with the equations below.

$$T°_1 = T_0 \left(1 + \frac{\gamma - 1}{2} M_0^2\right) \tag{3-19}$$

$$p°_1 = p_0 \left(1 + \frac{\gamma - 1}{2} M_0^2\right)^{\frac{\gamma}{\gamma - 1}} \tag{3-20}$$

With M_0 the free stream Mach number and γ the adiabatic expansion coefficient of air.

Precooler

The precooler is the key component of SABRE and it is here modeled as a heat exchanger with a total pressure loss along the flow. The outlet temperature of the PC is considered a design parameter and thus is given and assumed to be constant along the trajectory. This is equivalent to say that the PC is capable to adapt to the different demands in the different flight conditions and it is a sensible hypothesis given that in the real cycle the mass flow

of hydrogen and the conditions of the helium loop can be adapted by using different valves. The temperature is thus set equal to the design point temperature calculated in (Fernandez-Villace, 2013), $T°_3 = 97K$.

Regarding the total pressure loss it is also assumed to be constant and equal to the 28% of the inlet total pressure, as in (Fernandez-Villace, 2013).

The equations are the following:

$$Q_{PC} = \dot{m}_1 c_{p_{23}} (T°_3 - T°_2)$$

(3-21)

$$p°_3 = p°_2 \epsilon_{PC}$$

(3-22)

Where Q_{PC} is the power exchanged in the precooler, whose other side is not considered in this model, $\dot{m}_1$ is the air mass flow and $c_{p_{23}}$ is the average isobaric specific heat of air iteratively calculated by using also the tool developed in (Mjaavatten, 2021) which is based on the database of (National Institute of Standards and Technology).

Air compressor

Regarding the air compressor, similar considerations as for the intake were done and so a constant pressure ratio was considered and put equal to that calculated by (Fernandez-Villace, 2013). Moreover, a constant adiabatic efficiency of the compressor was assumed and conventionally put equal to 0.8.

The equations are:

$$p°_4 = \beta_{AC} p°_3$$

(3-23)

$$T°_4 = T°_3 \left(1 + \frac{1}{\eta_{AC}} \left(\beta_{AC}^{\frac{\gamma_{34}-1}{\gamma_{34}}} - 1 \right) \right)$$

(3-24)

Where η_{AC}, β_{AC} and γ_{34} are respectively the adiabatic efficiency, the compression ratio and the average adiabatic expansion coefficient of air between conditions 3 and 4.

Mixer

Two key assumptions were made in the mixer:

- The fuel, i.e. gaseous hydrogen, is fed at a total pressure and temperature equal to those in 4.
- The fuel mass flow is such that the fuel ratio is equal to the stoichiometric value, i.e. $f = \frac{\dot{m}_{H2}}{\dot{m}_{air}} = f_{ST} = 0.029$.

Given the first assumption, it is not necessary to write the mixer equations. However, it is still necessary to evaluate the thermophysical properties of the mixture which is done in the following way.

$$c_{p_{mix5}} = \frac{c_{p_{air4}}\dot{m}_4 + c_{p_{H2}}\dot{m}_{H2}}{\dot{m}_4 + \dot{m}_{H2}}$$

(3-25)

The isovolumic specific heat and the adiabatic expansion coefficient are calculated in an analogous manner.

Combustion chamber

The combustion efficiency η_b and the pneumatic combustor efficiency ϵ_b had to be assumed conventionally, equal respectively to 0.9 and 0.95. The combustor outlet temperature has been calculated by means of the energy balance equation during the combustion obtaining:

$$T^\circ_6 = T^\circ_5 + \eta_b \left(\frac{f_{ST}}{1 + f_{ST}} \frac{H_i}{c_{p_{gas56}}} \right)$$

(3-26)

Where H_i is the lower calorific value of molecular hydrogen and $c_{p_{gas56}}$ is the average specific heat between conditions 5 for the mixture and 6 for the combustion products, considering them to be made by the 75% in mass of nitrogen and 25% by water.

Regarding the pressure, it holds:

$$p^\circ_6 = \epsilon_b p^\circ_5$$

(3-27)

Nozzle

The most important assumption made regarding the nozzle is that it is always adapted, that is $p_e = p_0$, where p_e is the pressure at the exit of the nozzle and p_0 is the ambient pressure at that altitude. This hypothesis simplifies a lot the modeling of the nozzle but it also overestimates the thrust produced since it can be demonstrated that an adapted nozzle produces the maximum thrust, given that all the other parameters are the same.

A pneumatic efficiency, that takes into account the total pressure losses due for example to viscosity effects near the walls, was introduced, as well as a nozzle efficiency which were conventionally put equal to respectively $\epsilon_n = 0.98$ and $\eta_n = 0.95$. The exit velocity is then evaluated with the following formula:

$$w_e = \sqrt{2 c_{p_{gas6}} T_6^\circ \left(1 - \beta^{\frac{\gamma_{gas6}-1}{\gamma_{ga}}} \right)}$$

(3-28)

Where β is the ratio between the exit pressure and the total nozzle pressure that is equal to the total chamber pressure times the pneumatic efficiency.

Then the performance parameters were evaluated to compare them with the values published by R.E.L.: in particular the gross and uninstalled thrust (F_g, F_u) were considered, as well as the specific thrust T_{sp} and the specific impulse I_{sp}.

$$F_g = \eta_n \dot{m}_6 w_e \quad (3\text{-}29)$$

$$F_u = F_g - \dot{m}_1 u \quad (3\text{-}30)$$

$$I_{sp} = F_u / \dot{m}_{H2} \quad (3\text{-}31)$$

$$T_{sp} = F_u / \dot{m}_1 \quad (3\text{-}32)$$

3.2.2 Input data

The following table summarizes the input data necessary for the model to run, with the values used in the computation and comparison with SABRE data and the sources they were taken from. Where "from REL" is added to the source, it means that the values reported in the source are actually those published by Reaction Engine Limited.

	Parameters	Value	Source	Notes
Preliminary	*Free stream Mach number* M_0	0-5	(Fernandez-Villace, 2013), from REL	
	z, altitude	0-25000 m	(Fernandez-Villace, 2013), from REL	
	Air mass flow, $\dot{m}_1$	90.1 kg/s	(Fernandez-Villace, 2013)	supposed constant
Intake	*Intake kinetic efficiency*, η_k	0.9	(Fernandez-Villace, 2013)	
Precooler	*PC pneumatic efficiency,* ϵ_{PC}	72%	(Fernandez-Villace, 2013)	supposed constant
	PC outlet temperature, $T°_3$	97K	(Fernandez-Villace, 2013)	supposed constant
Air compressor	*AC efficiency* η_{AC}	0.8	(Moino, 2021)	Hypothesis
	AC pressure ratio β_{AC}	122	(Fernandez-Villace, 2013)	supposed constant
CC	*Combustion efficiency* η_b	0.9	(Moino, 2021)	Hypothesis
	Pneumatic combustor efficiency ϵ_b	0.95	(Moino, 2021)	Hypothesis
	Lower calorific value H_i	120.9e6 J/kg	(Moino, 2021)	
Nozzle	*Pneumatic efficiency* ϵ_n	0.98	(Moino, 2021)	Hypothesis
	Nozzle efficiency η_n	0.95	(Moino, 2021)	Hypothesis

Table 1: input data for the ramjet with precooler and compressor model

3.2.3 Results

Hereby the graphs of the performance along the ascent are reported: in particular, the thrust, specific impulse and specific thrust are compared to the values reported by R.E.L.; moreover, an error for each parameter was computed. For example, for the gross thrust the error is:

$$\mathrm{err}_{F_g} = \frac{F_g - F_{g_{REL}}}{F_{g_{REL}}} \tag{3-33}$$

and it is analogous for the other figures.

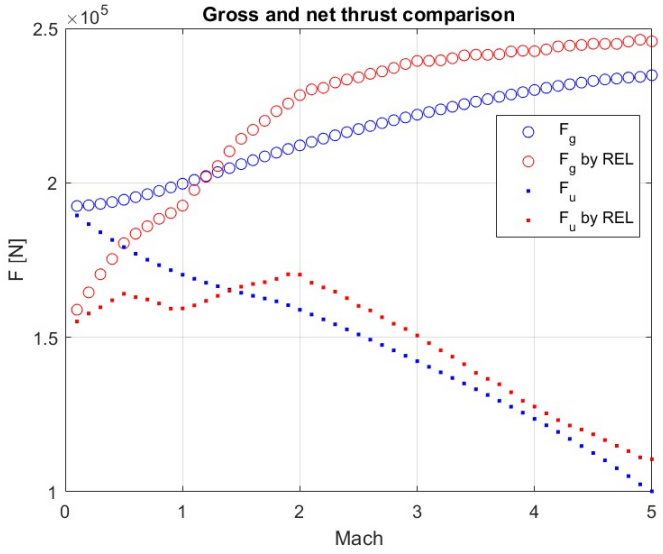

Figure 3.4: Gross and uninstalled thrust comparison for the ramjet with precooler and compressor model

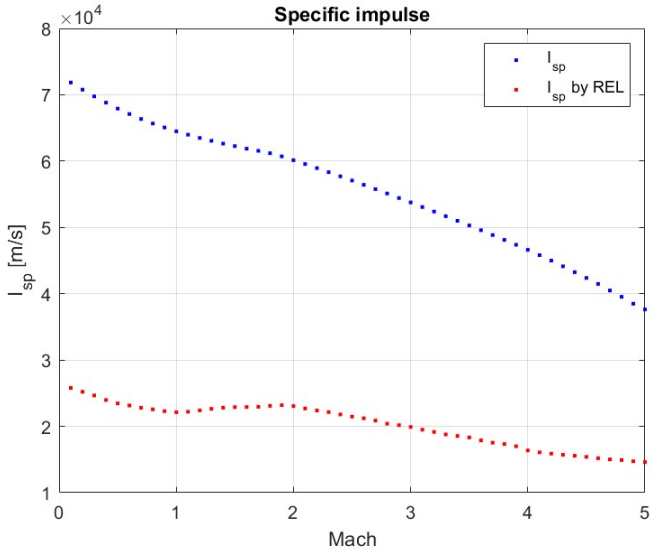

Figure 3.5: Specific impulse for the ramjet with precooler and compressor model

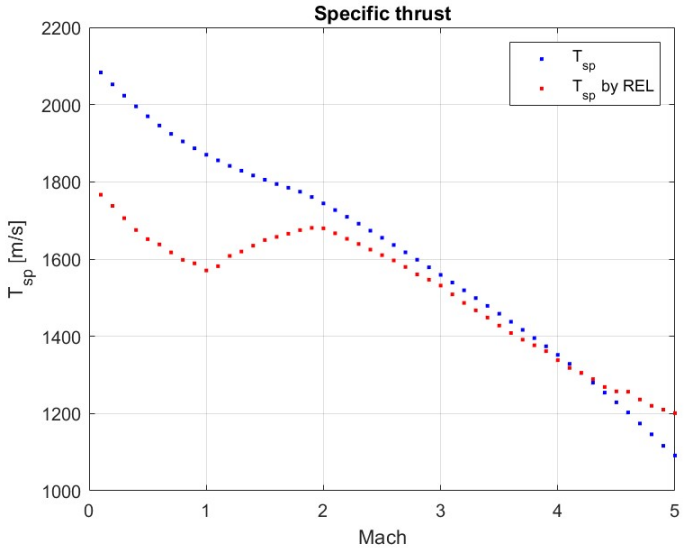

Figure 3.6: Specific thrust for the ramjet with precooler and compressor model

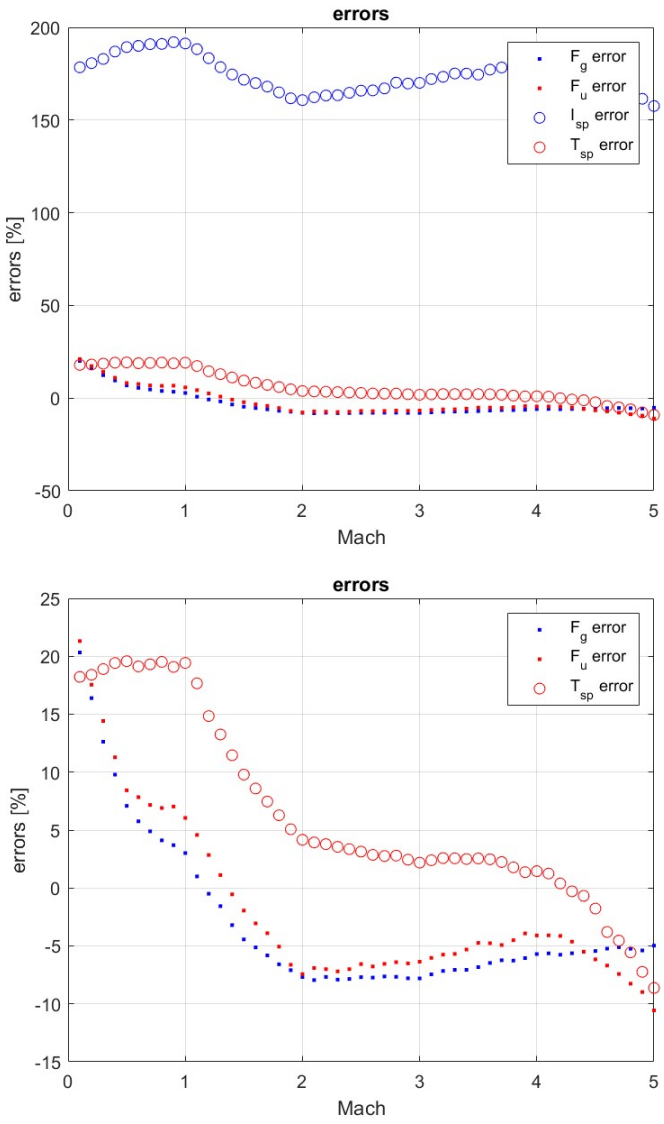

Figure 3.7: errors in the ramjet with precooler and compressor model

As it can be seen in the graphs, the model behaves well in predicting the thrust and specific thrust, especially in the later part of the trajectory: this is due to the fact that in the real engine, after the initial phase the parameters reach the design point values that were used here to obtain the results. In particular, the maximum absolute value of the errors for the gross, net and specific thrust are respectively 20.33%, 21.31% and 19.56%. Despite these results, the model fails completely in predicting the specific impulse. This is due to the assumption made regarding the fuel ratio: it was here assumed that it was equal to the stoichiometric fuel ratio, but it is well established that the SABRE runs with a rich mixture of air and hydrogen in order to accomplish the cooling aspects with the auxiliary cycles of hydrogen and helium that here were completely discarded. This in turn affects the specific impulse giving a maximum error of 193%. This problem is addressed in the following models.

3.3 Complete air cycle

The following model introduces some new elements to the previously described cycle, namely the pre burner and the secondary heat exchanger. The scheme is reported in Figure 3.8.

3.3.1 Thermodynamic cycle

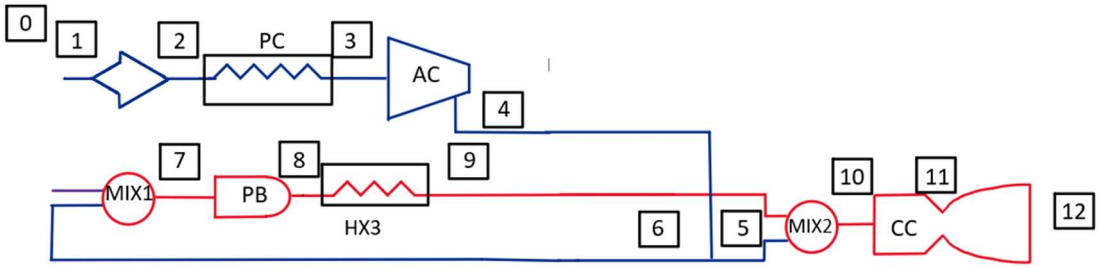

Figure 3.8: complete air cycle scheme

As can be seen in this scheme, this model is still a simplification of the real SABRE cycle and it represents the path followed by air and combustion gases without taking into account the auxiliary cycles of fuel and helium. In addition to the steps described before, here what happens after the compression in AC is the following:

- 4 – 5/6: the air in split into two mass flows that goes in the first mixer or in the second mixer.
- 6 – 7: in the first mixer the air is mixed with all the hydrogen that feds the engine, creating a rich mixture.
- 7 – 8: the mixture is burnt in the first stage of the combustion process in the preburner: the temperature increases and the outlet gases are composed mainly by water vapour, nitrogen and hydrogen that is not burnt because of the lack of enough oxidant.

- 8 – 9: the gases go through the second heat exchanger where they are cooled down by the helium stream on the other side. The reason for this to happen will be better explained later and is linked to the helium cycle functioning.
- 9 – 10: here the combustion gases that are still rich in hydrogen are mixed with the remaining part of air mass flow, giving again a rich mixture of hydrogen and air, with water vapor and molecular nitrogen.
- 10 – 11: this is the principal combustion chamber where the oxygen contained in the mixture is consumed in a quasi-isobaric combustion, as before.
- 11 – 12: finally, the air is expanded in the nozzle, which is here considered non adapted, as in the real case, differently from the previous model.

In the following part, the relations used in each component are reported, with a particular attention on those that are different from the ramjet with precooler and compressor model.

The precooler and air compressor are treated in the exact same way as before thus it is possible to refer to the equations in 3.2.1, that are not written here.

Intake

In order to reduce the uncertainties in the model, the intake was here modeled as the real SABRE intake studied in (Fernandez-Villace, 2013). The total pressure recovery factor is reported in Figure 3.9 for varying Mach number and altitude.

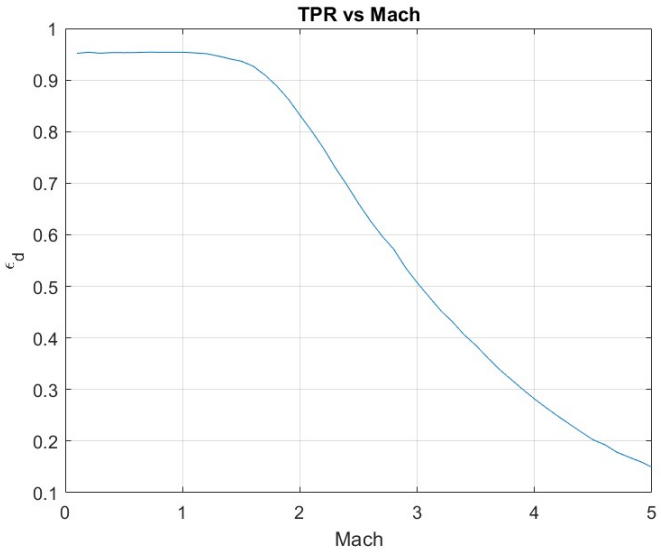

Figure 3.9: total pressure recovery of the real intake along the trajectory

CC – PB node

As said before, after the air compressor, the air reaches what was called CC – PB node which is simply the point at which it is divided into two mass flows that goes to the pre-burner or the combustion chamber. Here the most important aspect is to establish how much air flows directly in the combustion chamber and how much goes to the pre-burner. To do so it was noted that in (Fernandez-Villace, 2013), at the design point the mass flow is exactly split in half and the same assumption was made here, in addition to that of considering this ratio constant.

$$\dot{m}_6 = \frac{\dot{m}_{PB}}{\dot{m}_{tot}} \dot{m}_1$$

(3-34)

$$\dot{m}_5 = \dot{m}_1 - \dot{m}_6$$

(3-35)

where $\frac{\dot{m}_{PB}}{\dot{m}_{tot}} = 0.5$.

Mixer 1

In the first mixer the total amount of hydrogen needed by the engine is mixed with half of the air ingested: this could be enough to consider the mixture rich in fuel, but in addition to this it must be noted that the SABRE runs with an overall fuel to air ratio higher than the stoichiometric ratio, for reasons related to the cooling of the incoming air, as stated previously. Thus, in this model the real fuel equivalence ratio was used, differently from the previous model where this parameter was set to 1. In particular, as it will be seen later, this model was used to evaluate the results in two different cases: the first one in which the parameters are considered constant and equal to the design point values as before, in order to see the influence of the non-adapted nozzle and of the pre-burner; in the second case the parameters were varied along the trajectory according to the data published by Reaction Engines Ltd or reported in (Fernandez-Villace, 2013). In particular, regarding the equivalence ratio Φ, it varies linearly along the ascent from 2.5 to 2.8, that is the design point value.

The equations used in this stage are:

$$f = \Phi f_{ST}$$

(3-36)

$$\dot{m}_H = f \dot{m}_1$$

(3-37)

$$\dot{m}_7 = \dot{m}_6 + \dot{m}_H$$

(3-38)

Regarding the hydrogen total temperature and pressure, as before, they were assumed to be equal to those of the air in station 4. This is verified by the fact that also in (Fernandez-Villace, 2013) the values of air and hydrogen are nearly equal.

$$T^\circ_H = T^\circ_4$$

(3-39)

$$p^\circ_H = p^\circ_4$$

(3-40)

Given this assumption, it is not necessary to write the mixer equations, but it is necessary to evaluate the thermodynamic properties of the mixture as done before.

For example, for the isobaric specific heat (it is analogous for the other properties):

$$c_{p_7} = \frac{c_{p_4}\dot{m}_6 + c_{p_H}\dot{m}_H}{\dot{m}_6 + \dot{m}_H}$$

(3-41)

Pre-burner

In the pre-burner the rich mixture is burnt. In order to evaluate the outlet temperature, it is assumed that all the air burns with an amount of hydrogen corresponding to the one that gives a stoichiometric fuel ratio. Thus, in the outlet the composition will be a mixture of nitrogen, unburnt hydrogen and water vapor at high temperature and pressure, disregarding the reactions between hydrogen and nitrogen. The exit temperature and pressure are thus evaluated as follows:

$$T^\circ{}_8 = T^\circ{}_7 + \eta_b \frac{f_{ST}}{1 + f_{PB}} \frac{H_i}{c_{p_{78}}}$$

(3-42)

$$p^\circ{}_8 = p^\circ{}_7 \epsilon_b$$

(3-43)

Where η_b, ϵ_b are defined as before and $f_{PB} = \dot{m}_H/\dot{m}_6$.

Heat exchanger 3

Regarding HX3, an assumption like that made for the precooler was made, thus considering the outlet temperature constant and equal to the design value, that was taken from (Fernandez-Villace, 2013). Regarding the total pressure instead, it was assumed to remain constant along the flow through the heat exchanger, in a similar manner to what is done in (Jianqiang Zhang, 2017).

$$Q_{HX3} = \dot{m}_8 c_{p_{89}} (T^\circ{}_9 - T^\circ{}_8)$$

(3-44)

$$p^\circ{}_9 = p^\circ{}_8$$

(3-45)

Mixer 2

In the second mixer it is necessary to evaluate both the thermophysical properties of the outlet mixture, which will be composed by the same elements described before with the added fresh air, and also the outlet temperature and pressure conditions.

$$T_{10}{}^\circ = \frac{\dot{m}_5 c_{p_{air4}} T_4{}^\circ + \dot{m}_8 c_{p_{gas9}} T_9{}^\circ}{\dot{m}_5 c_{p_{air4}} + \dot{m}_8 c_{p_{gas9}}}$$

(3-46)

$$p_{10}{}^{\circ} = \frac{\dot{m}_5 p_4{}^{\circ} + \dot{m}_8 p_9{}^{\circ}}{\dot{m}_5 + \dot{m}_8}$$

(3-47)

$$c_{p_{gas10}} = \frac{\dot{m}_5 c_{p_{air4}} + \dot{m}_8 c_{p_{gas9}}}{\dot{m}_5 + \dot{m}_8}$$

(3-48)

$$c_{v_{gas10}} = \frac{\dot{m}_5 c_{v_{air}} + \dot{m}_8 c_{v_{gas9}}}{\dot{m}_5 + \dot{m}_H}$$

(3-49)

$$\gamma_{gas10} = c_{p_{gas10}} / c_{v_{gas10}}$$

(3-50)

$$\dot{m}_{10} = \dot{m}_5 + \dot{m}_8$$

(3-51)

Regarding the pressures the equation was used even if the differences between the two are always around 5% and thus negligible.

Combustion chamber

In the combustion chamber the mixture is once again rich in hydrogen thus the same hypothesis made for the pre-burner is made here, considering that only a fraction of the hydrogen corresponding to the stoichiometric fuel ratio burns.

The equations are:

$$T_{11}{}^{\circ} = T_{10}{}^{\circ} + \eta_b \frac{\left(f_{ST} \dot{m}_5 H_i / c_{p_{gas1011}}\right)}{\dot{m}_5 + \dot{m}_6 (1 + f_{PB})}$$

(3-52)

$$p_{11}{}^{\circ} = p_{10}{}^{\circ} \epsilon_b$$

(3-53)

Nozzle

Here the modeling of the nozzle is more complicated since, as said before, it considered non adapted, i.e. $p_e \neq p_0$, that is to say that the exit pressure is in general different from the ambient pressure at a certain altitude except from one particular point at which the nozzle is adapted. For the sake of simplicity here the thermal properties of the gas are considered constant during the expansion.

First of all, $p^{\circ}{}_{12} = p^{\circ}{}_{11} \epsilon_n$, where the nozzle pneumatic efficiency is the same as before. Then the nozzle area ratio needs to be known: in theory this is a fixed value given by the ratio between the area at the end of the nozzle and the throat area; however what is useful to know for the evaluation of the thrust is the nozzle area ratio at the separation point, that

is to say the ratio between the area of the nozzle at the point at which the flow detaches from the wall and the throat area. In fact, as reported in (Fernandez-Villace, 2013), $F_g = \dot{m}_{11} w_e + (p_{sep} - p_0) A_{sep}$ where the subscript "sep" stands for the separation conditions. The area ratio at separation, *AR*, is computed by (Fernandez-Villace, 2013), by applying the Summerfield criterion, that is to say that the jet detaches from the nozzle wall when the pressure is as low as the 30% of the ambient pressure. The values are assumed to be the same here and the plot of the *AR* along the trajectory is here reported.

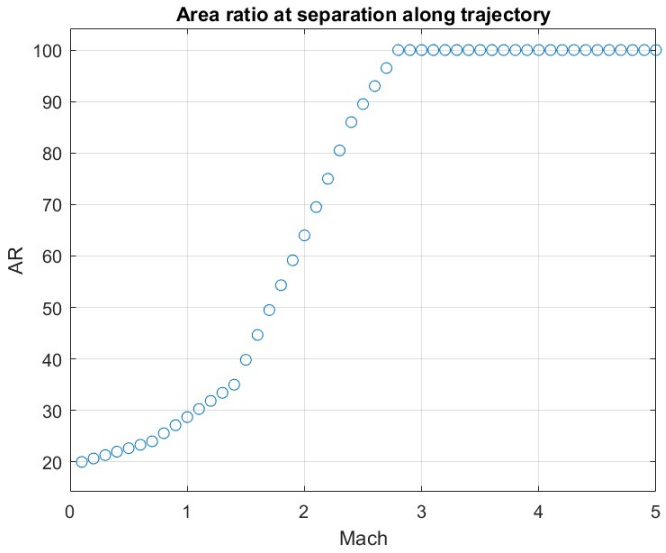

Figure 3.10: area ratio at separation along trajectory

As can be seen the flow separates inside the nozzle until the free stream Mach number is almost 3: after this point the nozzle runs full but the flow is still overexpanded until it reaches M=4.5 at 23 km of altitude. This datum was used to estimate the nozzle throat area through the following equation which is the equation for the mass flow in the throat assuming that the flow is sonic.

$$A_t = \dot{m} \frac{\sqrt{R_{gas} T_{11}{}^\circ}}{\sqrt{\gamma_{gas11}} * p_{11}{}^\circ} \left(1 + \frac{\gamma_{gas11} - 1}{2}\right)^{\frac{\gamma_{gas11}+1}{2(\gamma_{gas11}-1)}} = 0.0122 m^2$$

(3-54)

Now it is possible to calculate the area at separation: $A_{sep} = AR A_t$.

The other variable that needs to be known is the ratio between the exit and chamber pressure β, that appears in the equation

$$w_e = \sqrt{2 c_{p_{gas11}} T_{11}{}^\circ \left(1 - \beta^{\frac{\gamma_{gas11}-1}{\gamma_{gas11}}}\right)}$$

(3-55)

used to calculate the exit velocity, where, differently from before, it is not possible to calculate the ratio assuming $p_e = p_0$. In order to do so the following equation of the mass flow at the separation area had to be solved iteratively using Newton's method:

$$\sqrt{\beta^{\frac{2}{\gamma_{gas11}}} - \beta^{\frac{\gamma_{gas11}+1}{\gamma_{gas11}}}} - \dot{m}_{10}\frac{\sqrt{R_{gas}T_{11}{}^{\circ}}}{p_{11}{}^{\circ}A_{sep}}\sqrt{\frac{\gamma_{gas11}-1}{2\gamma_{gas11}}} = 0$$

(3-56)

It is now possible to calculate the performance parameters as done before.

3.3.2 Input data in the cases of constant and variable parameters

As stated before, the same model is used with two slightly different sets of input data in order to see separately the influence of the pre-burner, heat exchanger and non-adapted nozzle and that of the varying parameters along the trajectory.

	Parameters	Value	Source	Notes
Preliminary	*Free stream Mach number* M_0	0-5	(Fernandez-Villace, 2013), from REL	
	Altitude z	0-25000m	(Fernandez-Villace, 2013), from REL	
	Air mass flow $\dot{m}_1$	90.1 kg/s	(Fernandez-Villace, 2013)	supposed constant
Intake	*Intake total pressure recovery* ϵ_d	0.15–0.95	(Fernandez-Villace, 2013)	
Precooler	*PC pneumatic efficiency,* ϵ_{PC}	72%	(Fernandez-Villace, 2013)	supposed constant
	PC outlet temperature, $T°_3$	97K	(Fernandez-Villace, 2013)	supposed constant
Air compressor	*AC efficiency* η_{AC}	0.8	(Moino, 2021)	Hypothesis
	AC pressure ratio β_{AC}	122 kg/s	(Fernandez-Villace, 2013)	supposed constant
Node CC-PB	$\frac{\dot{m}_{PB}}{\dot{m}_{tot}}$	0.5	(Fernandez-Villace, 2013)	supposed constant
Mixer 1	*fuel/air equivalence ratio* Φ	2.8	(Fernandez-Villace, 2013), from REL	supposed constant
Pre-burner	*Combustion efficiency* η_b	0.9	(Moino, 2021)	Hypothesis
	Pneumatic efficiency ϵ_b	0.95	(Moino, 2021)	Hypothesis
	Lower calorific value, H_i	120.9e6 J/kg	(Moino, 2021)	
HX3	*Outlet total temperature* $T°_9$	1174	(Fernandez-Villace, 2013)	supposed constant
Nozzle	*Pneumatic efficiency* ϵ_n	0.98	(Moino, 2021)	Hypothesis
	Efficiency η_n	0.95	(Moino, 2021)	Hypothesis
	Area ratio at separation AR	20-100	(Fernandez-Villace, 2013)	

Table 2: input data for the complete air cycle model in the constant parameters case

In the second case, the parameters that vary are the air mass flow, the AC pressure ratio and the fuel to air equivalence ratio. The plots of this parameters along the trajectory are here reported and in particular the air mass flow was taken from the model developed by

(Fernandez-Villace, 2013) and it is not the real air mass flow rate but it was the only available. The same holds for the pressure ratio. Instead, the fuel equivalence ratio has the real values published by R.E.L. and it was chosen in the place of the value used in (Fernandez-Villace, 2013), which gives a much richer mixture.

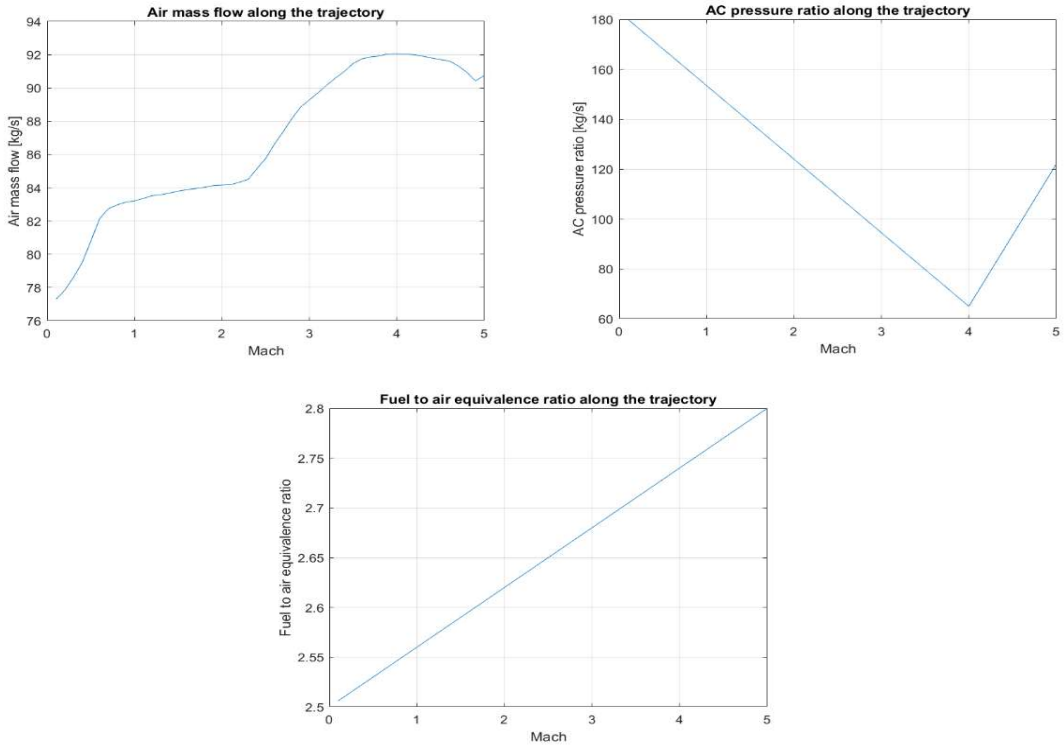

Figure 3.11: varying parameters in complete air cycle model

3.3.3 Results for variable parameters case

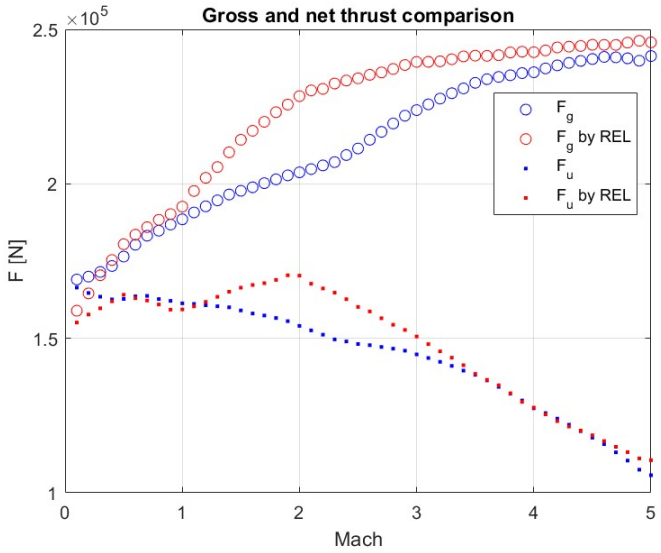

Figure 3.12: Gross and uninstalled thrust comparison for the complete air cycle model with varying parameters

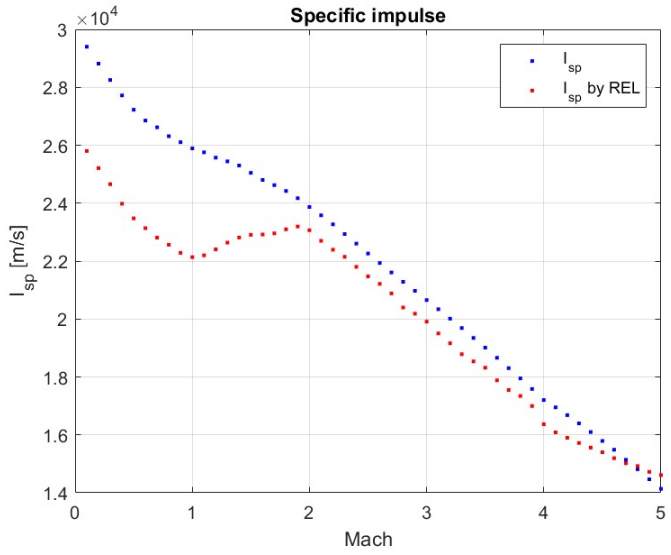

Figure 3.13: specific impulse for the complete air cycle model with varying parameters

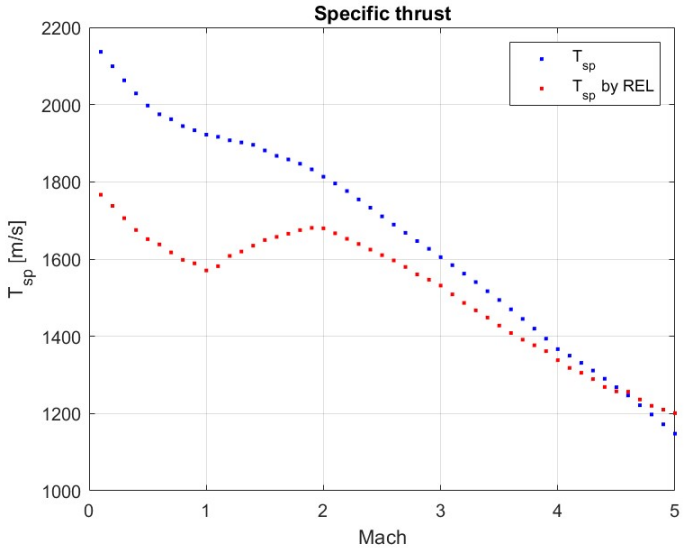

Figure 3.14: specific thrust for the complete air cycle model with varying parameters

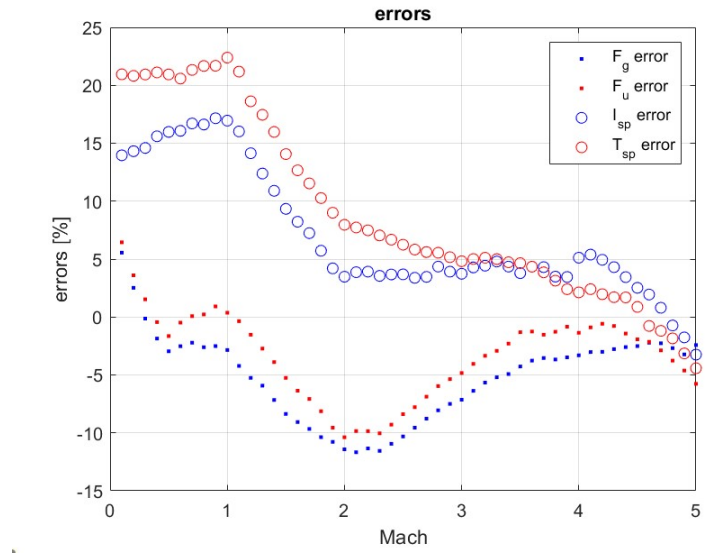

Figure 3.15: errors in the complete air cycle with varying parameters

The performance parameters and errors here reported are calculated in the exact same way as in the model before. The most notable difference between the two models is the error on the specific impulse: the use of a real equivalence ratio has a huge influence on this performance parameter and the maximum absolute value of the error is 17.45%. Regarding the gross and uninstalled thrust, this model also improves their prediction since maximum error is now 11.5% and 10.14% while the previous ones were almost double. Regarding the specific thrust there is a slight increment in the maximum error that reaches 22.7%. However, it must be noted that in the previous model, in the first part of the trajectory the mass flow was higher than the real value thus taking the calculated curve for the specific thrust closer to the one published by REL. This does not happen here, giving then the higher error: this is linked to the fact that the values used for the mass flow are not directly published by REL, whose data are usually hard to find or not available, but are based on the previous calculations made by (Fernandez-Villace, 2013) and can be affected by errors.

3.3.4 Results for constant parameters case

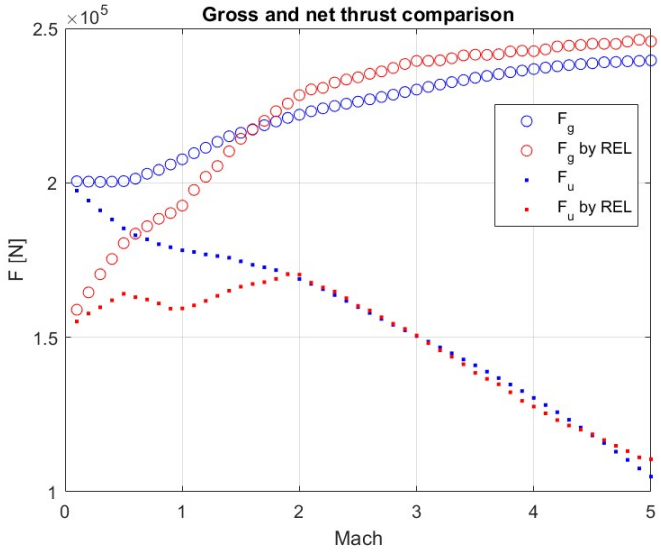

Figure 3.16: gross and uninstalled thrust comparison for the complete air cycle with constant parameters

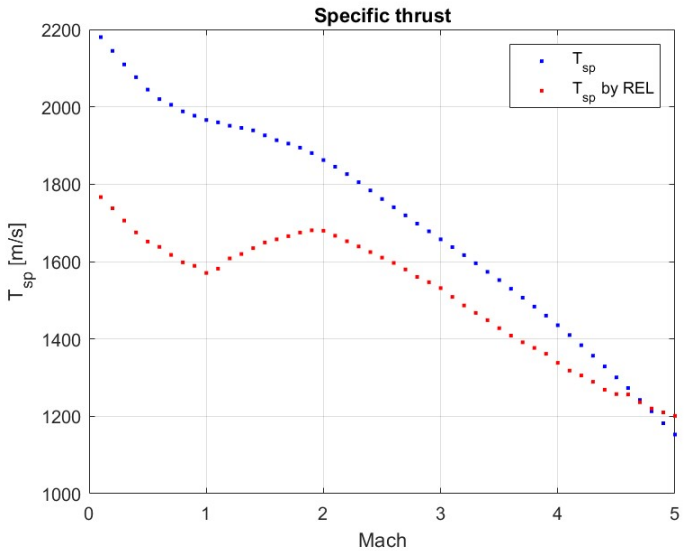

Figure 3.17: specific thrust for the complete air cycle with constant parameters

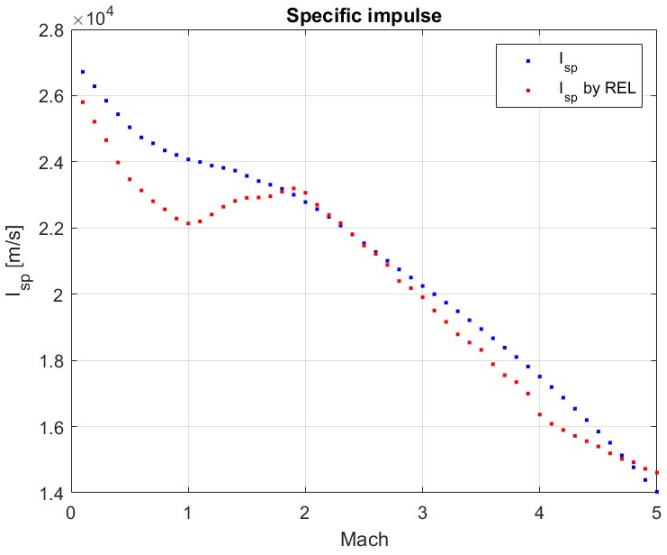

Figure 3.18: specific impulse for the complete air cycle with constant parameters

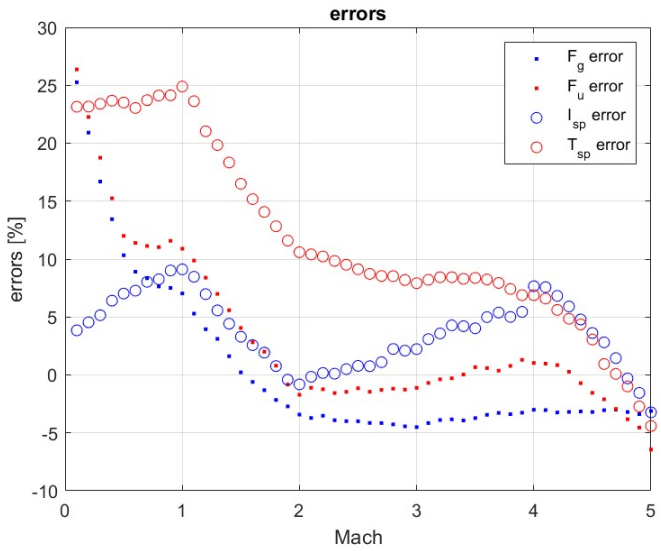

Figure 3.19: errors in the complete air cycle with constant parameters

It can be noted that by using constant parameters the errors increase, especially in the first part of the ascent, where they are the furthest from the design point value used. In particular, the errors increase significantly for the thrust and in a less obvious way for the specific thrust. Regarding the specific impulse, the error is lower in the first part of the trajectory because of the greater amount of hydrogen considered.

3.3.5 Comparison between constant and varying parameters model

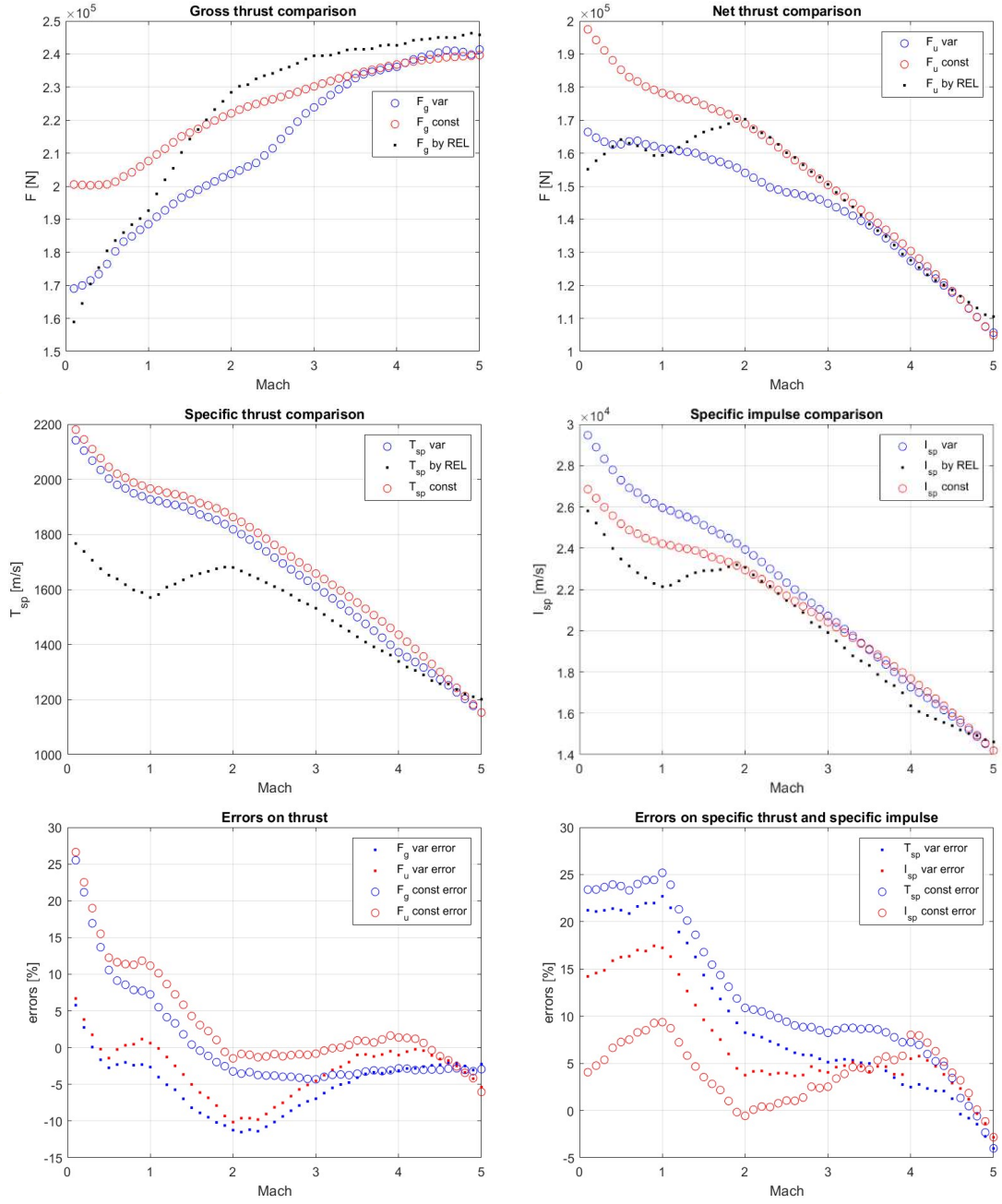

Figure 3.20: comparison between constant and varying parameters case

By comparing the two models with constant and variable parameters side by side, some interesting aspects can be noted. In particular, the two models perform practically the same in predicting the specific thrust and specific impulse and both are affected by a higher error in the first part of the trajectory in which the ramjet burners here neglected are operative. It also looks like the constant parameter model is better in predicting the specific impulse in the first part of the ascent, even if this is due to the higher amount of hydrogen there considered. Regarding the thrust prediction, the models give the same results after Mach 3, where the parameters are closed to the design values used in the constant parameters model. This gives good results after Mach 2 even if it overestimates a lot the ground level thrust.

3.4 Ramjet with fuel cycle model

The model that will be presented in the following is a first attempt to include the fuel cycle without considering the helium loop. In reality, the model represents a different kind of engine and, as it will be demonstrated, it is not capable of predicting the SABRE performance. Moreover, the presence of the secondary hydrogen turbine was firstly considered, but since it gave rise to negative temperatures due to the absence of the pre burner and reheater, it was then neglected. Thus, in the model the power source of the air compressor is not considered and assumed to work properly.

3.4.1 Thermodynamic cycle

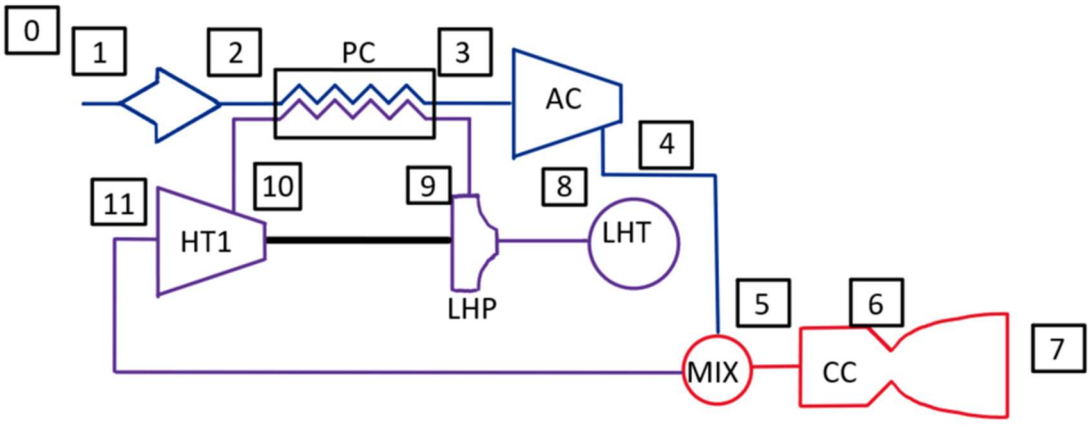

Figure 3.21: ramjet with fuel cycle scheme

Regarding the fuel cycle:

- 8 – 9: the liquid hydrogen is contained in the tank at constant pressure and temperature and is fed in the circuit by a turbopump
- 9 – 10: the hydrogen flows through the precooler where it subtracts heat from the incoming air flow
- 10 – 11: the fuel passes in a turbine that powers the turbopump and it is then fed in the mixer.

Intake, precooler and compressor

In this model the intake is treated as in the first model, with the equation suggested by (Fernandez-Villace, 2013). Moreover, the mass flow is considered constant and equal to 90.1 kg/s. The same holds for the subsequent two components: the outlet temperature of the PC and the compression ratio are considered constant, as done in the first model.

Liquid hydrogen tank

The tank supplies the fuel at constant temperature $T°_8$ and pressure $p°_8$ of 18K and 1 bar, as seen in (Fernandez-Villace, 2013). The thermophysical properties of hydrogen, differently from air, have been considered constant and equal to an average value along

the cycle of 14600 J/(Kg K) for the isobaric specific heat and 1.41 for the adiabatic expansion coefficient.

Turbopump

The compression ratio of the turbopump β_{LHP} is supposed constant and equal to 257, as in (Fernandez-Villace, 2013), while its efficiency is set by hypothesis equal to 0.8. It is possible to write:

$$p°_9 = \beta_{LHP} p°_8$$

(3-57)

$$W_{LHP} = \dot{m}_H \frac{p°_9 - p°_8}{\eta_{LHP} \rho_{H_{mean}}}$$

(3-58)

$$T°_9 = T°_8 + \frac{1 - \eta_{LHP}}{\eta_{LHP}} \frac{W_{LHP}}{\dot{m}_H c_H}$$

(3-59)

Where the hydrogen mass flow is calculated with linearly increasing equivalence ratio from 2.5 to 2.8, $\dot{m}_H = \phi f_{ST} \dot{m}_1$ and c_H and $\rho_{H_{mean}}$ are the hydrogen specific heat and density at average conditions in the turbopump.

Precooler

In the precooler the equations that can be written are the following:

$$T°_{10} = -Q_{PC} / \left(\dot{m}_H c_{P_H}\right) + T°_9$$

(3-60)

$$p°_{10} = p°_9$$

(3-61)

Hydrogen turbine

The efficiency of the hydrogen turbine is set by hypothesis equal to 0.8 and the power produced must be equal to that necessary to the turbopump.

$$W_{HT1} = -W_{LHP}$$

(3-62)

$$T°_{11} = T°_{10} + W_{HT1} / \left(c_{p_H} \dot{m}_H\right)$$

(3-63)

$$\beta_{HT1} = \left(\left(\frac{T°_{11}}{T°_{10}} - 1 \right) \frac{1}{\eta_{HT1}} + 1 \right)^{\frac{-\gamma_H}{\gamma_H - 1}}$$

(3-64)

$$p°_{11} = p°_{10}/\beta_{HT1}$$

(3-65)

The remaining components are treated as in the previous model, considering an adapted nozzle.

3.4.2 Input data

	Parameters	Value	Source	Notes
Preliminary	*Free stream Mach number* M_0	0-5	(Fernandez-Villace, 2013), from REL	
	Altitude z	0-25000m	(Fernandez-Villace, 2013), from REL	
	Air mass flow $\dot{m}_1$	90.1 kg/s	(Fernandez-Villace, 2013)	Supposed constant
Intake	*Intake kinetic efficiency* η_k	0.9	(Fernandez-Villace, 2013)	
Precooler	*PC pneumatic efficiency* ϵ_{PC}	28%	(Fernandez-Villace, 2013)	supposed constant
	PC outlet temperature, $T°_3$	97K	(Fernandez-Villace, 2013)	supposed constant
Air compressor	*AC efficiency* η_{AC}	0.8	(Moino, 2021)	Hypothesis
	AC pressure ratio β_{AC}	122 kg/s	(Fernandez-Villace, 2013)	supposed constant
Liquid Hydrogen Tank	*fuel/air equivalence ratio* Φ	2.5 - 2.8	(Fernandez-Villace, 2013), from REL	
	Tank temperature $T°_8$	18 K	(Fernandez-Villace, 2013)	
	Tank pressure $p°_8$	1 bar	(Fernandez-Villace, 2013)	
Liquid Hydrogen Pump	*Efficiency* η_{LHP}	0.8		Hypothesis
	LHP compression ratio β_{LHP}	257	(Fernandez-Villace, 2013)	Supposed constant
Hydrogen turbine	*Efficiency* η_{HT1}	0.8	(Moino, 2021)	Hypothesis
Combustion chamber	*Combustion efficiency* η_b	0.9	(Moino, 2021)	Hypothesis
	Pneumatic efficiency ϵ_b	0.95	(Moino, 2021)	Hypothesis
	Lower calorific value, H_i	120.9e6 J/kg	(Moino, 2021)	
Nozzle	*Pneumatic efficiency* ϵ_n	0.98	(Moino, 2021)	Hypothesis
	Efficiency η_n	0.95	(Moino, 2021)	Hypothesis

Table 3: input data for ramjet with fuel cycle model

3.4.3 Results

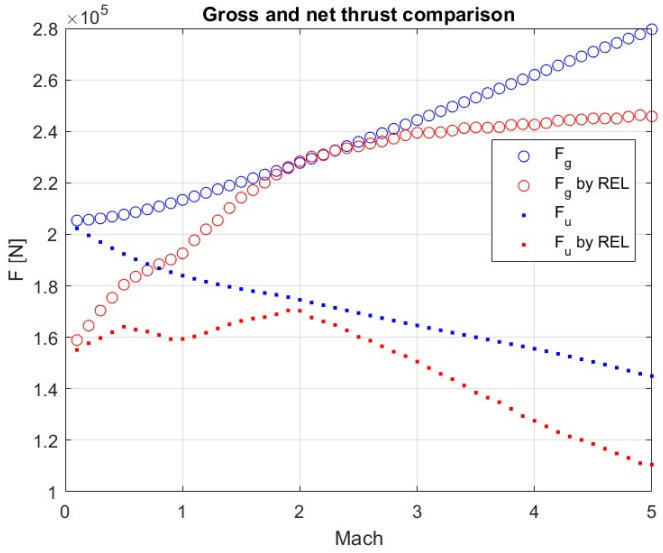

Figure 3.22: gross and net thrust comparison for the ramjet with fuel cycle model

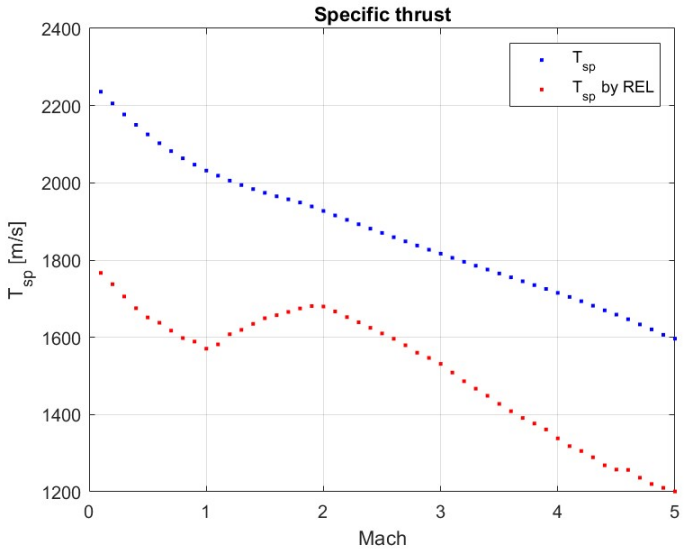

Figure 3.23: specific thrust in the ramjet with fuel cycle model

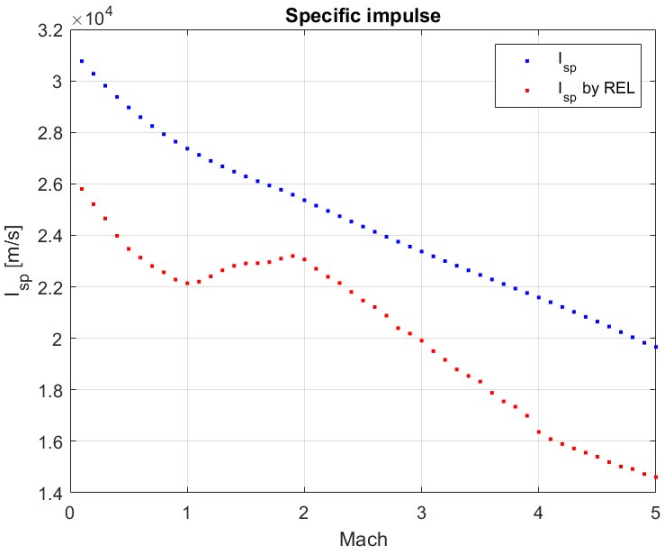

Figure 3.24: specific impulse in the ramjet with fuel cycle model

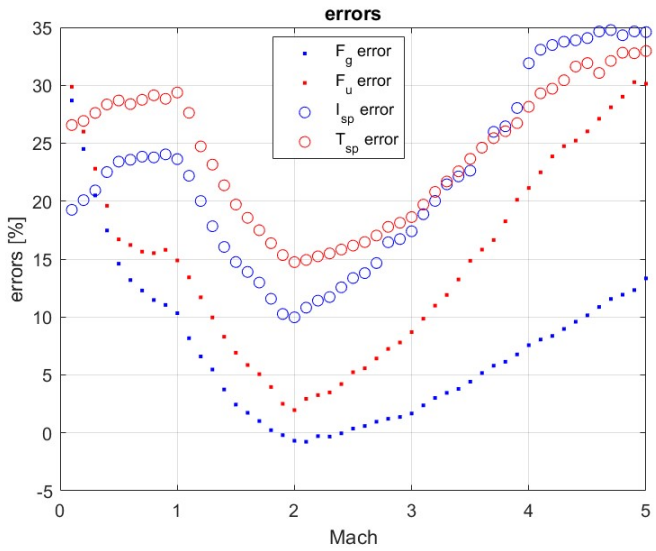

Figure 3.25: errors in the ramjet with fuel cycle model

As said before, this model is not representative of what happens in the SABRE. It could probably be adapted by changing some features like the amount of hydrogen but then again it would not return a realistic image of the engine. However, it could be a good representation of precooled engines in which the helium cycle is absent. Here the errors on specific thrust and impulse never goes under the 10% while the errors on thrust are generally higher than in the previous models, especially at the beginning and end of the air breathing ascent, where the previous model preforms much better. It can be seen that in this model the thrust is constantly overestimated and this is due to the higher temperatures reached by the hydrogen that directly flows in the precooler.

3.5 Complete model

The last model that has been analyzed is the most complete one and it resembles the real thermodynamic cycle of SABRE with insights in the two auxiliary cycles. The scheme is the one illustrated before and it is here reported again.

3.5.1 Thermodynamic cycle

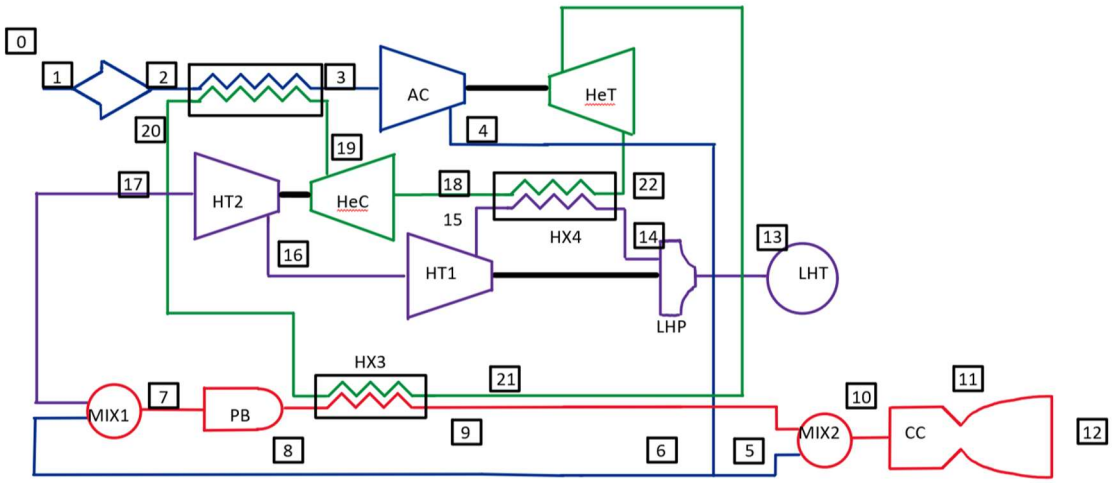

Figure 3.26: cycle scheme of the complete model

In addition to the previous complete air cycle model the helium and hydrogen cycle were introduced.

- 13 – 14: the hydrogen passes from the conditions in the cryogenic tank to the outlet pump conditions.
- 14 – 15: the hydrogen is heated by the helium flow.
- 15 – 16: the hydrogen flows through the first turbine, mechanically linked to the turbopump where it cools down and diminishes its pressure.
- 16 – 17: the hydrogen passes in the second turbine, coupled with the helium compressor, reaching the first mixer inlet conditions.
- 18 – 19: the helium is compressed thanks to the power extracted by the hydrogen turbine in the previous step.
- 19 – 20: the relatively cold helium flows through the precooler where it cools down the air coming from the intake.
- 20 – 21: the helium heats up again in the HX3, thanks to the combustion products of the first stage, in order to feed the following turbine.
- 21 – 22: the hot helium flows through the turbine where its temperature and pressure are taken back to the initial values, while the energy extracted is used to power the air compressor.

In this model the intake, precooler and air compressor were modeled in the same way as in model in 3.3, so the total pressure recovery is the one taken from (Fernandez-Villace, 2013), the temperature after the precooler is fixed and the compressor pressure ratio is varied along the trajectory as before. One key difference from the previous model in the

air part is that the ratio of air that is sent in the pre-burner varies along the trajectory: it is 0.5 until M=1, it increases from 0.5 to 0.6 at M=2 and it decreases linearly to reach the value of 0.45 at M=5; this choice was made because it was noticed that these was the trend that reduced the errors the most. It was seen that using a constant value of 0.5 gives acceptable errors similar to those of the complete air cycle model, thus it is still a good choice in the initial phases of the project or if details of the engine are not available.

After this the following steps were followed.

Helium turbine

First, it was necessary to have the helium mass flow $\dot{m}_{He}$ that was set equal to 22 kg/s, as in (Fernandez-Villace, 2013). As indicated in (Jianqiang Zhang, 2017), the helium turbine inlet temperature was considered a constant design parameter equal to 1190K. Then the following equations were used:

$$W_{HeT} = -W_{AC}$$

(3-66)

$$T°_{22} = T°_{21} + W_{HeT}/\left(c_{p_{He}}\dot{m}_{He}\right)$$

(3-67)

$$\beta_{HeT} = \left(\frac{1}{\eta_{HeT}}\left(\frac{T°_{22}}{T°_{21}} - 1\right) + 1\right)^{\frac{-\gamma_{He}}{\gamma_{He}-1}}$$

(3-68)

Where the first one is the power balance between the air compressor and helium turbine, disregarding mechanical efficiencies, the helium specific heat and expansion coefficient were considered constant as done in (Tayfun Tanbay M. B., 2020) and the last one is the relation between temperatures and pressure ratio in the turbine β_{HeT}.

$$p°_{22} = p°_{21}/\beta_{HeT}$$

(3-69)

The helium mass flow is considered constant, thus the pressure ratio of the turbine varies along the ascent, in order to accomplish to the different requests of the air compressor.

Heat exchanger 4

The helium compressor inlet temperature was set to a constant value of 50 K, as in (Fernandez-Villace, 2013), thus allowing to calculate the varying exchanged heat Q_{HX4} along the trajectory:

$$Q_{HX4} = \dot{m}_{He}c_{p_{He}}(T°_{18} - T°_{22})$$

(3-70)

Then, as done in (Jianqiang Zhang, 2017) the pressure was considered constant through HX4.

Helium compressor

Since in all heat exchangers total pressure could be assumed to remain unchanged, as done by (Jianqiang Zhang, 2017) and showed by (Fernandez-Villace, 2013), the pressure ratio in the compressor must be the same of the turbine, in order to have congruence of pressures in the helium cycle. Thus $\beta_{HeC} = \beta_{HeT}$. Then:

$$T_{19}° = T°_{18}\left(1 + 1/\eta_{HeC}\left(\beta_{HeC}^{\frac{\gamma_{He}-1}{\gamma_{He}}} - 1\right)\right)$$

(3-71)

$$W_{HeC} = \dot{m}_{He} c_{pHe}(T°_{19} - T°_{18})$$

(3-72)

$$p°_{19} = p°_{18}\beta_{HeC}$$

(3-73)

Precooler

Given the heat exchanged Q_{PC} calculated before in the air side of the precooler, it is possile to write

$$T°_{20} = T°_{19} - Q_{PC}/\left(\dot{m}_{He} c_{p_{He}}\right)$$

(3-74)

Heat exchanger 3

It is now possible to estimate the heat exchanged in HX3 along the ascent, which in the previous model was calculated considering a constant outlet temperature on the air side.

$$Q_{HX3} = \dot{m}_{He} c_{p_{He}}(T°_{21} - T°_{20})$$

(3-75)

Moving to the hydrogen cycle, the following path was followed.

Liquid hydrogen tank

The conditions at the tank outlet are considered constant and the values were taken from (Fernandez-Villace, 2013). In order to maintain simplicity, constant specific heats and specific heat ratio were assumed with a value corresponding to an average of the conditions in the cycle ($c_{p_H} = 14600 J/kgK, c_{v_H} = 10290 J/kgK, \gamma_H = 1.42$).

The fuel to air equivalence ratio Φ was chosen, as done before, to vary linearly from 2.5 to 2.8 along the ascent, thus it was possible to calculate the hydrogen mass flow $\dot{m}_H = \Phi f_{ST} \dot{m}_1$ where f_{ST} is the stoichiometric fuel ratio equal to 0.029.

Liquid hydrogen pump

Given the conditions reported in (Fernandez-Villace, 2013), while flowing in the turbopump the hydrogen passes from liquid to supercritical state, while according to those calculated in (Jianqiang Zhang, 2017), the hydrogen remains in the liquid state. Here, for

the sake of simplicity the hydrogen was considered liquid and an average density of $73 kg/m^3$ was assumed. Then a pressure ratio of the turbopump of 257, equal to the value at design point in (Fernandez-Villace, 2013) was chosen and assumed constant during the ascent. It was then possible to calculate the outlet pressure and the power consumed by the turbopump, using an efficiency $\eta_{LHP} = 0.8$.

$$p°_{14} = p°_{13}\beta_{LHP}$$

(3-76)

$$W_{LHP} = \dot{m}_H \frac{p°_{14} - p°_{13}}{\eta_{LHP}\rho_{LH}}$$

(3-77)

$$T°_{14} = T°_{13} + \frac{1 - \eta_{LHP}}{\eta_{LHP}} \frac{W_{LHP}}{\dot{m}_H c_H}$$

(3-78)

HX4

After exiting the pump, the hydrogen flows in the heat exchanger where part of the heat extracted by the helium in the precooler is given off to the hydrogen stream. The exit temperature can be calculated as:

$$T°_{15} = T°_{14} - Q_{HX} \ /\left(\dot{m}_H c_{p_H}\right)$$

(3-79)

Hydrogen turbine 1

Passing to the first hydrogen turbine, the power produced was set equal to that necessary to the turbopump, neglecting once again the mechanical efficiencies while the turbine efficiency was set to 0.8.

$$W_{HT1} = -W_{LHP}$$

(3-80)

$$T°_{16} = T°_{15} + W_{HT} \ /\left(\dot{m}_H c_{p_H}\right)$$

(3-81)

$$\beta_{HT1} = \left(\left(\frac{T°_{16}}{T°_{15}} - 1\right)/\eta_{HT1} + 1\right)^{-\gamma_H/(\gamma_H - 1)}$$

(3-82)

$$p°_{16} = p°_{15}\beta_{HT}$$

(3-83)

Hydrogen turbine 2

First, a turbine efficiency of 0.8 was assumed and the balance of power with the helium compressor was written, neglecting the mechanical efficiencies and then the same procedure used for HT1 was followed, getting as a result the pressure and temperature at the inlet of the first mixer:

$$W_{HT2} = -W_{HeC}$$

(3-84)

$$T°_{17} = T°_{16} + W_{HT2}/\left(\dot{m}_H c_{p_H}\right)$$

(3-85)

$$\beta_{HT2} = \left(\left(\frac{T°_{17}}{T°_{16}} - 1\right)/\eta_{HT2} + 1\right)^{-\gamma_H/(\gamma_H - 1)}$$

(3-86)

$$p°_{17} = p°_{16}\beta_{HT2}$$

(3-87)

Regarding the remaining components, they were treated as in the complete air cycle model, in particular with a non-adapted nozzle.

3.5.2 Input data

	Parameters	Value	Source	Notes
Preliminary	*Free stream Mach number* M_0	0-5	(Fernandez-Villace, 2013), from REL	
	Altitude z	0-25000m	(Fernandez-Villace, 2013), from REL	
	Air mass flow $\dot{m}_1$	77.3 - 92 kg/s	(Fernandez-Villace, 2013)	
Intake	*Intake total pressure recovery* ϵ_d	0.15-0.95	(Fernandez-Villace, 2013)	
Precooler	*PC pneumatic efficiency,* ϵ_{PC}	72%	(Fernandez-Villace, 2013)	supposed constant
	PC outlet temperature, $T°_3$	97K	(Fernandez-Villace, 2013)	supposed constant
Air compressor	*AC efficiency* η_{AC}	0.8	(Moino, 2021)	Hypothesis
	AC pressure ratio β_{AC}	65 - 180	(Fernandez-Villace, 2013)	
Liquid Hydrogen Tank	*fuel/air equivalence ratio* Φ	2.5 - 2.8	(Fernandez-Villace, 2013), from REL	
	Tank temperature $T°_8$	18 K	(Fernandez-Villace, 2013)	

	Tank pressure $p°_8$	1 bar	(Fernandez-Villace, 2013)	
Liquid Hydrogen Pump	*Efficiency* η_{LHP}	0.8		Hypothesis
	LHP compression ratio β_{LHP}	257	(Fernandez-Villace, 2013)	Supposed constant
Hydrogen turbine	*Efficiency* η_{HT1}	0.8	(Moino, 2021)	Hypothesis
Helium turbine	*Efficiency* η_{HeT}	0.8	(Moino, 2021)	Hypothesis
	Turbine inlet temperature $T°_{21}$	1190 K	(Fernandez-Villace, 2013)	constant
Helium compressor	*Compressor inlet temperature* $T°_{18}$	50 K	(Fernandez-Villace, 2013)	Supposed constant
	Compressor efficiency η_{HeC}	0.8	(Moino, 2021)	Hypothesis
Node CC-PB	$\frac{\dot{m}_{PB}}{\dot{m}_{tot}}$	0.45-0.6		
Pre-burner	*Combustion efficiency* η_b	0.9	(Moino, 2021)	Hypothesis
	Pneumatic efficiency ϵ_b	0.95	(Moino, 2021)	Hypothesis
	Lower calorific value, H_i	120.9e6 J/kg	(Moino, 2021)	
Nozzle	*Pneumatic efficiency* ϵ_n	0.98	(Moino, 2021)	Hypothesis
	Efficiency η_n	0.95	(Moino, 2021)	Hypothesis
	Area ratio at separation AR	20-100	(Fernandez-Villace, 2013)	

Table 4: input data for the complete model

3.5.3 Results

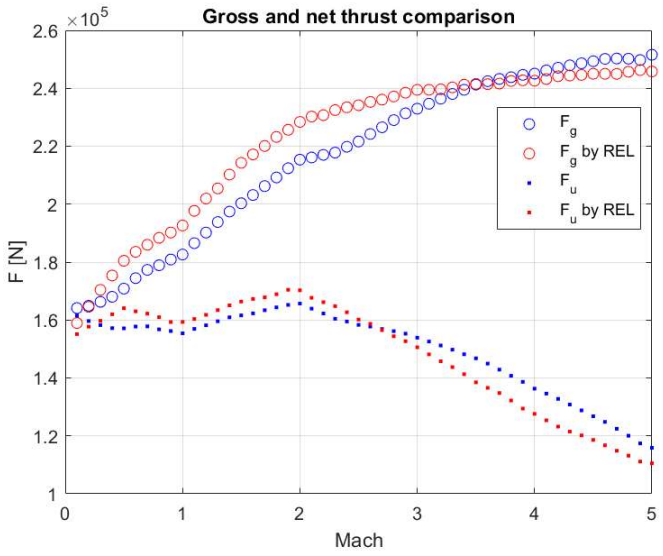

Figure 3.27: gross and net thrust in the complete model

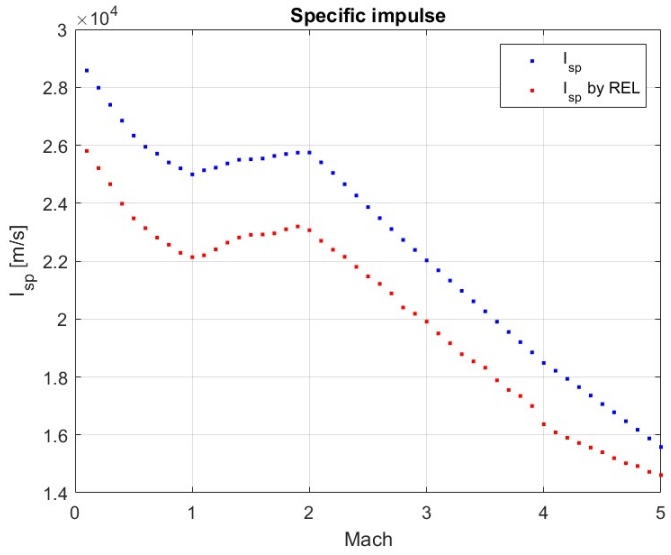

Figure 3.28: specific impulse in the complete model

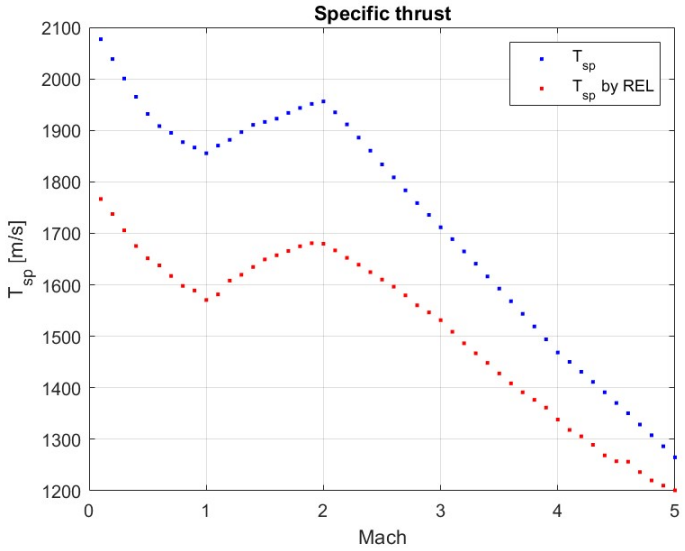

Figure 3.29: specific thrust in the complete model

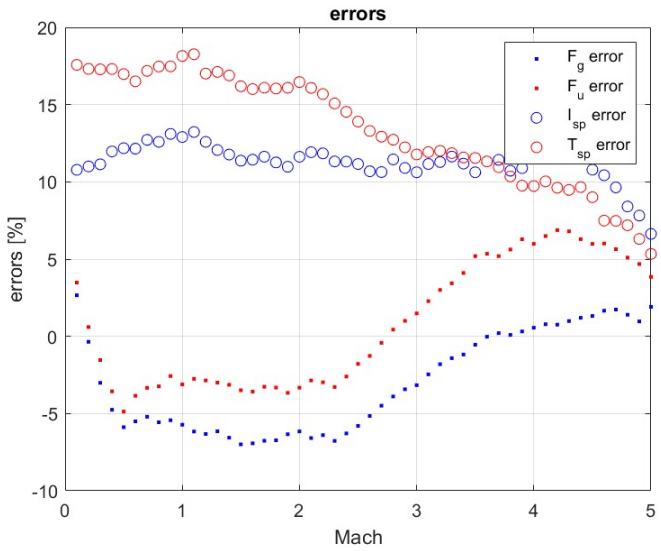

Figure 3.30: errors in the complete model

As it can be noted, in this model the errors are lower: in fact, the maximum error for the gross thrust is a negative 7% while for the net thrust is 6.9%. Also, the maximum error on the specific impulse and thrust are lower and respectively of 13.2% and 18.3%. However, apart from the higher precision, the main advantage of this model is its capacity of giving an insight of what happens in the helium and hydrogen cycles, that were previously neglected, thus allowing for a more complete understanding of the functioning of the engine. Below, tables with the values of pressure and temperature at each station are reported for the design point at M=5 and h=25 km and for four different points at increasing Mach numbers at sea level. Part of these data will be used in the next chapter for the estimation of the emissions.

	M=0.1	**M=0.2**	**M=0.3**	**M=0.4**	**M=5, design**
T°$_1$ [K]	287.7	289.4	292.4	296.5	1210.1
T°$_2$ [K]	287.7	289.4	292.4	296.5	1210.1
T°$_3$ [K]	97.0	97.0	97.0	97.0	97.0
T°$_4$ [K]	493.6	492.6	491.8	491.4	488.7
T°$_5$ [K]	493.6	492.6	491.8	491.4	488.7
T°$_6$ [K]	493.6	492.6	491.8	491.4	488.7
T°$_{17}$ [K]	1169.0	1155.9	1137.9	1117.5	822.2
T°$_7$ [K]	949.5	940.4	927.9	913.8	725.2
T°$_8$ [K]	1851.1	1841.4	1828.7	1814.4	1523.9
T°$_9$ [K]	1059.1	1057.3	1055.6	1053.9	1445.0
T°$_{10}$ [K]	930.7	929.1	927.6	926.1	1209.3

$T°_{11}$ [K]	1593.5	1591.5	1589.5	1587.5	1770.1
$T°_{12}$ [K]	1593.5	1591.5	1589.5	1587.5	1770.1

Table 5: temperature at each station at four points at ground level and at design point

	M=0.1	**M=0.2**	**M=0.3**	**M=0.4**	**M=5, design**
$p°_1$ [bar]	1.0	1.0	1.1	1.1	14.5
$p°2$ [bar]	1.0	1.0	1.0	1.1	2.2
$p°3$ [bar]	0.7	0.7	0.7	0.8	1.6
$p°4$ [bar]	123.5	124.3	126.6	130.7	189.8
$p°_5$ [bar]	123.5	124.3	126.6	130.7	189.8
$p°_6$ [bar]	123.5	124.3	126.6	130.7	189.8
$p°_{17}$ [bar]	203.8	203.3	202.6	201.6	185.3
$p°_7$ [bar]	133.7	134.3	136.2	139.8	189.1
$p°_8$ [bar]	127.0	127.6	129.4	132.8	179.7
$p°_9$ [bar]	127.0	127.6	129.4	132.8	179.7
$p°_{10}$ [bar]	125.4	126.0	128.1	131.8	184.9
$p°_{11}$ [bar]	119.1	119.7	121.7	125.2	175.6
$p°_{12}$ [bar]	116.7	117.4	119.2	122.7	172.1

Table 6: pressure at each station at four points at ground level and at design point

	M=0.1	**M=0.2**	**M=0.3**	**M=0.4**	**M=5, design**
$\dot{m}_1$ [kg/s]	77.3	77.8	78.6	79.5	90.8
$\dot{m}_6$ [kg/s]	38.6	38.9	39.3	39.7	40.8
$\dot{m}_5$ [kg/s]	38.6	38.9	39.3	39.7	49.9
$\dot{m}_H$ [kg/s]	5.6	5.7	5.7	5.8	7.4

Table 7: mass flows at four points at ground level and at design point

3.6 Comparison between the various models along the trajectory

In the previous sections, the four models were presented in detail and it was noted that they could give rise to a high variety of error values along the trajectory and the same model could perform well in one phase and poorly in another phase of the ascent. Moreover it could appear reasonable to use always the last model which is the most complete but some results could be completely similar to those of other simpler models. Thus, in this section graphs comparing the errors of each model are reported in order to discern when it is necessary to increment the precision and when the effort of looking for

more input data is useless or not rewarding in term of accuracy. In this comparison, the ramjet with fuel cycle model presented in section 3.4 is intentionally left out because, as said before, it represents a different concept from that of SABRE and its results are not trustworthy.

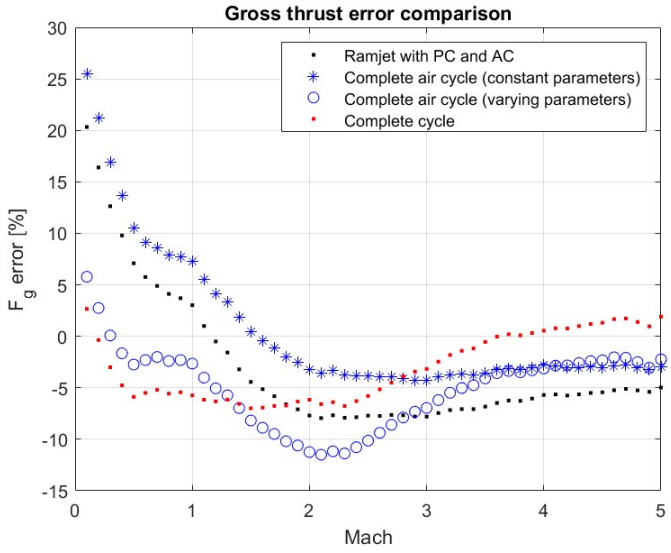

Figure 3.31: gross thrust error comparison

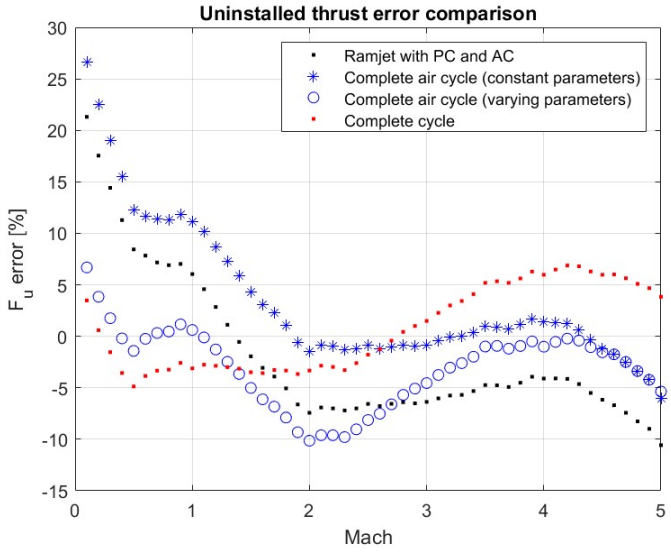

Figure 3.32: uninstalled thrust error comparison

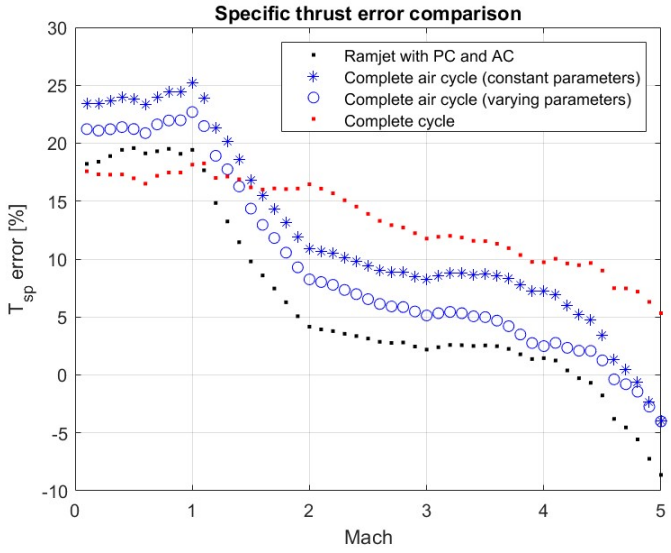

Figure 3.33: specific thrust error comparison

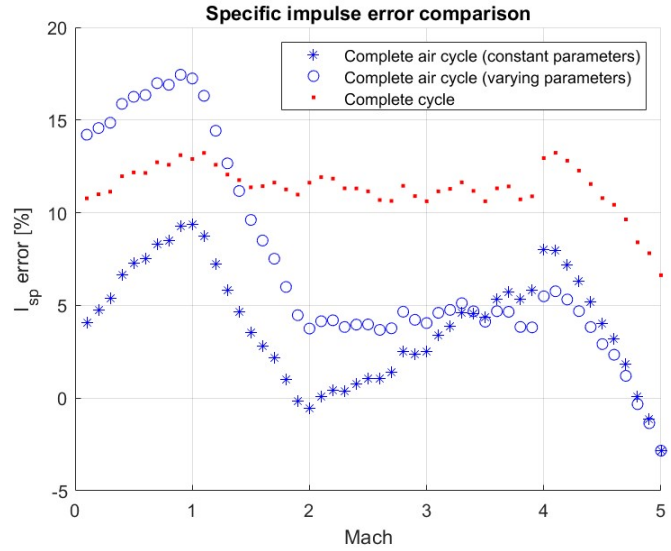

Figure 3.34: specific impulse error comparison

From Figure 3.31, it is possible to see that the ramjet with precooler and compressor model and the complete air cycle with constant parameters model give rise to similar trends for the errors, showing that they are highly inaccurate in subsonic flight. In the same situation actually the simpler model performs better while the situation is reversed around M=1.5. At high Mach flight, all the models give similar results thus showing that in a context in which only on design performance are desired the simpler models can be satisfying. In a wide Mach range however the complete cycle model is the one giving the best results.

Regarding the uninstalled thrust in Figure 3.32, similar considerations can be made and in particular it is interesting how, at high Mach numbers, the complete model gives rise to higher errors with respect to the other, even if it is generally better along all the design space.

In Figure 3.33, it is possible to see that regarding the specific thrust all the models show similar trends and while the complete model is better at low Mach numbers, the simpler models are better again at the end of the ascent.

Finally regarding the specific impulse in Figure 3.34, first it must be noticed that the results given by the first model are neglected because, as said at the end of section 3.2.3, the choice of using a stoichiometric fuel ratio drastically affects the specific impulse with errors around 200% that, if represented, would alter the scale of the plot. Thus, this model should not be used in any case to predict the specific impulse. Regarding the other models, the complete air cycle with constant parameters should not be considered because its results are affected by the assumption of using constant fuel flow equal to the value at the design point which is the highest. Then, from a first look at the two remaining curves, it could appear that the complete air cycle model is better. However, this is due to the fact that all the models overestimates the specific impulse and since the air cycle model underestimates the uninstalled thrust the distance between the calculated specific impulse and the real one is lower, thus giving lower errors than the complete model. However, if one is looking for a first estimate on all the parameters and along all the conditions, the complete model is the one to choose.

4 Greenhouse gases and pollutant emissions estimation

As it was stated in the first chapter, the environmental impact of space exploration is becoming an important matter and it is starting to attract popular interest, in particular with the most recent touristic flights. Despite this, the problem should be taken in consideration, especially for a launcher like Skylon. In fact, as said before, with the development of such a spaceplane, the cost for putting systems in orbit will be drastically reduced in a similar way to which is already happening with the introduction of new reusable launchers, such as those from SpaceX. The lower specific cost could potentially lead to an extremely higher launch frequency, since space could become accessible to a much larger stalls of private industries and stakeholders. Despite the increase in the number of orbiting satellites, which is a completely different problem and matter of concern, also the space related emissions in atmosphere will increase. At present day, they are definitely negligible with respect to other pollutant and greenhouse sources, but, with the desirable reduction of pollution in other fields, they can start to become more relevant.

One example is the scenery depicted in (Erik J.L. Larson, 2016), in which the concepts of using Skylon to build a 3000 GW space based solar power generation system is presented. It is there stated that in order to be economically viable it should require a total of 10^5 launches over 10 years, which is a dramatic growth with respect to the current average number of annual space launches, which is roughly a hundred. It is thus mandatory to explore the impact of such a program, with respect to the advantages of such a power production system.

With all this in mind, the objective of the present chapter is to estimate the chemical emissions of SABRE in terms of both pollutant and climate-changing gases since, after a review of technical literature, an absence of such analysis emerged. Differently from SABRE, the derived engine Scimitar has drawn more attention from this point of view: for example, already in (Varvill, Jivraj, & Paniagua, The Scimitar Precooled Mach 5 Engine), it is stated how the NO_x emissions are of major relevance and also in (Tayfun Tanbay M. B., 2020), they are shown to be relatively high, as a result of the extremely high combustion chamber temperatures. This interest is a result of the LAPCAT program, in which the Scimitar was largely investigated as an advanced propulsion concept, but those results are not applicable to SABRE since the thermodynamic cycles of the two engines are slightly different, just as the applications, and also the conditions in the combustion chambers are dissimilar, where the Scimitar shows higher temperatures and a mixture much closer to the stoichiometric point, which promotes the formation of nitrogen oxides.

Thus, in the following, emissions of greenhouse gases, in our case water vapor, and pollutant gases, that are indicated as NO_x, are estimated for the SABRE, based on the last model developed in the previous chapters, that includes the helium and hydrogen cycle and that is the most accurate along the ascent trajectory.

4.1 Estimation of greenhouse gases emissions

The overall stoichiometric combustion product of hydrogen oxidation is water vapor. In SABRE, as seen in the previous chapter, the combustion is subdivided into two stages and is always in rich conditions.

It is possible to make some considerations on the combustion products even without taking into account the detailed chemistry.

Pre-burner

The Table 1Table 7 at the end of the previous chapter, which is here reported again for the sake of clarity , contains the mass flows of air and hydrogen in different points of the trajectory. For example, at the design point, 40.8 kg/s of air mix with 7.4 kg/s of hydrogen and burn. As stated before, the mixture is fuel rich, thus not all the hydrogen burns but only an amount sufficient to consume all the oxygen present in air. Thus, the outlet composition of the pre-burner will be a mixture of unburnt molecular hydrogen, water vapor and molecular nitrogen (which all together constitutes more than the 99% of the mass of the exhaust gas), plus negligible quantities of compounds of nitrogen and oxygen, hydrogen peroxide, ammonia and so on.

	M=0.1	**M=0.2**	**M=0.3**	**M=0.4**	**M=5, design**
$\dot{m}_1$ **[kg/s]**	77.3	77.8	78.6	79.5	90.8
$\dot{m}_6$ **[kg/s]**	38.6	38.9	39.3	39.7	40.8
$\dot{m}_5$ **[kg/s]**	38.6	38.9	39.3	39.7	49.9
$\dot{m}_H$ **[kg/s]**	5.6	5.7	5.7	5.8	7.4

Table 8: mass flows at four points at ground level and at the design point

The only greenhouse gas that is here produced is the water vapor and the amount that forms is basically proportional to the amount of fuel burnt. Considering the stoichiometric equation of the hydrogen/oxygen combustion $2H_2 + O_2 \leftrightarrow 2H_2O$, we can notice that for each mole of hydrogen burnt, a mole of water is formed. Then, considering the molar mass of the reactants and products, that are equal to $MM_{H_2} = 2.0157\ g/mol$, $MM_{O_2} = 31.999\ g/mol$ and $MM_{H_2O} = 18.015\ g/mol$, it is possible to state that for every gram of burnt hydrogen 8.9373 g of water are formed. Thus, the emission index of water is

$$EIH_2O = 8.9373\ g_{H_2O}/kg_{fuel\ burnt}$$

(4-1)

It is thus possible to calculate the mass flow of water vapor exiting the pre-burner along the trajectory, assumed that the amount of burnt fuel is given by

$$\dot{m}_{H_2burnt} = f_{ST}\,\dot{m}_6$$

(4-2)

Where f_{ST} is the stoichiometric fuel to air ratio and is equal to 0.029, as shown in the plot of Figure 4.1.

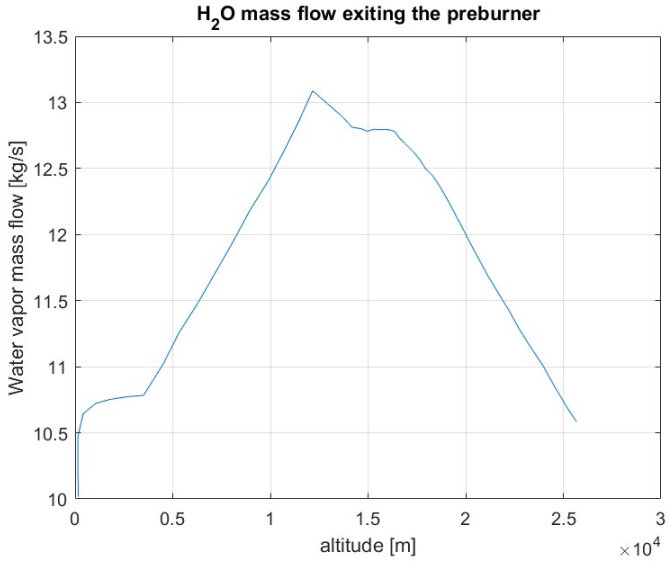

Figure 4.1: mass flow of water vapor exiting the pre-burner

Combustion chamber

The treatment of the combustion chamber is similar: the amount of burnt hydrogen is given by

$$\dot{m}_{H_2burnt} = f_{ST}\,\dot{m}_5$$

(4-3)

And the emission index of water is the same. Below a graph reporting the amount of water produced in the pre-burner, in the combustion chamber and the total mass flow exiting the nozzle is reported, where the total is computed by summing the two values, neglecting the presence of dissociation reactions that could occur in the combustion chamber.

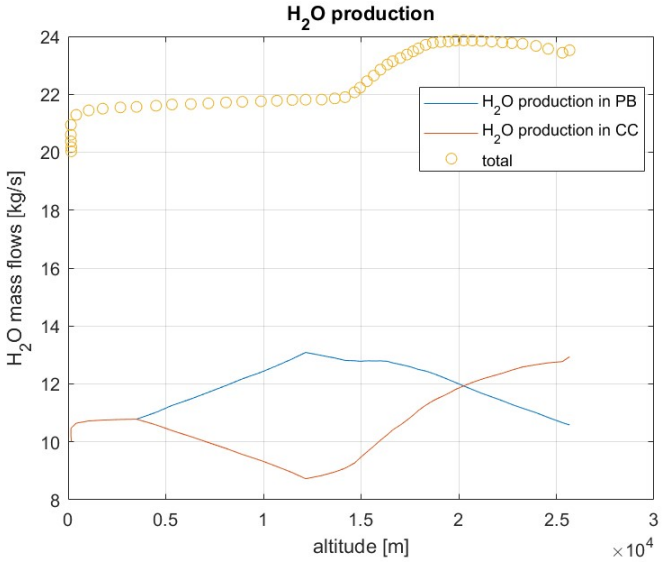

Figure 4.2: water vapor production of SABRE

These results were verified by calculating the water mass ratio at the combustion chamber outlet which is always equal to 0.24 with minor variations. Then, this result was compared to the mass fraction computed using the software Chemical Equilibrium with Applications – CEA by NASA in five different points, at M=0.1, 0.2, 0.3, 0.4 and 5, giving an error lower than 2%, proving the correctness of this method.

Obviously, since there is carbon neither in the fuel nor in the oxidant, the formation of CO_2 is absent and the only greenhouse gas produced is water vapor. It must also be noticed that its climate impact is roughly ten times lower than that of carbon dioxide; however water vapor still has the potential of increasing the radiative forcing (the solar irradiance absorbed by the Earth minus the energy radiated back to space, that is linearly related to the change in mean surface temperature), through the formation of contrails and clouds (Viola, 2020-2021).

The emission estimation of another gas, the molecular hydrogen, is here reported even if it is not a greenhouse gas, because it can be calculated by doing similar considerations, since we have assumed that the water produced is proportional to the fuel burnt and that the only other emitted species is molecular nitrogen, which is here considered as non-reactant. Again, these results were compared with the results calculated with CEA and the errors were around 1% proving the soundness of these assumptions.

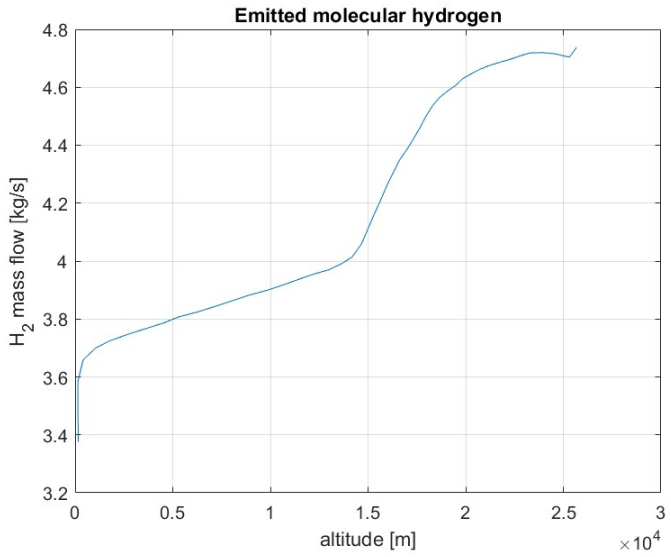

Figure 4.3: mass flow rate of molecular hydrogen leaving the nozzle

4.2 Estimation of pollutant emissions

The major part of the exhaust gas, both from the pre-burner and the combustion chamber, is constituted by N_2, unburnt H_2 and H_2O, which together form more than the 99.5% in mass of the combustion products. However, the engines release also negligible amount of other atomic or molecular species e.g., O, H, H_2O_2, compounds of nitrogen and hydrogen such as NH_2, NH_3 and NNH. Moreover, the combustion processes produce also low quantities of chemical species that can negatively impact on climate and air quality and therefore they are considered pollutants i.e., NO and NO_2. As it will be seen later, the mass fractions of these species are several orders of magnitude lower than those of the three main products. However, for example the nitrogen oxides are usually addressed in the environmental certification of aircrafts and they are considered as air pollutants that decreases the local air quality in the zone surrounding the airport. In terms of certification, they are evaluated at the LTO cycle, namely the four modes of the engine near ground level that are idle, approach, climb out and take off, while no interest is drawn to the cruise phase. This is due to the fact that in the troposphere, where the most of the present aircrafts fly, NO_x does not have a major impact on climate. Instead, they are toxic compounds with effects on the cardiorespiratory system. Moreover, in certain situations at ground level in presence of solar radiation they can react with atmospheric oxygen producing ozone O_3, which again is a toxic compound with proved important effects on the cardiorespiratory, immune and central nervous system. However, inside the ozonosphere, which extends from 15 to 35 km, nitrogen oxides have a different effect of ozone depletion, causing a positive radiative forcing and thus affecting the global climate. Thus, for new supersonic propulsion configurations, like SABRE which works until 25 km in the air – breathing mode, it will become necessary to evaluate the impact of nitrogen oxides emissions.

4.2.1 Notes on NO_x formation

Nitrogen oxides are essentially formed in the majority of combustion processes in which the oxidant is air, even when there is no presence of nitrogen in the fuel. For example, in hydrogen and air combustion, they are generated through the combination between O and N atomic radicals released by the molecular O_2 and N_2 thermal dissociation.

Neglecting the presence of nitrogen and carbon in the fuel, the mechanisms that cause the formation of NO_x are essentially three:

i. Thermal
ii. N_2O
iii. NNH

They are briefly explained here.

Thermal mechanism

The thermal mechanism was the first to be discovered by Zeldovich (Zeldovich, 1946) and is particularly relevant at high temperatures. The initiating reaction is the attack of an oxygen atom on the molecular nitrogen and, because of the high activation energy, this is the rate limiting reaction. Then the nitrogen atoms react with O_2 but in fuel rich mixtures, where oxygen is lacking, the oxidation is due to the reaction with OH radical and the mechanism takes the name of extended Zeldovich mechanism. The global reaction and the three steps are reported below.

$$N_2 + O_2 \leftrightarrow 2NO \tag{4-4}$$

$$N_2 + O \leftrightarrow NO + N \tag{4-5}$$

$$N + O_2 \leftrightarrow NO + O \tag{4-6}$$

$$N + OH \leftrightarrow NO + H \tag{4-7}$$

N_2O and NNH mechanism

Both these mechanisms are due to the recombination of N_2 with atomic oxygen or hydrogen, followed by the oxidation of the nitrogen intermediate. The N_2O mechanism is important in lean conditions at high pressures and moderate temperatures and its steps are reported below.

$$O + N_2 + M \leftrightarrow N_2O + M \tag{4-8}$$

$$N_2O + H \leftrightarrow NO + NH \tag{4-9}$$

$$N_2O + O \leftrightarrow NO + O$$

(4-10)

Then the NH radical may react with OH or O_2 to form NO or react with NO to form N_2 or N_2O recycling the products back to nitrogen.

Finally, the NNH mechanism may be important in fuel rich conditions, and it is composed by the two steps reported below, followed by the oxidation of NH.

$$H + N_2 + M \leftrightarrow NNH + M$$

(4-11)

$$NNH + O \leftrightarrow NH + NO$$

(4-12)

4.2.2 Methods for prediction of nitrogen oxides formation

As explained before, the NO_x formation is usually evaluated in the LTO cycle with four different throttle settings. However, none of these includes the settings and conditions typical of the cruise phase which is obviously predominant during the flight, also because the in-flight measurements are extremely complicated and expensive. Thus, if it is necessary to evaluate the emissions during the whole flight, a different path must be followed and different methods can be used that are based on the emission index at sea level, usually reported in database such as the ICAO emission database (ICAO). In Figure 4.4: scheme of the different available methods for NOx emission prediction below, extracted from (N. Chandrasekaran, 2012), it is possible to see a scheme of the different techniques available that will be briefly explained.

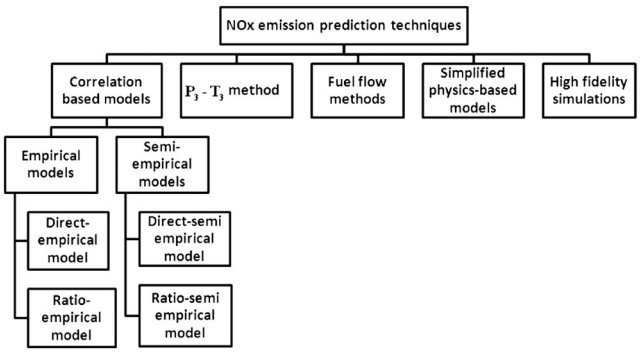

Figure 4.4: scheme of the different available methods for NOx emission prediction

Correlation based models

Correlation based models are classified in empirical and semi-empirical and are based on engine data obtained at ground level. These are the simplest methods that can be used and the empirical ones are based on inlet and outlet conditions of the combustor while the semi-empirical ones include data specific to the model of combustor that is being analyzed. The second classification is made between direct and ratio models: the firsts do not need a measure of the $EINO_x$ at sea level while the seconds do, but this datum is usually available in the ICAO databank. The main disadvantages are related to the high

number and specific input data required, that may be difficult to find. This type of method was not considered for the application to SABRE because of the aforementioned reason.

p3T3 method

This method is the most reliable between the simple prediction techniques that are here presented. It is based on the emission index at sea level which is corrected both with the conditions of the combustor, such as the inlet temperature and pressure and the fuel to air ratio, at sea level and flight level. This method was the one chosen to predict the emissions of SABRE thus it is here explained in detail. First, the inlet conditions of the combustion chambers that are the pressure p3, the temperature T3 and the fuel to air ratio FAR, at sea level are calculated with a simulation of the engine, usually at the four points that are present in the ICAO databank, where also the $EINO_x$ are reported. Then, these four points are plotted and interpolated against the inlet temperature range of the flight. The inlet conditions at flight level are once again calculated by simulating the engine performance and the $EINO_{xSL}$, $p3_{SL}$ and $T3_{SL}$ are determined considered the mentioned plot. Then the $EINO_x$ at flight level is computed using the following correction:

$$EINO_{X\,FL} = EINO_{X\,SL}\left(\frac{p3_{FL}}{p3_{SL}}\right)^{n}\left(\frac{FAR_{FL}}{FAR_{SL}}\right)^{m} exp(H)$$

(4-13)

Where *n* and *m* are two exponents typical of each engine, but they can be usually assumed equal to 0.4 and 0, when no more information are available. *H* is a correction used to take into account the effect of atmospheric humidity and it is equal to

$$H = 19(h_{SL} - h_{FL})$$

(4-14)

with *h* the specific humidity at a given altitude expressed as kg of water per kg of dry air.

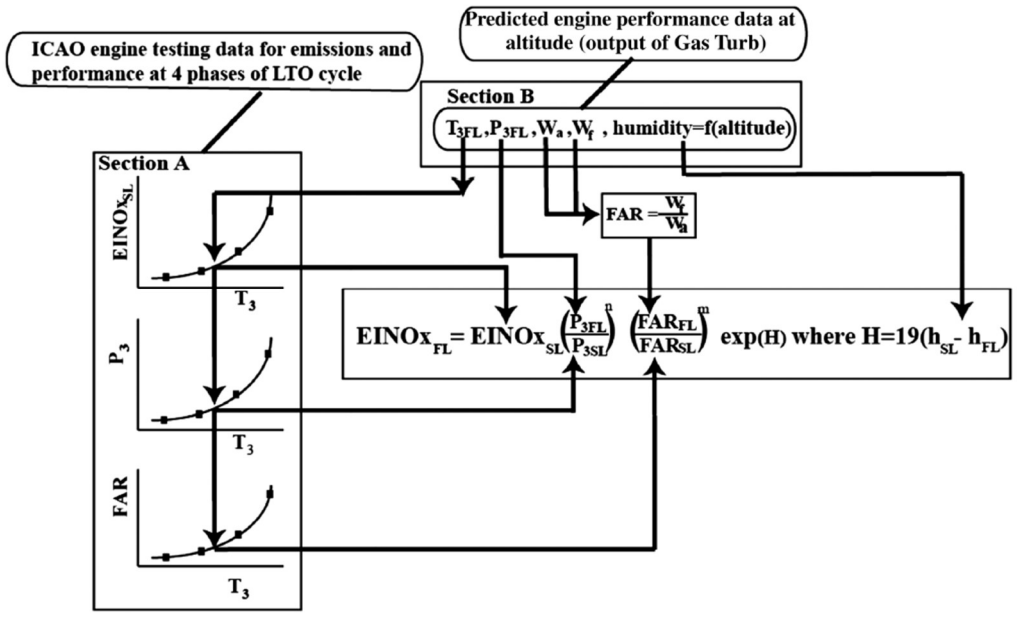

Figure 4.5: scheme of the methodology of the p3T3 technique

Fuel flow methods

Fuel flow methods, such as the DLR and Boeing Fuel Flow Method 2 are derived by the previous technique trying to compensate for the fact that some of the input required are proprietary data not publicly available. First, looking at the four points in the ICAO databank, the fuel flows must be corrected with the effects of the engine installation; then, the emission indices at sea level are plotted and curve fitted in a log10-log10 scale against the corrected fuel mass flows. For the fuel flow at altitude the corresponding $EINO_x$ of sea level is determined from the plot created before and then the $EINO_x$ at sea level is determined with a correction that for example for the BFFM2 is the following:

$$EINO_{X\,FL} = EINO_{X\,FL}\left(\frac{\delta_{amb}^{1.02}}{\theta_{amb}^{3.3}}\right)^{0.5} e^{H}$$

(4-15)

Where $\delta_{amb} = p_{amb}/101.325$ and $\theta_{amb} = T_{amb}/288.15$ while H is the same as in the previous method.

This technique could also have been applied to SABRE, but it was discarded because the p3T3 method is generally more accurate.

Simplified physics-based models and high-fidelity simulations

Both these models are computational ones: the first class consisting in subdivision of the combustor in many zones, each one modeled as an ideal reactor, reducing the computational cost but without the introduction of the complex kinetics necessary to predict the emissions. The second typology is based on the fluid dynamics inside the combustor and include the kinetic mechanism, but they require the detailed geometry of the combustion chamber in order to apply the correct boundary conditions and they are more computationally expensive.

4.2.3 Application of the p3T3 method to SABRE

In this section, the path and results of the p3T3 method applied to SABRE are reported. Starting from the equation (4-13) which is here reported again for the sake of clarity, it is possible to make few considerations.

$$EINO_{X\,FL} = EINO_{X\,SL}\left(\frac{p3_{FL}}{p3_{SL}}\right)^{n}\left(\frac{FAR_{FL}}{FAR_{SL}}\right)^{m} exp(H)$$

First of all, it is important to highlight that the emission indices at sea level are not available at any points: in fact, as previously stated, no analysis has been previously carried out regarding the engine and it is obviously absent from the ICAO emission databank, since it is still in a development phase. Regarding the other parameters, they can all be extracted from the previous simulations and here in particular the values from the complete model are used. However, there are also other problems related with this formulation: the p3T3 method was originally developed for application to subsonic engines burning hydrocarbon fuels and the exponent n and m are specifically related to

these assumptions. It is probably wrong to assess that the same values can be used for a completely different engine cycle that also uses a different fuel. Another problem arises from to the fact that it was formulated with the intention to be applied to subsonic engines, while SABRE operates in a wide range of Mach number. Last, while in common aircraft engines there is only one combustion chamber, here there are two different combustion stages with dissimilar conditions.

The first addressed problem was the absence of estimation for the emissions at sea level. One first hypothesis was to consider the emissions of Scimitar and adapt them to the SABRE, but this was soon discarded due to the aforementioned differences between the two engines.

So, some simulations of the combustion were conducted. It was decided to perform the simulations in four different points at ground level corresponding to the points from M=0.1 to M=0.4 and in four points along the ascent corresponding to M=1,2,4,5, in order to compare these results with those of the p3T3 method. The simulations were performed both in the pre-burner and combustion chamber using 0D thermodynamic and kinetic methods i.e., in equilibrium and non-equilibrium conditions; however, after the initial results, it was noted how the equilibrium model underestimated the NO_x emissions, much like what happens by using CEA, and thus only the kinetic model results were taken into consideration. The input for the pre-burner analysis were the pressure inside the pre-burner that was set equal to $p°_7$ of the scheme in Figure 3.26, and the temperatures and mass flows of the reactants, that were set equal to the conditions at station 6 for the air, considered as a mixture of nitrogen and oxygen with mass fractions of respectively 0.77 and 0.23, and the station 17 for the hydrogen. The input data for the simulation of the combustion chamber were the mass flows of the chemical species forming the reacting mixture that enters the CC (N_2 from the PB, N_2 from air, O_2 from air, H_2O from PB and H_2 from PB) at the mixing temperature that was calculated by making an enthalpy balance between the temperatures of the exhaust gases after they pass through the HX3 and the fresh air from the compressor. The pressure of the CC was set equal to that in station 10. Combustion was assumed to be isochoric and adiabatic, thus giving slightly different results than the previous models in which the combustion was considered quasi-isobaric. Then a kinetic scheme had to be adopted. The choice was between the model of N. Zettervall and C. Fureby (N. Zettervall, 2018), that has been widely validated in the relatively low pressure range of typical air-breathing engines combustion, or the more detailed Konnov scheme, in which also the NNH mechanism previously described was added in (Alexander A. Konnov, 2000) and that was updated in (Konnov, 2008) and lately in (Konnov, 2019). The choice fell on the second, mainly because of its wider applicability.

Part of the compositions of the exhaust gases of both the pre-burner and the combustion chamber is reported below in Table 9 and Table 10.

Mass fractions	**Injected H_2**	**Expelled H_2**	**O_2**	**N_2**	**H_2O**	**NO**	**NO_2**	**NH_3**
M=0.1	0.127	0.101	1.59E-09	0.669	0.229	1.13E-06	2.11E-12	1.24E-03
M=0.2	0.127	0.101	1.41E-09	0.668	0.229	1.05E-06	1.87E-12	1.27E-03
M=0.3	0.127	0.102	1.20E-09	0.668	0.229	9.41E-07	1.59E-12	1.32E-03
M=0.4	0.128	0.102	9.86E-10	0.668	0.229	8.29E-07	1.32E-12	1.39E-03
M=1	0.129	0.104	4.73E-10	0.667	0.228	5.09E-07	6.16E-13	1.47E-03

M=2	0.112	0.086	2.23E-09	0.680	0.233	1.37E-06	3.17E-12	1.09E-03
M=4	0.137	0.112	5.77E-11	0.662	0.226	1.27E-07	6.55E-14	2.26E-04
M=5	0.153	0.128	5.55E-12	0.650	0.222	3.00E-08	6.90E-15	3.01E-05

Table 9: composition of exhaust gases of pre-burner

Mass fractions	**Injected H_2**	**Expelled H_2**	**O_2**	**N_2**	**H_2O**	**NO**	**NO_2**	**NH_3**
M=0.1	0.054	0.040	4.07E-09	0.716	0.243	1.57E-06	5.37E-12	2.83E-04
M=0.2	0.054	0.041	3.94E-09	0.716	0.243	1.55E-06	5.23E-12	5.32E-05
M=0.3	0.054	0.041	3.8E-09	0.716	0.243	1.52E-06	5.08E-12	5.17E-05
M=0.4	0.054	0.041	3.61E-09	0.716	0.243	1.48E-06	4.89E-12	5.25E-05
M=1	0.055	0.042	3.25E-09	0.715	0.243	1.39E-06	4.36E-12	4.74E-05
M=2	0.054	0.043	4.04E-09	0.714	0.243	1.53E-06	4.6E-12	3.49E-05
M=4	0.060	0.047	2E-08	0.712	0.241	4.69E-06	2.61E-11	2.35E-04
M=5	0.063	0.048	4.64E-08	0.711	0.241	9.12E-06	8.29E-11	4.53E-04

Table 10: composition of exhaust gases of combustion chamber

In this tables the main combustion products are reported and we can see that nitrogen, hydrogen and water make up almost all of the products. Then the mass fractions of the NO_x of our interest are reported and we can see that the NO_2 are negligible (and thus not considered in the application of the method) with respect to NO. Moreover, it is possible to notice the production of ammonia which is not considered here and the fact that practically all of the oxygen from air is burnt, as we expected since the mixture is fuel rich. We can also see how a large part of the hydrogen injected is expelled as it is practically wasted. The second columns of both Table 9 and Table 10 refer to the mass fraction of the fuel that is injected in the two chambers and that is used in the computation of the EINO as it can be seen later.

Coming to the effective application of the p3T3 method, first, two separate calculations were accomplished for the pre-burner and the combustion chamber, in order to estimate the EINO of the two different chambers along the trajectory. The EINO of the eight available points were calculated with the following formula and a constant, average value of the first four was taken as $EINO_{SL}$.

$$EINO = 1000 \frac{m_{NO}}{m_{H_{2_{in}}} - m_{H_{2_{out}}}}$$

(4-16)

Where *m* indicates the mass and EINO is expressed as grams of NO produced per kilograms of hydrogen burnt.

	EINO [$g_{NO}/kg_{H2\ burnt}$]
M=0.1	0.0437
M=0.2	0.0404
M=0.3	0.0364
M=0.4	0.0320
M=1	0.0197
M=2	0.0522
M=4	0.0050
M=5	0.0012

Table 11: EINO of the pre-burner in the known points

As we can see from the Table 11: EINO of the pre-burner in the known points and expected from the previous mass fractions, the NO produced in the pre-burner are very low and practically negligible. The EINO at sea level is equal to 0.0381 g/kg. The results of the combustion chamber are a little bit higher as we expected from the higher temperatures but still negligible and are reported in the table below.

	EINO [$g_{NO}/kg_{H2\ burnt}$]
M=0.1	0.1159
M=0.2	0.1146
M=0.3	0.1124
M=0.4	0.1093
M=1	0.1025
M=2	0.1419
M=4	0.3474
M=5	0.6136

Table 12: EINO of the combustion chamber in the known points

The p3T3 method was then applied using as $p_{3_{SL}}$ and FAR_{SL} the average of the inlet pressure and fuel to air ratio of the two chambers at the first four points. For the pre-burner, the FAR was calculated as the mass flow of the hydrogen divided by the mass flow of the air, while for the combustion chamber it was calculated as the ratio of the unburnt hydrogen exiting the pre-burner and the sum of the fresh air directly injected in the CC and the remaining exhaust gases of the PB. The calculations were performed both for the pre-burner and the combustion chamber in four different ways that are all plotted in the following graphs. The first case consists in the classic formulation of the method i.e., using the exponents $n = 0.4$ and $m = 0$. In the second case the exponent m was changed to a value equal to 0.05, which was derived from an initial analysis on the emissions of Scimitar. However, as it can be seen, the results are practically the same of the classic formulation and are not applicable to SABRE. The last two formulations are respectively:

$$EINO_{X\,FL} = a\, EINO_{X\,SL} \left(\frac{p3_{FL}}{p3_{SL}}\right)^{0.4} \left(\frac{FAR_{FL}}{FAR_{SL}}\right)^{c} exp(H)$$

(4-17)

And

$$EINO_{X\,FL} = a\, EINO_{X\,SL} \left(\frac{p3_{FL}}{p3_{SL}}\right)^{b} \left(\frac{FAR_{FL}}{FAR_{SL}}\right)^{c} exp(H)$$

(4-18)

In which the parameters a, b, c were calculated, when present, in order to best fit the values known at the higher Mach numbers, through the Curve Fitting toolbox of Matlab. For the pre-burner, which results and errors are plotted in Figure 4.6: EINO of pre-burner and Figure 4.7, for the formulation (4-17) the values of the coefficients are $a = 0.4227$ and $c = -7.897$ while for the formulation (4-18) are $a = 0.4313$, $b = 2.183$ and $c = -9.376$.

Instead for the combustion chamber (Figure 4.8: EINO of combustion chamber and Figure 4.9), $a = 847.6, c = 9.602$ for formulation (4-17) and $a = 2464, b = -0.001245$ and $c = 11.3$ for formulation (4-18). The errors, reported in Figure 4.7: errors in the pre-burner and Figure 4.9, are calculated as

$$err = \frac{EINO_{FL} - EINO_{real}}{EINO_{real}} * 100$$

(4-19)

where $EINO_{FL}$ is the one calculated with the classic or modified method and $EINO_{real}$ is the result of the simulation.

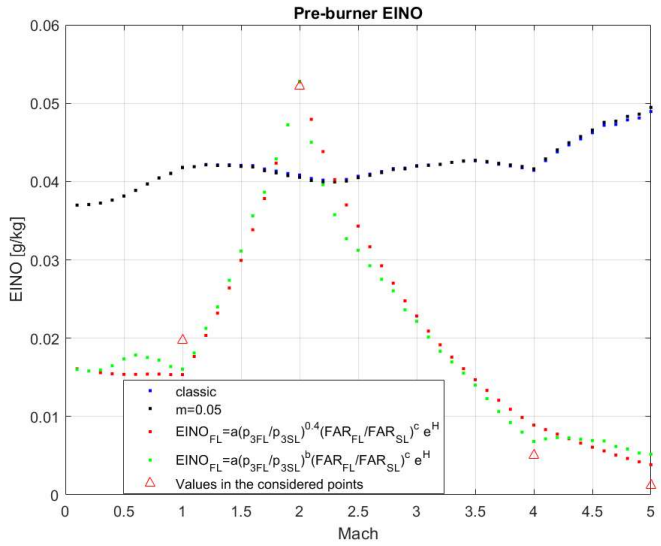

Figure 4.6: EINO of pre-burner

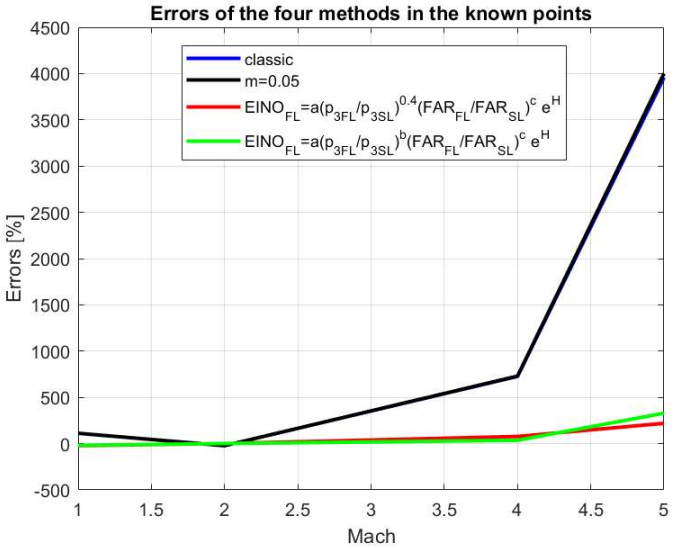

Figure 4.7: errors in the pre-burner

In the case of the pre-burner the classic method preforms particularly bad, and it is absolutely non applicable. However, also the modified formulations are shown to be

poorly accurate, with average errors around 90 % and maximum errors of 200 %. This is probably due to the value of simulated EINO at M=2 which is out of scale with respect to the others: this is probably justified by the lower fuel to air ratio, which reaches its minimum in this point and this could encourage the formation of NO.

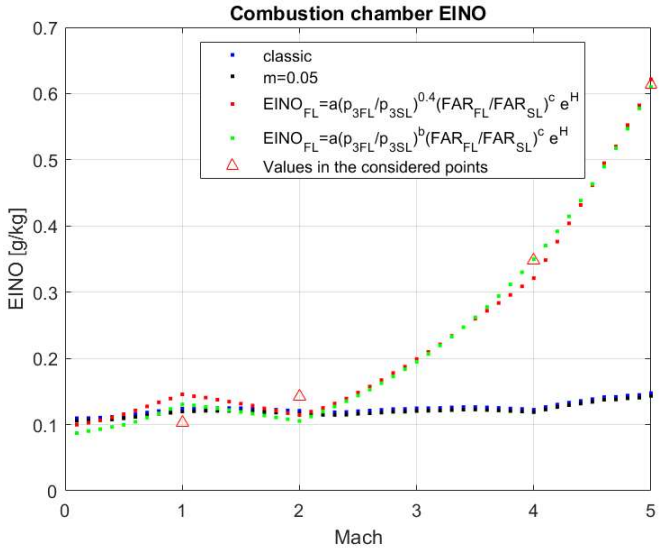

Figure 4.8: EINO of combustion chamber

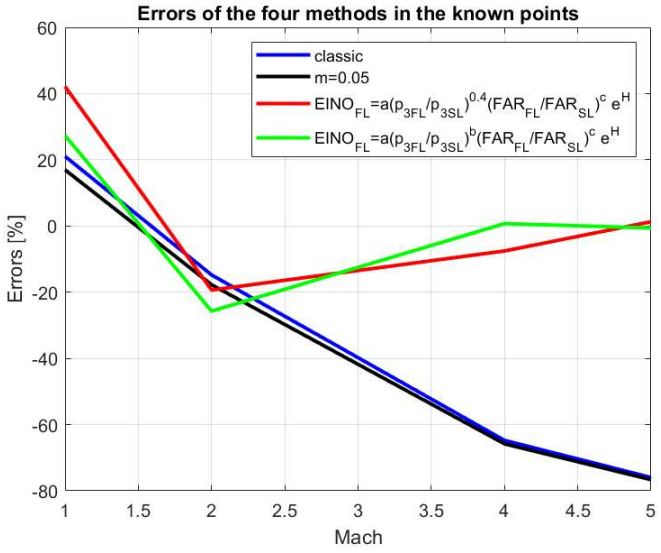

Figure 4.9: errors in the combustion chamber

Regarding the combustion chamber, we can see again that the classic method is not applicable while the two modified versions perform quite well with the last formulation that is slightly more accurate with an average error of 13.6% against the 17.6% of the other.

Another path was also followed: instead of calculating the two different EINO for pre-burner and combustion chamber, only one global emission index was calculated considering in the formula the mass of hydrogen injected in the pre-burner and expelled by the combustion chamber. Equation (4-16) becomes

$$EINO = 1000\frac{Y_{NO_{CC}}\dot{m}_{out\ CC}}{Y_{H_{2_{inPB}}}\dot{m}_{in\ PB} - Y_{H_{2_{outCC}}}\dot{m}_{out\ CC}}$$

(4-20)

Where $Y_{NO_{CC}}$ is the mass fraction of NO at the outlet of combustion chamber, $Y_{H_{2_{inPB}}}$ is the mass fraction of hydrogen that enters the pre-burner, $Y_{H_{2_{outCC}}}$ is the mass fraction of the unburnt hydrogen exiting the combustion chamber and $\dot{m}_{in\ PB}$ and $\dot{m}_{out\ CC}$ are respectively the sum of the hydrogen and the air entering the pre-burner and the sum of the pre-burner exhaust gases mass flow and the air mass flow directly injected in the combustion chamber. The global EINO in the eight considered points are reported in the table below.

	EINO [$g_{NO}/kg_{H2\ burnt}$]
M=0.1	0.058
M=0.2	0.057
M=0.3	0.056
M=0.4	0.054
M=1	0.051
M=2	0.056
M=4	0.173
M=5	0.337

Table 13: global EINO in the known points

The path followed for the application of the p3T3 method was the same as before with the difference that the p3 here used was the total pressure at the inlet of the pre-burner and the FAR was the global fuel to air ratio, namely the ratio of the hydrogen mass flow to the total air flow entering the intake.

All the versions previously described were used and are shown in the graphs below (Figure 4.10: global EINO and Figure 4.11: errors on global EINO in known points). For the formulation of equation (4-17), it holds $a = 0.4155$ and $c = 22.27$ while for the formulation of equation (4-18) $a = 0.4677, b = 0.56, c = 20.74$. It is possible to notice that in both cases there is a rather strong dependance with the FAR which explains also why the classic model, where the exponent of the FAR ratio is null, fails in predicting the emissions of such a propulsion system.

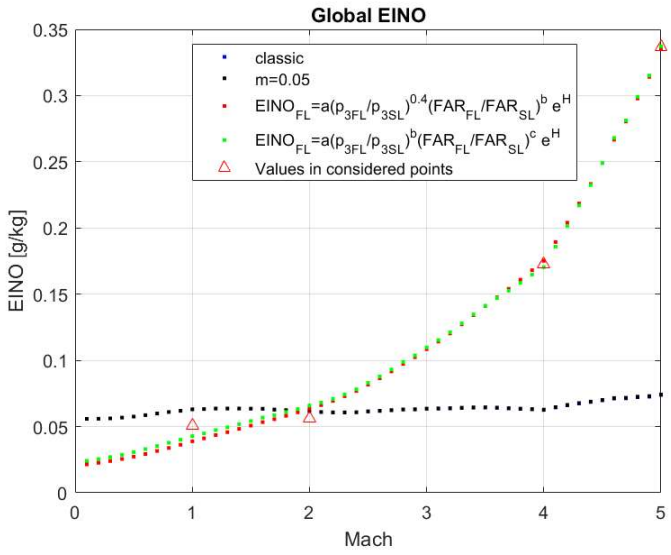

Figure 4.10: global EINO

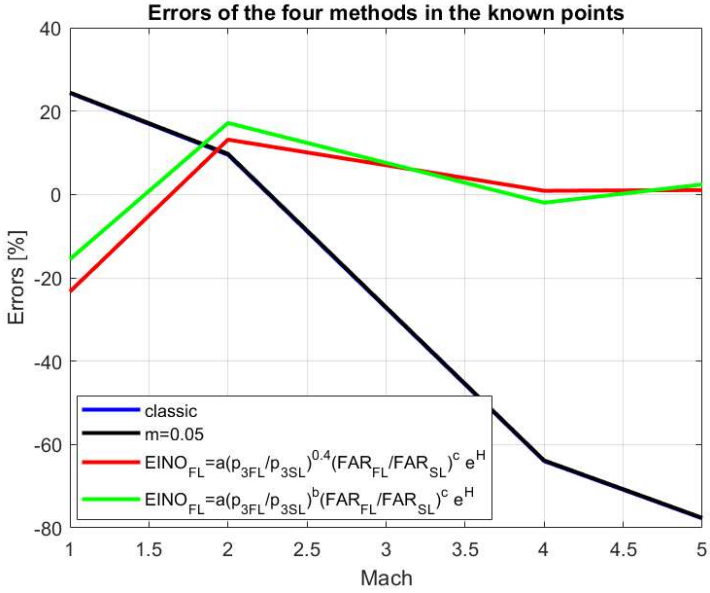

Figure 4.11: errors on global EINO in known points

It is possible to notice that the two modified models perform well, in particular at higher Mach numbers, which is also the most interesting phase since it lasts longer, as can be noticed in Figure 2.3 and it is also useful to evaluate the emissions at higher altitude, as explained at the beginning of section 4.2.

Two other models were also used to estimate the emissions, in particular considering varying sea level conditions by interpolating the pressures, EINO and FAR with temperatures but the results were not reliable because of the high variability of trends during the ascent due to the changing working parameters of SABRE.

Regardless of the model, it is possible to state that SABRE, at least from this preliminary analysis, appears to be particularly clean from the point of view of nitrogen oxides. This can be related to various aspects: first, the temperatures are not very high and this inhibits the formation of NO_x, at least for what regards the thermal mechanism. Moreover, the

fuel rich mixture conditions tend to promote the reactions between oxygen and hydrogen, thus there is not a high amount of atomic or molecular oxygen for the reactions with nitrogen; last the presence of water entering the combustion chamber is positive: in fact, from the presence of the atmospheric humidity correction, we can see that at increasing water content the formation of NO_x is penalized.

4.3 Comparison of environmental impact of SABRE and Falcon 9

The results obtained in the previous sections, both regarding the emissions of greenhouse and pollutant gases, are used in this section to make a comparison with another launcher, the Falcon 9 from SpaceX, in order to assess which of the two is less environmentally impacting. The other launcher was chosen because of its reusability, which makes it similar to Skylon, and the similar capability in delivering payload. In fact, according to (SpaceX, s.d.), the deliverable mass in Low Earth Orbit is around 15 tons for a 28.5° inclined orbit, launching from Cape Canaveral, that has coordinates of 28°N 80°W. Comparing it with the diagram reported in Figure 4.12: delivered payload of Skylon for a 30° launch site from (Reaction Engines Limited, 2014), it is possible to deduce comparable performance of the two space vehicles.

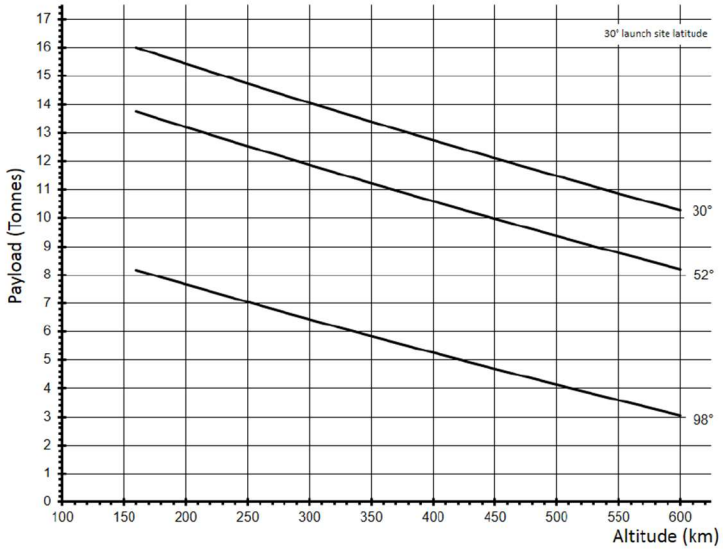

Figure 4.12: delivered payload of Skylon for a 30° launch site (from (Reaction Engines Limited, 2014))

4.3.1 Comparison

For the comparison, the approach described in (National Academies of Sciences, Engineering and Medicine, 2021) was followed. In that work, the first tool for the estimation of emissions of space vehicles was created and integrated in the graphic user interface of the previously developed Rumble 3.0, a program by Blue Ridge Research and Consulting to estimate noise pollution of launchers. The methodology of the research was to obtain engine performance data to estimate the propellant mass flow rate, calculate the emission indices to relate the quantity of burnt propellant to the emitted pollutants and use trajectory data to determine the time spent in each atmospheric layer. It is possible to

notice that all this data are available for SABRE from the previously described analysis, thus a comparison with the vehicles present in the Rumble database is readily practicable. In particular, from the database that contains all launchers used in USA in 2019 and some historical vehicles such as Saturn V and Space Shuttle, the Falcon 9 was chosen for the reasons aforementioned, but it is possible to choose every vehicle without great changes to the procedure that will be described.

The main obstacle that was still present in this calculation was to analyze the performance of SABRE in the pure rocket phase. Almost no literature is present about this since the main interest is obviously focused to the innovative air – breathing mode of the engine. However, it was possible to make some estimations from the data reported in (Reaction Engines Limited, 2014) in the graphs of Figure 2.3: ascent trajectory It can be noticed that the mass decreases linearly in the rocket phase, following the profile reported below in Figure 4.13: decreasing mass profile in the rocket phase. In particular, the rocket phase starts with a mass of 300 tons and ends after 270 seconds with a mass of 75 tons. Therefore, it was possible to establish an average mass flow rate of propellant of 833 kg/s for Skylon, which is comparable to the instantaneous mass flow rate.

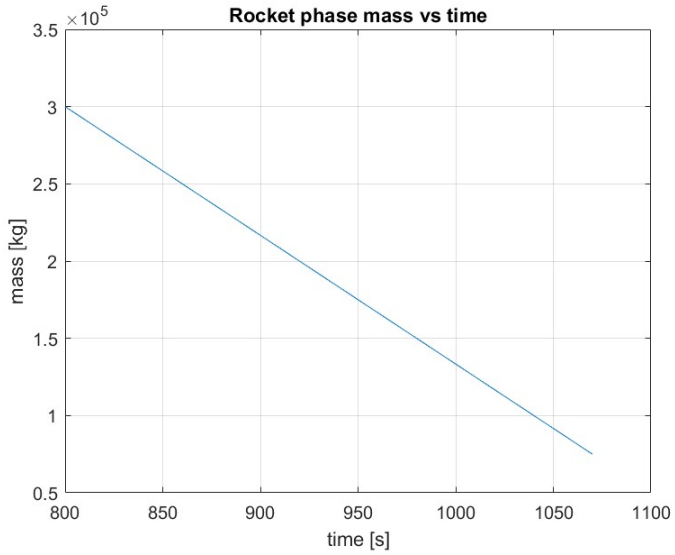

Figure 4.13: decreasing mass profile in the rocket phase

It has to be noted that the Skylon propulsive plant mounts two SABRE engines, each of one consists in four combustion chambers, as explained in the paragraph 2.2, thus the mass flow rate of propellant in each chamber is 104.2 kg/s. The mixture ratio was defined as $MR = \dot{m}_O/\dot{m}_F$, where $\dot{m}_O$ is the mass flow rate of the oxidizer, in our case LO_x, and $\dot{m}_F$ is the mass flow rate of the fuel, in our case LH_2. It was not possible to find any data about the mixture ratio, thus it was assumed to be constant along the ascent and equal to 6, which is a common choice since, even if, it does not correspond to the value associated to the maximum specific impulse (i.e., the minimum propellant consumption) that is around 4, it allows to reduce the structural weight of the tanks by lowering the amount of liquid hydrogen, which possesses a much lesser density compared to the liquid oxygen, usually requiring much more volume.

Then it was possible to calculate the instantaneous mass flow rate of hydrogen and oxygen as:

$$\dot{m}_{LH2} = \dot{m}/(1 + MR) = 119.05\ kg/s$$

(4-21)

$$\dot{m}_{LOx} = \dot{m} - \dot{m}_{LH2} = 714.28\ kg/s$$

(4-22)

The stoichiometric mixture ratio of oxygen and hydrogen is 7.937 so the conditions are those of a fuel rich mixture. This means that, similarly to what was done in 4.1, we can assume that all the oxygen is consumed in the reaction, while only a limited amount of hydrogen is burnt. The emission index of water, which is here considered as the only combustion product, is different than before, when it was equal to $EIH_2O = 8937.3\ g_{H_2O}/kg_{fuel\ burnt}$, because it must be referred to the propellant burnt. The mass flow rate of water emitted is $\dot{m}_{H_2O} = \frac{\dot{m}_{LOx}}{MR_{st}} EIH_2O = 804.3\ kg/s$ so, dividing by the amount of propellant, $EIH_2O = 965.2\ g_{H_2O}/kg_{prop}$. Instead, the mass flow rate of unburnt hydrogen is 29 *kg/s.* Obviously, there are also other minor species formed in the CC, e.g., hydrogen peroxide, but they are neglected in this analysis.

The emissions described until now are the so-called primary emissions, that are made of the species at the nozzle exit plane. The data present in the Rumble database regard the final emissions, that comprises the secondary emissions, made up by the species that are formed in the exhaust plume, in which reactions continue to occur, due to the high temperature of the exhaust gases, that can combine with the surrounding atmospheric air. Thus, it is necessary to evaluate the secondary emission indices of the SABRE, and an approach similar to the one presented in (National Academies of Sciences, Engineering and Medicine, 2021) was used, with the main assumption of frozen composition in the nozzle, that is to say that the species exiting the nozzle are exactly those formed in the CC. Theoretically, for the air – breathing phase, it could be possible to apply directly the first order estimate used in the reference and described by the following equation for water vapor:

$$EIH_2O_f = EIH_2O_p + \frac{MM_{H_2O}}{MM_H} EIH_p + \frac{MM_{H_2O}}{MM_{H_2}} EIH_{2_p} + EIOH_p$$

(4-23)

where the subscript p stands for the primary emission indices, the subscript f for the final and MM for the molar mass of the species. However, as it was noted, this would not give correct results since those emission indices are computed with respect to the whole propellant and not to the burnt fuel mass only. Nevertheless, the theoretical explanation behind the above formula is still valid and is that practically all the remaining unburnt hydrogen exiting the nozzle is converted to water by reacting with atmospheric oxygen in the rocket plume. It is thus possible to evaluate the total mass flow rate of water vapor as:

$$\dot{m}_{H_2O} = \dot{m}_1 f_{ST} EIH_2O + (\dot{m}_H - \dot{m}_1 f_{ST}) EIH_2O$$

(4-24)

where the first addendum is the primary emission and the second is the contribution of the secondary emission. It is now possible to calculate the effective emission index through division by the burnt fuel flow rate. The profile of the final water vapor produced mass flow rate is reported in Figure 4.14. The fuel mass flow indicated in 3.6 had to be multiplied by 8, in order to take into account the two engines with four thrust chambers per each.

For the rocket phase the method described in (National Academies of Sciences, Engineering and Medicine, 2021) is applicable since all the calculated indices are referred to the propellant consumed. The primary emission index of unburnt hydrogen is a constant value of $EIH_{2_p} = 34.8 g_{H_2}/kg_{prop}$ so the final emission index of water for the rocket phase is constant and equal to 1276.2 g/kg$_{prop}$. The monoatomic hydrogen and OH were neglected since their mass fractions are several orders of magnitudes lower than those of molecular hydrogen.

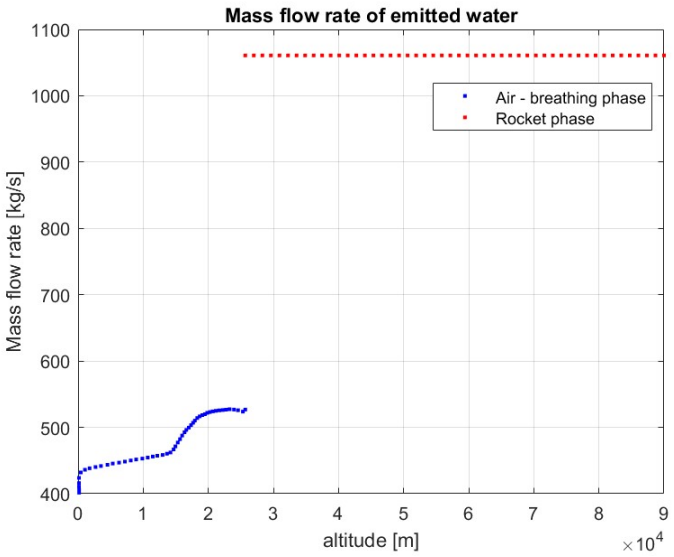

Figure 4.14: final water vapor mass flow rate for the Skylon

Regarding the other species analyzed here, the first order estimate for the secondary emissions of NO_x is:

$$EINO_s = (33 g/kg) e^{-0.26 h/km}$$

where h is the altitude expressed in kilometers and it was assumed that the NO_x are solely composed by NO since the mass fraction of NO_2 was much lower and thus negligible. This emission index has to be referred to the total propellant also in the air – breathing phase so, in order to have a correct estimation, it must be multiplied by the sum of air and fuel flowing through the nozzle. $EINO_p$ is zero for the rocket phase since, unless impurities, no nitrogen is contained in the oxidizer or the fuel. For the air – breathing phase the completely modified formulation of the global EINO, shown in green in Figure 4.10, was chosen as primary emission index since it showed a slightly lower average error. The mass flow rate of NO along all the ascent is reported below.

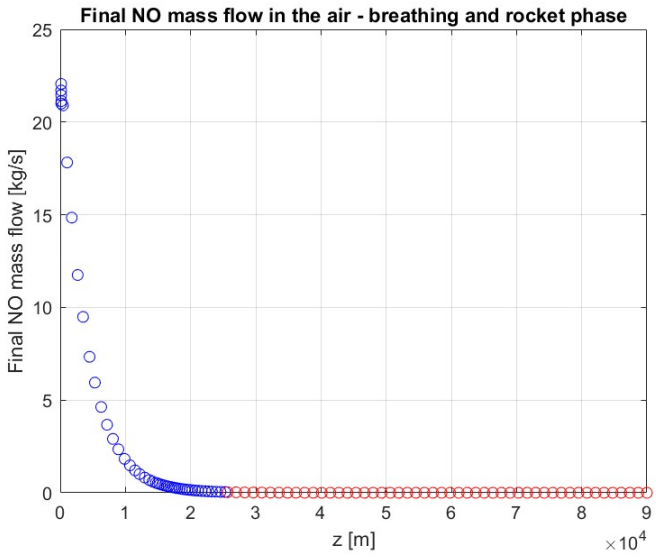

Figure 4.15: final NO mass flow in the air - breathing (blue) and rocket phase (red)

It is now necessary to evaluate the emissions of Falcon 9 through Rumble 3.0. (Blue Ridge Research and Consulting , 2020). In the database, only the results for the first stage are present thus the analysis is limited to that. Below, it is possible to see some images of the graphical user interface of Rumble. First of all, it is necessary to create a study, the case of the analysis of our interest: for us it is "Falcon 9 study". Then, the spaceport data has to be inserted, for example the coordinates of the Kennedy Space Center. The receptors tab can be skipped for our purposes, since it is necessary only for the noise pollution analysis that is not addressed in this work. Operations and a scenario must be defined, by inserting the data of the number of annual operations of the launcher for example, that in our case was put equal to one since we are only interested in one launch, while the trajectory was set equal to the default vertical launch trajectory, since it was shown in (National Academies of Sciences, Engineering and Medicine, 2021) that the typical trajectories of various launchers do not differ much one from another. Finally, the metrics must be selected, in our case the emission summary. Rumble delivers as an output different tables with the masses of pollutants emitted with different level of detail, from the emissions at every one second step to the global amount of pollutant emitted.

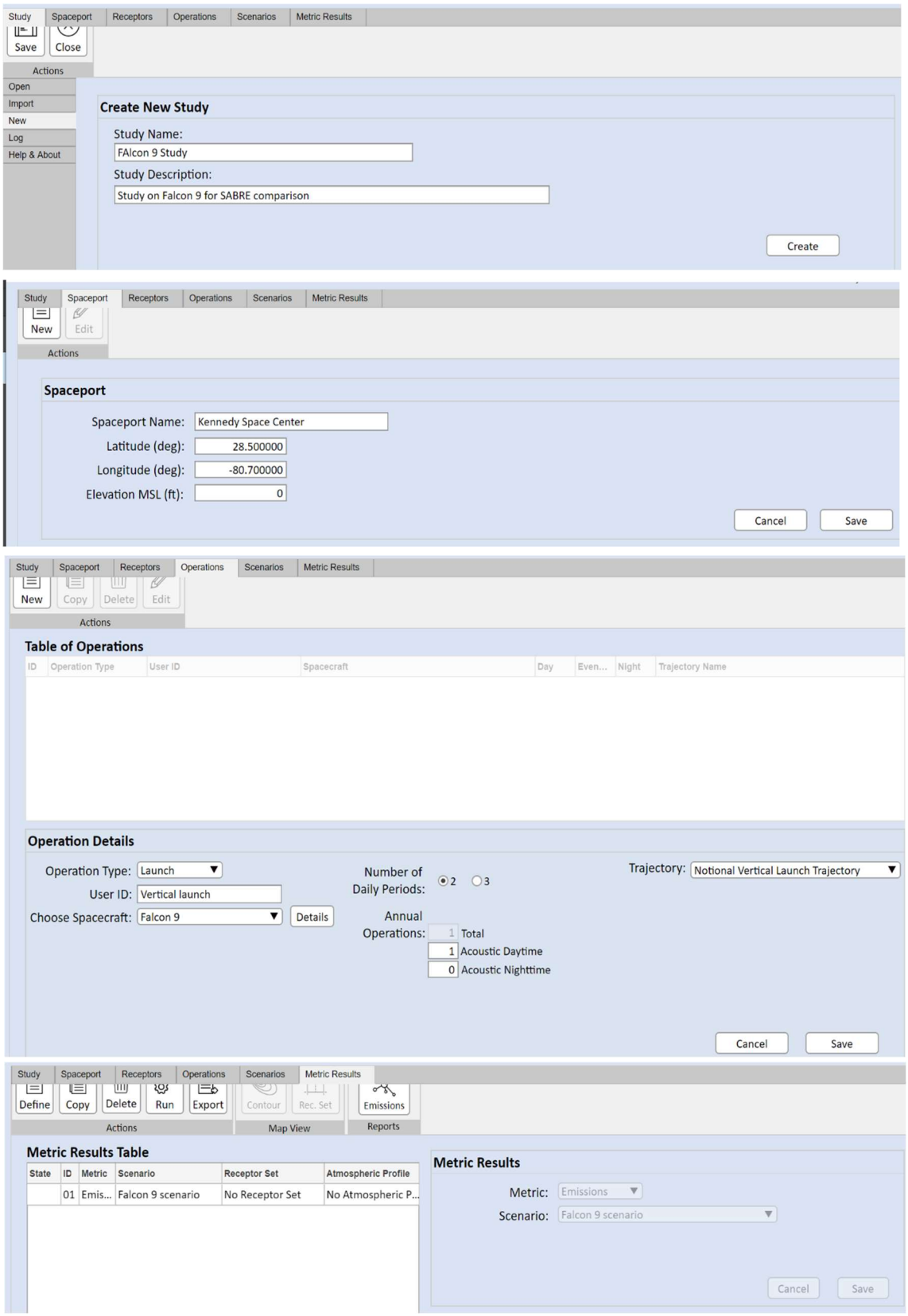

Figure 4.16: workflow of Rumble 3.0

Propellant burn [kg]	CO [kg]	CO_2 [kg]	H_2O [kg]	NO_x [kg]	BC [kg]
418700.0	3931.2	386214.2	156649.9	4184.2	2041.9

Table 14: summary of the total emissions of Falcon 9 first stage

In Table 14: summary of the total emissions of Falcon 9, the summary of the mass of pollutant species emitted by Falcon 9 is reported: the first thing that can be noticed is the main difference from the species emitted by SABRE. This is due to the fact that Falcon 9 burns liquid oxygen and RP-1, a highly refined form of kerosene which is normally used for rocket propulsion. Thus, the presence of carbon dioxide and monoxide and of black carbon, completely absent in SABRE due to the use of a decarbonized fuel. By looking at Table 14, it could seem that the sum of the emitted species masses is higher than that of propellant burnt but this is not an error and it is rather due to the inclusion of elements from the atmosphere during the reactions in the plume.

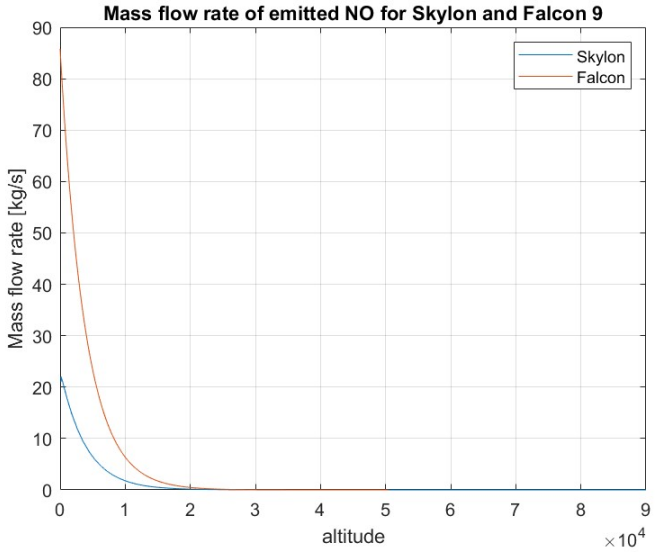

Figure 4.17: Comparison of the mass flow rate of the NO produced by Skylon and Falcon 9

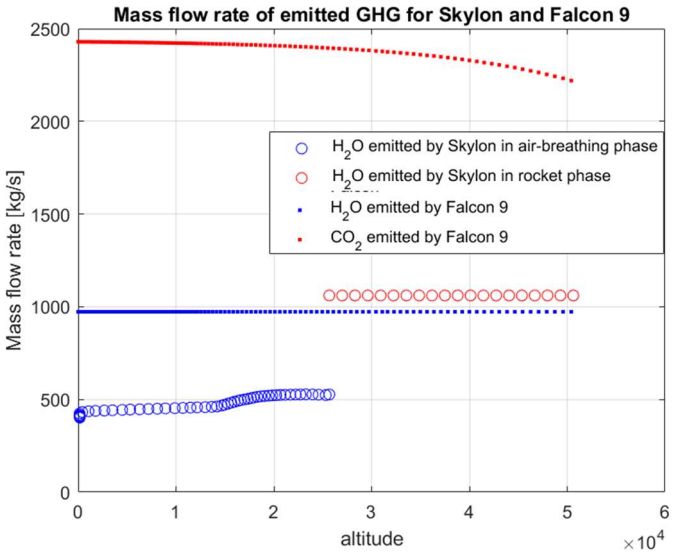

Figure 4.18: comparison of the mass flow rate of GHG produced by Skylon and Falcon 9

Regarding the direct comparison of the two vehicles, the data for Falcon 9 are available until an altitude of 50 km, at which there is the stages separation. Thus, the results will be illustrated until that value. In Figure 4.17, it is possible to see the difference between the Skylon and Falcon 9 production of NO, due to the higher mass flow rate of propellant in Falcon 9.

In order to compare the masses emitted at each altitude it is necessary to evaluate the propellant burn of Skylon. By looking at the graphs in Figure 2.3: ascent trajectory, it was assumed that the Mach number increases linearly with time starting from 0 to 5 in 800 seconds, which is 0.0063 M/s. Thus, the intervals of 0.1 Mach previously used in the models correspond to a time of 15.873 s. For each interval the average mass flow rates of the species were computed. The global results are reported in the table below.

	Propellant consumed [kg]	**H_2O emitted [kg]**	**NO emitted [kg]**
Air – breathing phase	41952	374940	3393
Rocket phase	225000	295070	0.76

Table 15: total emissions of Skylon till 90 km

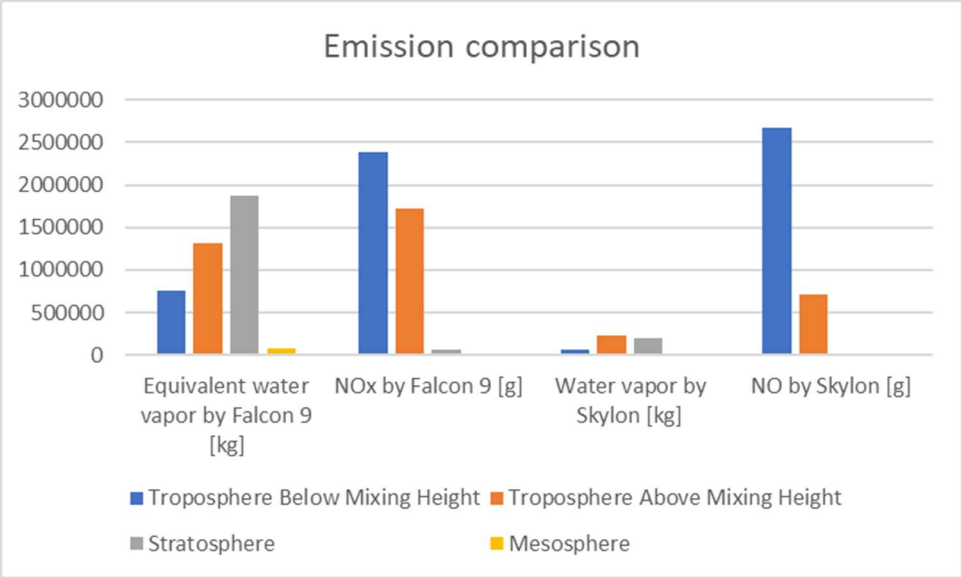

Figure 4.19: emissions comparison in the different atmospheric layers

In Figure 4.19 it is possible to notice how it is not so evident which of the two launch architectures is greener. In this graph an equivalent water vapor emitted by Falcon 9 was calculated by considering that, generally, the impact of CO_2 is ten times higher than that of water vapor, in terms of greenhouse effect. Thus, the mass of the carbon dioxide emitted by Falcon 9 was multiplied by ten and summed to the mass of water vapor effectively emitted. Then the sum of the emission masses was accomplished considering the four different atmospheric layers that are crossed by the two launchers till the altitude of the separation of Falcon 9. It can be seen how the equivalent water vapor of Falcon 9 is much higher in all atmospheric layers. Regarding the NO_x, Skylon is slightly more pollutant below the mixing height, which is around 2850 m, while above that Falcon 9

performs worse and it also emits a small amount of nitrogen oxides in the stratosphere, where they may alter the ozone layer through the mechanisms explained before.

However, an important observation must be said regarding the emissions of NO_x. The formula for the calculation of the secondary emissions is statistically derived and it is based on rockets, that generally do not contain nitrogen in the oxidant, differently from SABRE. Thus, the contributions that are here considered are two: that of the combustion chamber and of the entrainment with atmospheric air, which in any case is also limited due to the confining of the supersonic exhaust plume. In the case of Falcon 9 then only the second is present. In the case of SABRE they are both present and correctly considered in this analysis, but there is also a third contribution related to the afterburning: in fact in the SABRE the exhaust plume is rich of nitrogen and the high temperatures, coupled with the elapsed time may contribute to the formation of nitrogen oxides, even if it must be said that the oxygen is scarse in the plume and has to be supplied by the atmosphere. However, this contribution may be important and should be subject of future analysis.

5 Graphical User Interface

The last part of the thesis work concerned the development of a tool that could ease the use of the previously developed models. In particular, the focus was set onto the possibility to easily vary the input parameters requested by the various cycles illustrated in chapter 3 and plot the results. All the performance models were included in the tool, also the ramjet with fuel cycle model which proved to work poorly on SABRE but that could be useful to analyze a different engine, since this is the final objective of the software. Instead, none of the models presented for the analysis of emissions are present, because they were carefully tailored on SABRE characteristics, and it is not possible to assess at this point if they would work on other engines without major changes.

Regarding the software per se, it consists in a Graphical User Interface, developed with Matlab App Designer, that eases the process and allows to immediately apply changes in future, even for users that do not know the code well. In particular, the SABRE analysis capability was added to the interface previously developed by Simone Moino in (Moino, 2021), for the analysis of hypersonic engines such as ATR and DMR.

Thanks to the creation of this interface, the models can then be added to ASTRID-H, a conceptual design tool for the estimation of performance of high-speed vehicles, continuously improved by the Department of Mechanical and Aerospace Engineering of Politecnico di Torino. ASTRID-H has been developed to support users such as researchers, engineers and students during didactic activities, in the first phases of the project to move from statistical evaluation of data to geometric characterization of the vehicle with insights in the subsystems.

5.1 GUI Architecture

The architecture of the Graphical User Interface has been reprised from the aforementioned one and adapted to match its characteristics. It is reported in the figures below, modified from those reported in (Moino, 2021). In Figure 5.1, the general architecture is reported, with the characteristics of the classic cycles models, that will not be explained here since they were not subject of modification, just as the ATR and DMR models reported in Figure 5.2 and Figure 5.3, that are present for the sake of completeness.

The first request to the user is to choose the model to study between the classic cycles, hypersonic cycles and supersonic cycles such as the precooled air – breathing rocket cycle, typical of SABRE. The architecture of the SABRE model is reported in Figure 5.4. After choosing the case study, the user must select one of the models that were presented before and the necessary input data will be highlighted while the unnecessary ones will be blocked, in order for the software to be clearer. As explained also before the input data

requested vary a lot, based on the model chosen: for example, the complete model is much more demanding than the ramjet with precooler and air compressor model. Every input requested is accompanied by a button in which the suggested value for the simulation is written. The atmosphere model is already present in every cycle and only the ending value of Mach and altitude are requested to model the trajectory. After the insertion of the required values, a new window opens where the user can decide which output needs to be plotted, between those present: the gross and uninstalled thrust, the specific thrust and specific impulse, as defined before. The user must be aware of the limits of each model, as explained in chapter 3.

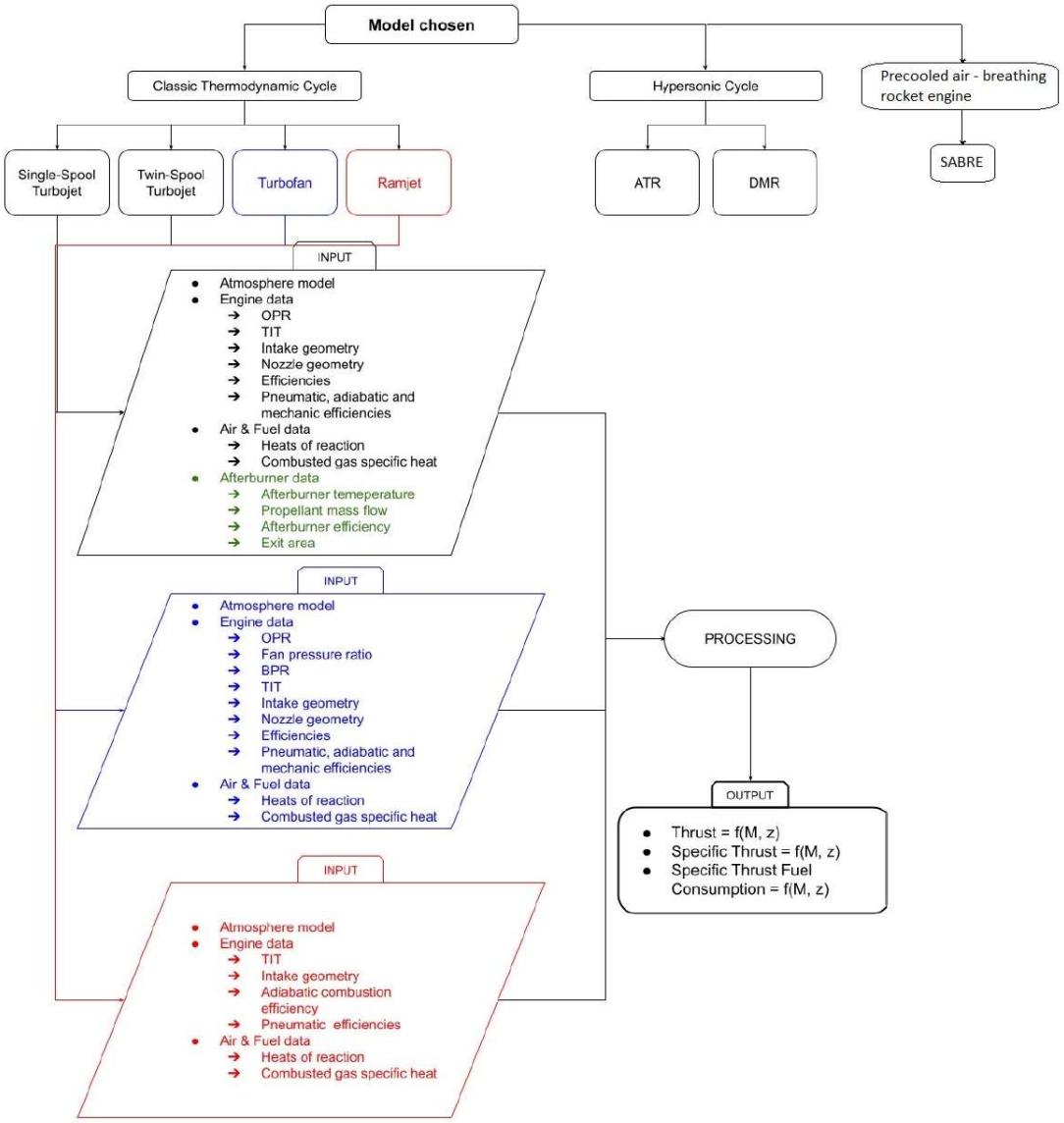

Figure 5.1: GUI architecture: insights of classic cycles capabilities (from (Moino, 2021))

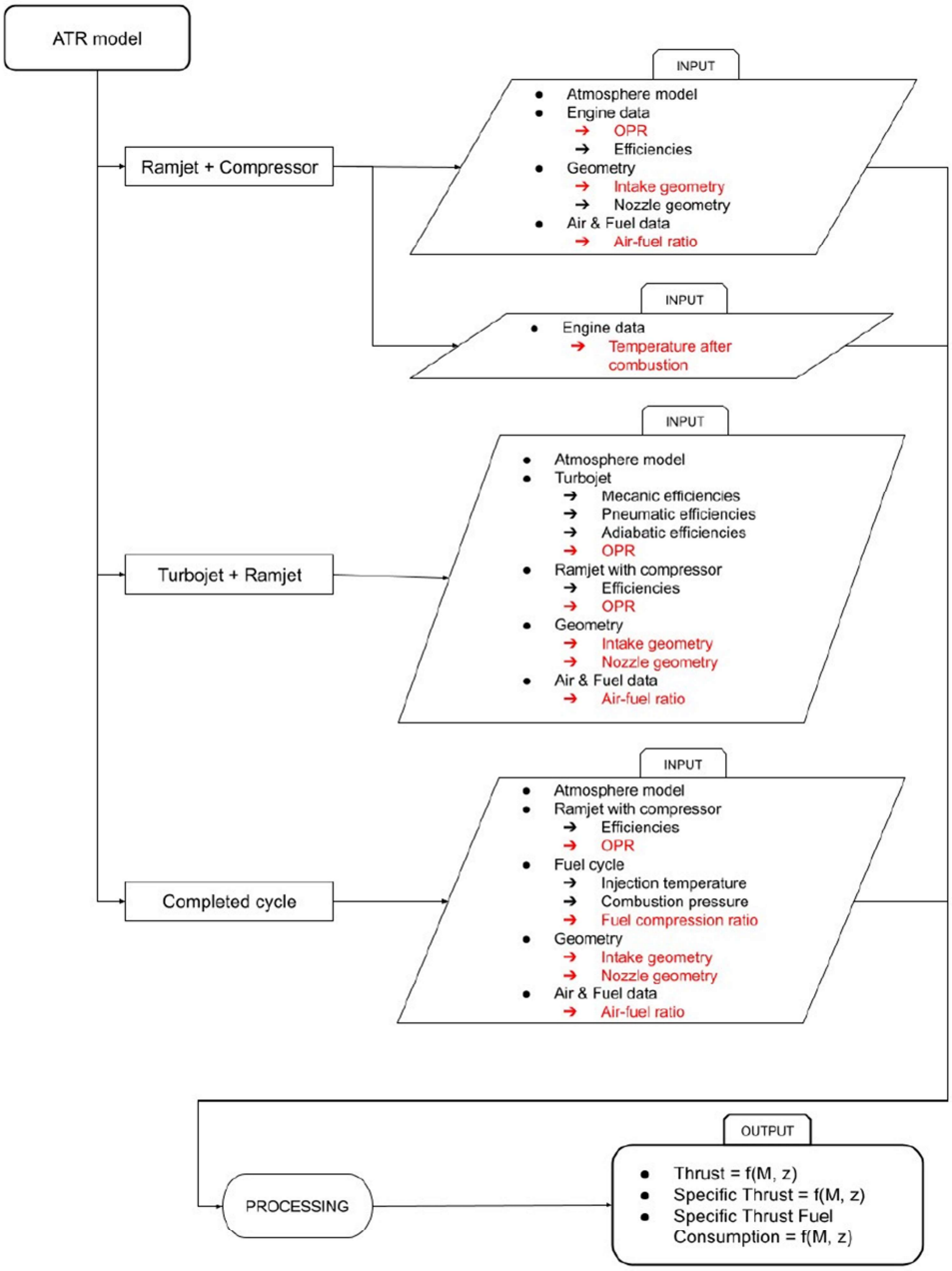

Figure 5.2: GUI architecture: insights of ATR model (from (Moino, 2021))

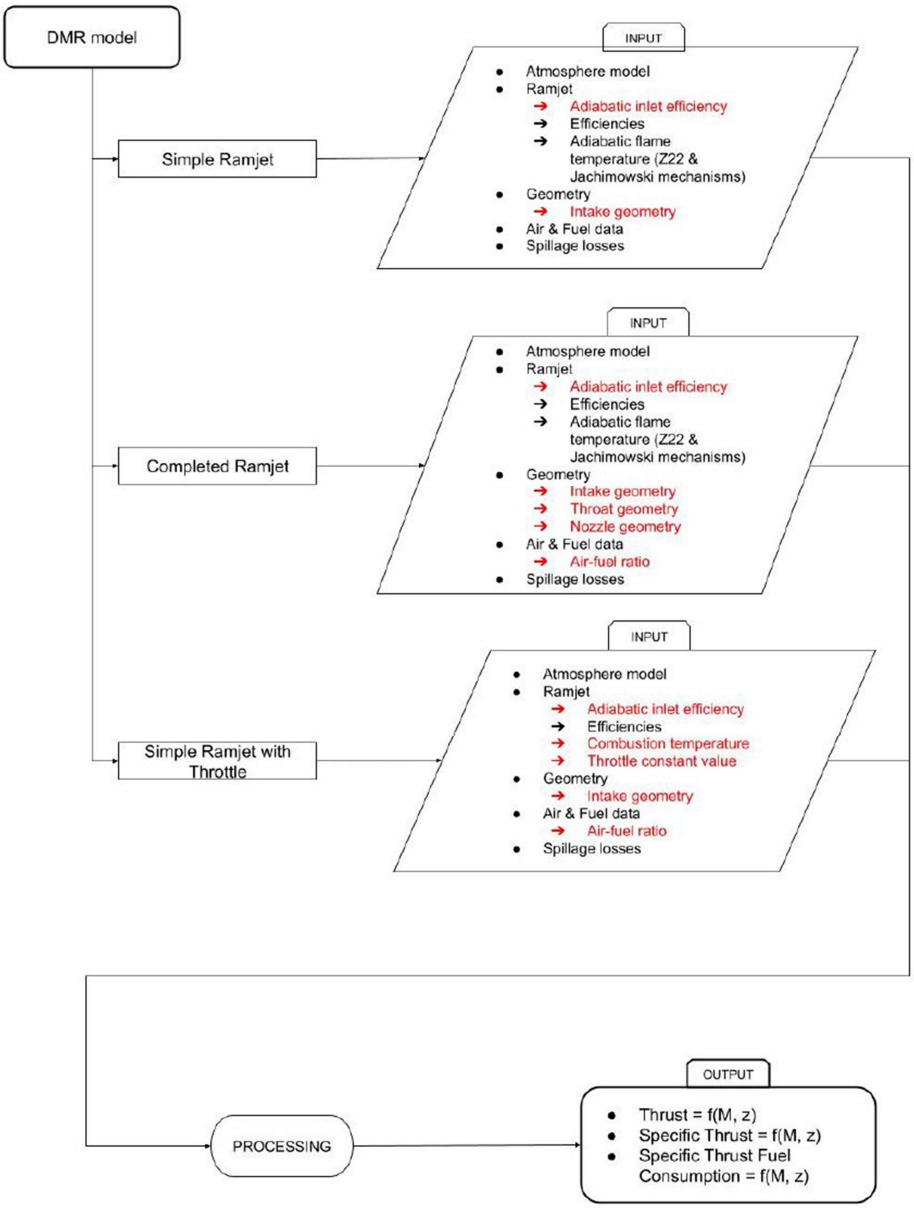

Figure 5.3: GUI architecture: insights of DMR model (from (Moino, 2021))

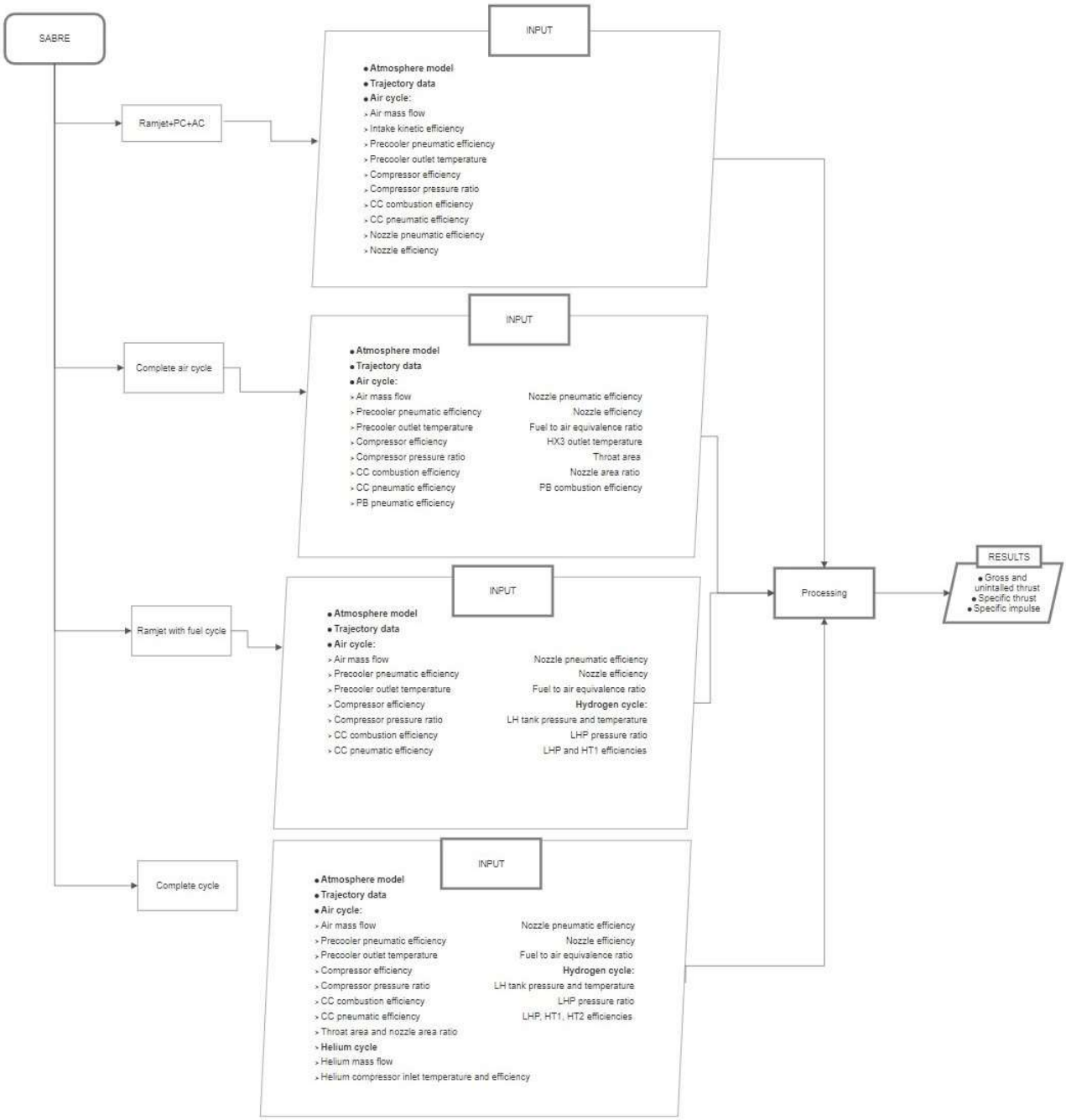

Figure 5.4: GUI architecture: insights in the SABRE model

5.2 Example

The home page of the GUI appears as in Figure 5.5. The different engine classes are visible and after choosing one of them, the user is redirected to the input window. For example, after ticking the SABRE checkbox the window in Figure 5.6 becomes visible and, as it can be seen, after pushing the button corresponding to *Complete air cycle model,* the necessary inputs are highlighted. For example, in this case all the parameters related to the fuel or helium cycle are shadowed. By clicking on the buttons with the question

mark it is possible to see the suggested value for the corresponding box, which in any case is already put as default. The ending points of the trajectory can be chosen by means of the two sliders. Then, by clicking on the *Calculate* button the user is redirected to the output window in which it is possible to choose the result to plot from the drop down tab, as shown in Figure 5.8

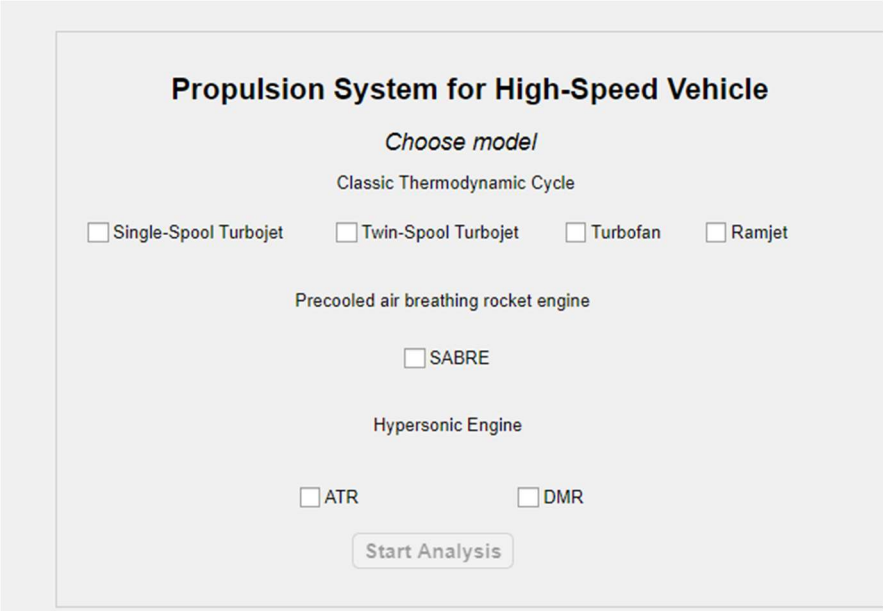

Figure 5.5: GUI home page

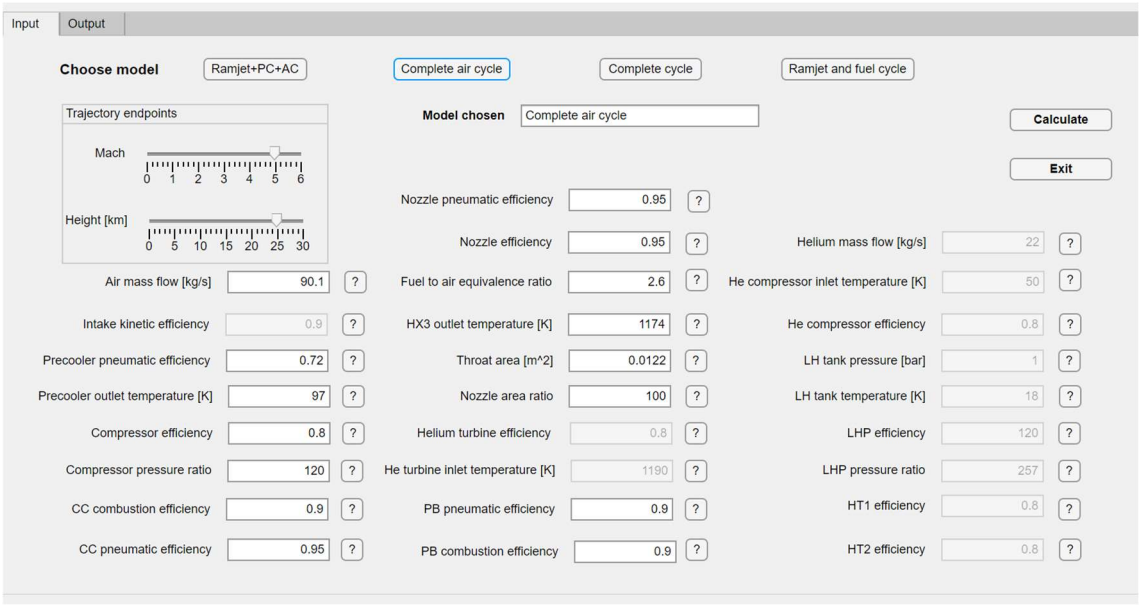

Figure 5.6: input window for complete air cycle model

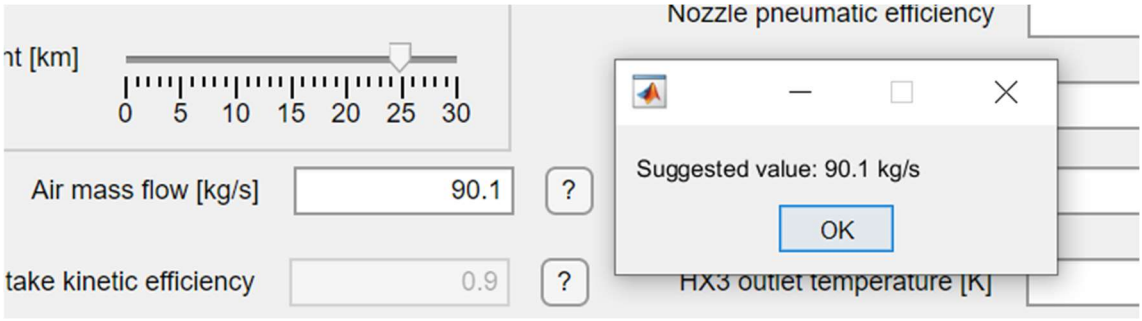

Figure 5.7: value suggestion

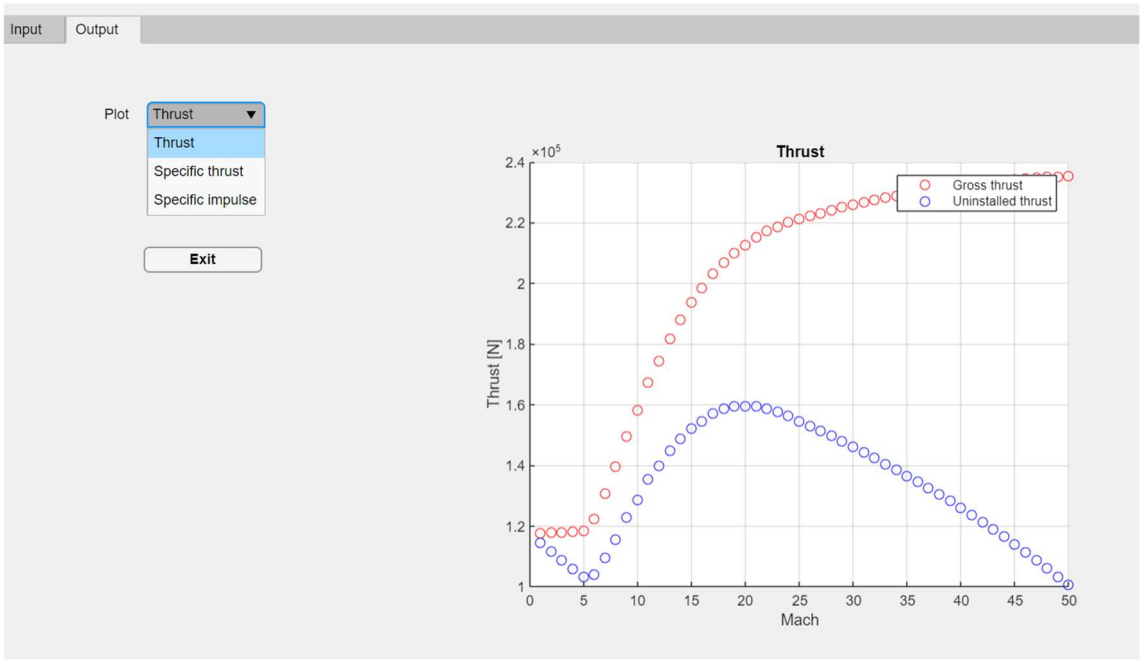

Figure 5.8: output window

6 Conclusions

The scope of this work was dual: to develop models for the estimation of performance of highly innovative propulsion architectures in a conceptual design phase and to use those models to evaluate the environmentally harmful emissions of this engines. The precooled hybrid air – breathing rocket engines were addressed, since they promise to revolutionize in the close future both the space access and the high-speed civil air transport.

In chapter 3, different models for the estimation of performance were built and analyzed, using the SABRE from Reaction Engines as a test bench for the accuracy. The simplest model comprises only the indispensable elements of such an engine, the intake, compressor, precooler, combustion chamber and nozzle and even though it is a highly simplified version of the real engine cycles, it proved to work well, especially at high Mach numbers. In order to further reduce the error, the initial simplifying hypothesis were gradually dismissed, increasing both the calculation complexity, but especially the number input data required, that sometimes had to be hypothesized due to the lack of literature. By doing so, the complete air cycle and the complete model were created and the last one in particular showed a good accuracy along the whole trajectory. Also another model, the ramjet with fuel cycle model, was tested but it proved to work too poorly with respect to its complexity, because it actually represents a different cycle from that of SABRE, disregarding the presence of the helium cycle which is fundamental.

Passing to chapter 4, here the complete model previously cited was used to extrapolate the input data necessary to evaluate the emissions of SABRE, since no literature was found regarding the environmental impact of this engine, even if this aspect is really important, due to the characteristics of reusability and low cost of the launcher. First the primary emissions of water vapor were estimated, considering them to be proportional to the fuel burnt. Then, through methods present in literature it was possible to estimate the secondary emissions, formed in the rocket plume, to have a more comprehensive idea of the impact of the system. Then pollutant emissions, in particular those of NOx, were evaluated. The p3T3 method was used, since it represents a sort of gold standard for this type of analysis, at least for the hydrocarbon subsonic aircrafts. First, the criticalities of the method applied to such a different propulsion system were identified. The absence of data of emissions at sea level was coped with simulations of the combustion in both the pre-burner and combustion chamber, by applying the Konnov kinetic scheme. The same approach was used to calculate emissions at higher Mach numbers in order to make a comparison with the p3T3 method results. As expected, the classic method proved to be not applicable to the engine, but a modified version showed good accuracy with the simulations data. In general, SABRE was found to be particularly clean from the point of view of NO_x, especially if compared with the Scimitar, a modified version for hypersonic air transport. Then these results were used to compare the environmental performance of the subject of the thesis with another innovative launcher, the Falcon 9, chosen because of its reusability and similar payload capacities.

Last, a Graphical User Interface was developed, in order to ease the application of the performance models to other similar systems. Moreover, by doing so, the models could

be later added to ASTRID-H, a conceptual design tool developed at Politecnico di Torino, for the estimation of high-speed vehicles characteristics.

Generally speaking, all the objectives that were meant to be achieved were met, even if there is still margin for some improvements. Regarding the first part, all the models could be rerun and possibly improved with more precise data obtained from the producer. Moreover, the ramjet with fuel cycle model could be tested against the performance of an engine with a more similar cycle, where the helium loop is not present. As for the second part, it could be good to run more simulations along the trajectory points in order to improve the accuracy of the p3T3 method and eventually extend it to other similar engines, maybe also separating the subsonic from the supersonic operations. A new form of the method, directly developed for high-speed hydrogen vehicles, could also be pursued and this is currently under development at Politecnico di Torino: the estimation done here could be carried out again once those results will be available. Moreover, Skylon could be added to the Rumble database and a noise pollution evaluation could also be performed. In order to be as accurate as possible, an evaluation of the life cycle of the spaceplane could be performed. In fact, from the initial comparison with Falcon 9, Skylon proved to be slightly environmentally better but the two launchers are fundamentally different by construction and use different fuels, which production require different resources. Moreover, an evaluation of the NOx produced in the afterburning and due to the aerodynamic heating during reentry should be performed, since they are believed to be quantitively important, according to some sources. Finally, the GUI described could be modified and added to ASTRID-H, as intended.

Bibliography

Alexander A. Konnov, G. C. (2000). The new rout forming NO via NNH.

Blue Ridge Research and Consulting . (2020). Rumble: Launch Vehicle Noise and Emissions Simulation Model. Version 3.0. User Guide.

Bonnie J. McBride, S. G. (1996). Computer program for calculation of complex chemical equilibirum compostions and applications. *NASA Reference Publication 1311*.

Casalino, L. (2018). *Dispense del corso di fondamenti di macchine e propulsione.* Politecnico di Torino.

Dai Jian, Z. Q. (2020). Key technologies for thermodynamic cycle of precooled engines: A review. *Acta Astronautica 177*, 299-312.

Davide Ferretto, N. V. (2020). A conceptual design tool to support high-speed vehicle design. *AIAA Aviation 2020.*

Erik J.L. Larson, R. W. (2016). Global atmospheric response to emissions from a proposed. *Earth's Future 5*, 37-48.

European Space Agency. (2011). *Skylon Assessment Report.*

Fernandez-Villace, V. (2013). *Simulation, design and analysis of air-breathing combined-cycle engines for high speed propulsion.* Madrid: Universidad Politécnica de Madrid.

Hempsell, M. (2010). A phasedapproachtoorbitalpublicaccess. *Acta Astronautica 66*, 1639-1644.

ICAO. (n.d.). ICAO Aircraft engine emissions databank.

Jianqiang Zhang, Z. W. (2017). Thermodynamic efficiency analysis and cycle optimization of deeply precooled combined cycle engine in the air-breathing mode. *Acta Astronautica 138*, 394-406.

Konnov, A. (2008). Remaining uncertainties in the kinetic mechanism of hydrogen combustion. *Combustion and Flame 152*.

Konnov, A. (2019). Yet another kinetic mechanism for hydorgen combustion. *Combustion and Flame*.

Mark Hempsell, J. A. (2016). A Business Analysis of a SKYLON-based European Launch Service Operator. *Acta Astronautica 121*, 1-12.

Mjaavatten, A. (2021). *Thermodynamic models and tools for H2O, H2, CO2 and Air.*

Moino, S. (2021). *Methodology and tools for propulsive performance characterization of high-speed aircraft in conceptual design.* Torino: Politecnico di Torino.

N. Chandrasekaran, A. G. (2012). Study of prediction methods for NOx emission from turbofan engines. *Journal of Propulsion and Power*.

N. Zettervall, C. F. (2018). A computational study of ramjet, scramjet and dual-mode ramjet/scramjet combustion in a combustor with a cavity flameholder.

Nailard, O. (2020). Eliminating the boundary between sky and space. *Physics World 33*.

National Academies of Sciences, Engineering and Medicine. (2021). Commercial Space Vehicle Emissions Modeling. *The National Academies Press*.

National Institute of Standards and Technology. (n.d.). *Thermophysical properties of fluid systems.*

Parliament, U. (2011). Written evidence from Reaction Engines Limited. London.

Pastrone, D. (2019). *Dispense del corso di endoreattori* . Politecnico di Torino.

Pelton, J. N. (2019). *Space 2.0: Revolutionary Advances in the Space Insutry.* Springer.

Peter Glarborg, J. A. (2018). Modeling nitrogen chemistry in combustion. *Progress in Energy and Combustion Science 67*, 31-68.

Reaction Engines Limited. (2014). *Skylon Users' Manual.*

Reaction Engines Limited. (n.d.). *Reaction Engines*. Retrieved from Reaction Engines website: www.reactionengines.co.uk

Space Exploration Technologies. (2008). *Falcon 9 Launche Vehicle Payload User's Guide.*

SpaceX. (n.d.). *Falcon 9: Cpabilities and Services*. Retrieved from https://www.spacex.com/vehicles/falcon-9/

Stanley, M. (n.d.). *A new space economy on the edge of liftoff*. Retrieved from https://www.morganstanley.com/Themes/global-space-economy

Tayfun Tanbay, M. B. (n.d.).

Tayfun Tanbay, M. B. (2020). Assessment of NOx emissions of the Scimitar engine at Mach 5 based on a thermodynamic cycle analysis. *International Journal of Hydrogen Energy 45*, 3632-3640.

TEC-MPC, E. (2011). *Skylon Assessment Report.*

Trainelli, L. (2011). *Lezioni di Meccanica del Volo.*

Varvill, R. (2010). Heat exchanger development at Reaction Engines Ltd. *Acta Astronautica 66*, 1468-1474.

Varvill, R., Jivraj, F., & Paniagua, G. (n.d.). The Scimitar Precooled Mach 5 Engine. *2nd European Conference for Aerospace Sciences.*

Viola, N. (2020-2021). Operational challenges to meet environmental requirements. In P. Maggiore, *Dispense del corso di Gestione dei rischi, costi e supporto logistico integrato dei sistemi aerospaziali.* Torino: Dipartimento di Ingegenria Meccanica e Aerospaziale, Politecnico di Torino.

Zeldovich, J. (1946). The oxidation of nitrogen in combustion and explosion.